UNIVERSITÀ DEGLI STUDI DI PADOVA

Dipartimento di Ingegneria Industriale DII

Corso di Laurea Magistrale in Ingegneria Meccanica

MULTI-POINT OPTIMIZATION OF A TRANSONIC FAN FOR BOUNDARY LAYER INGESTION PROPULSION

Relatore: Dr. Ing. Andrea Magrini

Laureando: Alberto Bergamin, 2045625

Anno Accademico 2023/2024

"A scientist studies what is, whereas an engineer creates what never was."

— Théodore von Karman

ABSTRACT

Boundary Layer Ingestion (BLI) propulsion is a promising concept in aviation engineering that aims to improve aircraft efficiency. The ingestion of a distorted inlet flow, however, introduces stability challenges due to the reduction of the stall margin. This thesis aims to create a family of profiles that can perform efficiently with different values of inlet Mach number and incidence angles, thereby extending the operational range. A multi-point multi-objective optimization was used to find the main features of distortion-tolerant profiles. A Bayesian optimizer was used for its convergence velocity. Objective function evaluations were made using CFD simulations, performed with 3D RANS software adapted for bi-dimensional evaluations. Two significant blade sections were chosen for the optimization, namely the tip and mid-span. High total pressure ratio individuals have low thickness ratio and higher flow deflection. In both blade sections, improvement up to 5% was achieved compared to the initial cascade. High-efficiency individuals are thick and straight at the blade tip, resulting in a gain of up to 15% compared to the baseline, due to decreased shock losses. At mid-span, an increase of 11% is achieved with thin and straight profiles by reducing wake losses. A comparison between the Bayesian optimizer and a well-proven Genetic algorithm is conducted. The effectiveness of the first optimizer was confirmed and earlier convergence was observed.

Sommario

La propulsione BLI (Boundary Layer Ingestion) è un concetto promettente nell'ingegneria aeronautica che mira a migliorare l'efficienza degli aerei. L'ingestione di un flusso di ingresso distorto, tuttavia, introduce problemi di stabilità dovuti alla riduzione del margine di stallo. Questa tesi mira a creare una famiglia di profili che possano funzionare in modo efficiente con diversi valori di numero di Mach in ingresso e angoli di incidenza, estendendo così la margine operativo. Per trovare le caratteristiche principali dei profili tolleranti alle distorsioni è stata utilizzata un'ottimizzazione multi-punto multi-obiettivo. Un ottimizzatore Bayesiano è stato impiegato per la sua velocità di convergenza. Le valutazioni della funzione obiettivo sono state effettuate con simulazioni CFD, eseguite con un software RANS 3D adattato per valutazioni bidimensionali. Per l'ottimizzazione sono stati scelti due sezioni palari significative, ovvero il tip e il mid-span. Gli individui con un elevato rapporto di compressione totale hanno un basso rapporto di spessore e una maggiore deflessione del flusso. Entrambe le sezioni della pala dimostrano un miglioramento fino al 5% rispetto alle schiere iniziali. Gli individui ad alta efficienza sono spessi e rettilinei al tip della pala, con un guadagno fino al 15% rispetto alla baseline, grazie alla riduzione delle perdite per urto. A mid-span, si ottiene un aumento dell'11% con profili sottili e rettilinei, riducendo le perdite di scia. È stato condotto un confronto tra l'ottimizzatore bayesiano e un algoritmo genetico ben collaudato. L'efficacia del primo ottimizzatore è stata confermata e si è osservata una convergenza più rapida.

Contents

LIST OF FIGURES

LIST OF TABLES

ABBREVIATIONS

BLI Boundary Layer Ingestion.

BO Bayesian Optimization.

CFD Computational Fluid Dynamics.

DV Decision Variables.

EHVI Expected Hypervolume Improvement.

GA Genetic Algorithm.

GPS Gaussian Processes.

LHS Latin Hypercube Sampling.

MCA Multiple-Circular-Arc.

MPOP Multi-Point Optimization Problem.

OF Objective Function.

RANS Reynolds-averaged Navier–Stokes.

SPOP Single-Point Optimization Problem.

TPR Total Pressure Ratio.

TTR Total Temperature Ratio.

NOMENCLATURE

α angle of attack.

β relative flow angle.

η_{pol} polytropic efficiency.

LE Leading edge.

PS Pressure side.

SS Suction side.

TE Trailing edge.

1 INTRODUCTION

In recent years, awareness of how different means of transportation affect the environment grew. This is caused especially from the significant impact of carbon dioxide (CO2) emissions on long-term climate change [1]. In this context, the European Commission created a long-term plan in 2018 to achieve carbon neutrality (Net-Zero) by 2050 [2]. Although aviation currently contributes only about 2.5% to environmental pollution [3], forecasts predict a substantial annual average growth of 4.2% in global passenger numbers from 2023 to 2040 [4].

To reduce carbon emissions, new aviation concepts are being developed, aiming to enhance aircraft efficiency. This not only helps in reducing emissions but also lowers the cost of flying. One concept proposed to decrease carbon emissions by enhancing plane efficiency is the Boundary Layer Ingestion (BLI) propulsion. The fundamental concept behind BLI propulsion is to improve the overall efficiency of the aircraft by revitalizing the boundary layer that develops on the vehicle surface. This allows for a reduction in fuel consumption by reducing the drag of the aircraft and increasing the engine propulsive efficiency. The concept of BLI propulsion has been known for a long time. Early studies conducted by Smith et al. [5] more than 70 years ago already confirmed the potential of the solution. While the BLI configuration promises enhanced vehicle efficiency, the ingestion of the boundary layer introduces stability challenges for the engine. These issues are primarily due to the decreased surge margin available [6]. This latter raises considerable concerns about aircraft safety.

Over the years, many studies were conducted to understand flow physics and develop multi-fidelity tools to address the problem. Here, some research contributions are reported and briefly described.

Investigations using Computational Fluid Dynamics (CFD) tools were performed to understand the effects of distorted inflows on compressors. Fidalgo et al. [7] investigate the aerodynamics of NASA rotor 67 operating in a transonic regime with a 120-degree circumferential distortion in stagnation pressure to understand the fan behaviour. Using high-fidelity, full-annulus, unsteady CFD, the researchers observe a redistribution of incoming quantities, due to the total pressure distortion. This redistribution caused the fan to work differently around the annulus and also distorted conditions were observed after the compressor stage. A variation of the shock passage was also observed.

Lesser et al. [8] used numerical data and an analytical approach to understand how circumferential distortions are transported throughout a transonic fan. The main finding was the role of the decoupled speed of propagation of the inflow velocity and static pressure distortions which increases the distorted sector and causes the variation of the distortion after the fan stage. The results of the transportation phenomena were general since they were not dependent on the specific compressor geometry. Also, the flow field at the tip of the compressor was studied since the area is critical for stability. Conditions similar to near-stall were observed with no separation occurring. Overall in the distorted area, the compressor was working beyond the surge line.

Gunn et al. [9] studied a BLI fan at cruise conditions to understand the fluid dynamics and the loss causes using full annulus CFD simulations along with high-resolution experimental data. Researchers observed that one of the main causes for the loss of efficiency was the off-design conditions across the annulus due to the inlet distortion. This was present in both the transonic and subsonic test cases.

Several methods were developed for predicting the performances of compressors under distorted inflows. One of the first was the parallel compressors theory proposed by Pearson et al. [10]. This theory

calculates the performance of the compressor as the weighted sum of two compressors working with the same angular velocity and static back pressure. The first operating under free-stream conditions with a high total pressure; the second with a low total pressure, simulating the distorted inflow. This method deals with total pressure circumferential distortions. A modified version was proposed in 2011 by Cousins et al. [11], extending the theory also to complex circumferential patterns, swirl, and temperature distortions.

Concerning the solutions proposed to mitigate the inlet distortion effects, one was submitted by Shaw et al. [12]. Researchers investigate the impact of variable inlet guide vanes (VIGV) on a transonic fan with distorted inlet flow. Specifically, the study revealed that the implementation of VIGVs not only enhances performance but also increases stability margins by mitigating the presence of the swirl at the fan inlet. Furthermore, a good correlation between CFD and experimental data was found.

Da et al. [13] performed an optimization on a transonic fan ingesting a distorted inflow, investigating the best sweep angle to reduce losses. The aim was to create useful guidelines for the design of compressors under distorted inflow. The final design reduced tip leakage and flow separation at the hub, improving the efficiency also outside the design conditions.

1.1 Objectives

This thesis aims to create a family of profiles that can perform efficiently with different values of inlet Mach number and incidence angles, thereby extending their operational range. For this purpose, a previously designed transonic fan is taken as a test case. Two blade sections were analyzed. First, the blade tip was studied, where a multi-point optimization was performed to create the family. The second design point was specifically chosen to recreate the conditions under a distorted inlet. A Bayesian optimizer was used for its velocity of convergence. A new optimization of the same problem was performed using a well-proven Genetic algorithm to test the effectiveness of the Bayesian optimizer. The mid-span blade section was then considered. Two Bayesian optimizations were performed using two different strategies to induce the near-stall conditions at the second design point.

2 METHODS

2.1 Test Case: Fan Baseline

To evaluate the improvements achieved through the optimization, a baseline was established as a reference point. The initial fan was designed for a BLI propulsion configuration, with the engine placed at the tail of the aircraft. Two-dimensional cascades were constructed using common geometries typical of fans with uniform inlet flow. For example, a Multiple-Circular-Arc (MCA) airfoil was used at the tip of the blade due to its well-known performance in low supersonic conditions. The 3D blade was generated by stacking the 2D profiles while accounting for the distorted inflow. This procedure resulted in a fan with 13 blades and a target fan pressure ratio of 1.3. Figure 2.1 displays the two-dimensional profiles respectively at spans 0%, 50%, and 100%. The coordinate r and m will be defined later on, while θ is the circumferential angle.
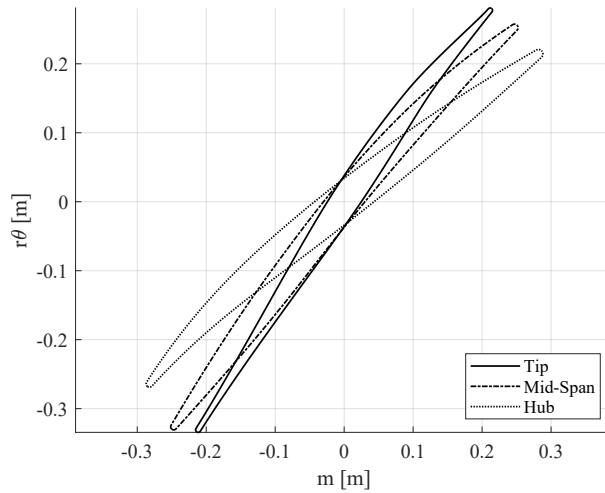
Figure 2.1: Baseline blade sections at the tip (100% span), mid-span (50% span) and hub (0% span).

2.2 Parametrization

In engineering optimization tasks, the input variables often refer to the geometry of the components being optimized. Given the complexity of turbomachinery shapes, achieving complete control over the blade shape would require regulating each point that composes it. This would overly complicate the problem due to the large number of variables involved. To solve this, the geometries are described using a parameterization method. This approach facilitates effective control of the shape by adjusting the positions of only a few "control points," thus mitigating the complexity of the problem.

In the field of turbomachinery, Bézier Curves and B-splines are widely employed as parameterization curves, with the latter used in this study. Particularly, cubic B-splines (degree 3) were used due to their balance between flexibility and computational efficiency. A cubic B-spline curve is a composite curve, constructed by smoothly joining adjacent segments of polynomial curves. The curve is defined by a set

of control points $\{P_0, P_1, \ldots, P_n\}$ with $n \geq 3$ (our variables), and a set of basis functions. The control points define $n - 2$ adjacent cubic curve segments. The basis functions are defined from a non-decreasing sequence of real numbers $\{t_0, t_1, \ldots, t_m\}$ called knots where for cubic functions $m + 1 = n + 3$. In general, the points of the control polygon do not belong to the curve. This happens only if the multiplicity of the nodal value is equal to the degree of the curve. The cubic B-spline function is defined as follows:

$$B(t) = \sum_{i=0}^{n} N_{i,k}(t) P_i \tag{2.1}$$

where k is the degree of the polynomial and $N_{i,k}(t)$ are the cubic B-spline basis functions. This is the final function of the curve. The basis functions are computed recursively as:

$$N_{j,1}(t) = \begin{cases} 1 & \text{if } t_i \leq t < t_{i+1} \\ 0 & \text{otherwise} \end{cases} \tag{2.2}$$

$$N_{j,k}(t) = \frac{t - t_j}{t_{j+k} - t_j} N_{j,k-1}(t) + \frac{t_{j+k+1} - t}{t_{j+k+1} - t_{j+1}} N_{j+1,k-1}(t) \tag{2.3}$$

Finally, between successive curves, second-order continuity is guaranteed: the last point of the first curve coincides with the first point of the second curve, and at these two points there is the same tangent (first derivative) and curvature (second derivative).

2.2.1 Parameterized Geometry

To uniquely describe a profile, two methods are possible. The first one is to parametrize separately the suction side and the pressure side with two different curves. The second way is to reconstruct the airfoil by using a curve for the camber line and another curve for the distribution of thicknesses. In this study, the second strategy was used to avoid the generation of profiles with intersecting suction and pressure sides.

The geometry is parametrized using 8 DV. The first six $(x_1, ..., x_6)$ control the Camber line by describing it in the m'-β space, where β denotes the angle between the tangent to the Camber line and the axial direction while m' refers to the coordinate defined as:

$$m' = \int \frac{\mathrm{d}m}{r} \tag{2.4}$$

where r is the radius. The Camber line is parametrized using a cubic B-spline cure, with 6 control points, as shown in figure 2.2. Each of the first six decision variables controls the positions of the control points along the β axis, thereby influencing the shape of the profile.
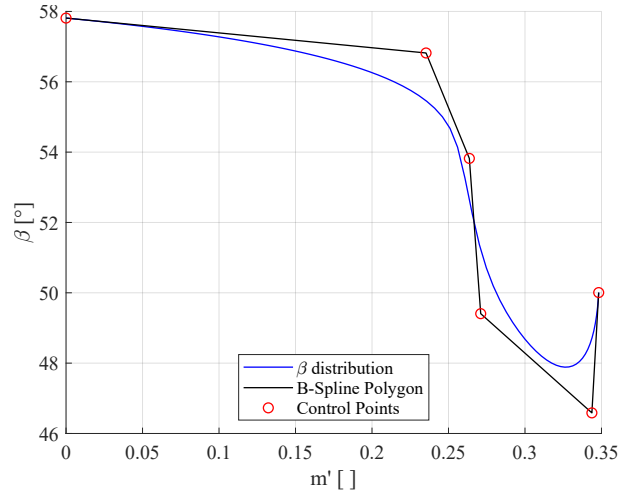
Figure 2.2: Parametrization of the Camber line of the baseline at the tip.

The thickness distribution is parameterized in the $t - m$ plane, where t is denotes the thickness and m the meridional coordinate. A cubic B-spline curve with 6 control points is used, as visible in figure 2.3. The second, third, and fourth points (marked as red circles in the figure) are the only ones that can be moved. In particular, the 7th decision variable (x_7) controls the position of the maximum thickness by changing the m coordinate of these three points. The value of the maximum thickness is controlled by x_8, which changes the y-axis position of the third and fourth points.
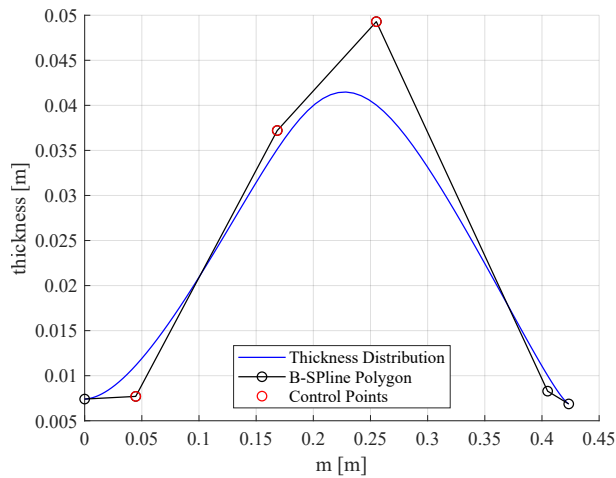
Figure 2.3: Parametrization of the thicknesses distribution of the baseline at the tip blade section.

Finally, the DV are defined as variations in the position of the control points from their original positions in the baseline. The variables do not directly represent the values of the final angle or thickness but instead, quantify the deviation of each individual from the baseline values.

In tables 2.2 and 2.1 the boundaries of the DV are presented.

Camber Line Variables [°]						Thickness Variables[]	
-4.5	-4.5	-4.5	-4.5	-4.5	-4.5	0.0	-1.00
4.5	4.5	4.5	4.5	4.5	4.5	1.0	0.40

Table 2.1: Decision variables boundaries for the tip blade section optimization. Final values.

Camber Line Variables [°]						Thickness Variables []	
-6.5	-6.5	-6.5	-6.5	-6.5	-6.5	-1.0	-0.4
5.5	5.5	5.5	5.5	5.5	5.5	1.0	0.5

Table 2.2: Decision variables boundaries for the mid-span blade section optimization. Final values.

2.3 Optimization points

In optimization problems, deciding which and how many objective functions to optimize is always important. An error in selecting the OF can lead to results that are completely incorrect or not useful for the specific problem. The determination of the number of objective functions to minimize or maximize during optimization also involves a trade-off between achieving control over the desired outcome and the number of evaluations necessary to find the solutions. As more objectives are chosen, locating the absolute minimum of the function within the feasible region becomes progressively more challenging. Additionally, objective functions can be calculated at a single design point (Single-Point Optimization Problem (SPOP)) or multiple design points (Multi-Point Optimization Problem (MPOP)) extending the computational time per individual.

Since the objective of this thesis is to identify profiles capable of handling inflows with distorted total pressure distribution, a two-objective multi-point optimization problem is implemented. The first objective selected is the η_{pol} at design conditions, while the second objective is the TPR under near-stall conditions.

2.3.1 Objective one: η_{pol}

The first objective chosen is the polytropic efficiency (η_{pol}), which is calculated using equation 2.5. This OF is selected to ensure that the cascade operates efficiently under design conditions.

$$\eta_{pol} = \frac{k-1}{k}\log\left(\frac{p_{t2}}{p_{t1}}\right)\Big/\log\left(\frac{T_{t2}}{T_{t1}}\right) \tag{2.5}$$

Where k is the specific heat ratio, equal to 1.4, p_{t2}/p_{t1} is the TPR and T_{t2}/T_{t1} is the Total Temperature Ratio (TTR). The subscript "1" stands for upstream of the cascade while the "2" stands for downstream.

The simulations of the first design point are conducted at a static back pressure of $p_2 = 42000 Pa$ and at a rotational speed of $100\%\omega$. This combination of p_2 and ω was used as design conditions during the construction of the baseline.

2.3.2 Objective two: TPR

The second objective is chosen to optimize the performance of the cascade when operating with an inflow partially composed of the boundary layer section. The entry of a boundary layer through the fan causes a distorted distribution of the total pressure at the inlet, resulting in a reduced stall margin. This reduction is evident from the downward shift of the surge line in the compressor map. For this reason, as the second objective, it is decided to maximize the total pressure ratio (TPR) at a near-stall condition to improve the stall margin of the cascade. Since the optimization is conducted at various blade spans, different techniques are used to induce the stall condition in the respective blade sections.

Tip Blade Section

The relative inlet flow at the tip blade section is supersonic. In this condition, a bow shock is formed at the leading edge of the blade and it is composed of two branches. The first one enters the passage, and it is called passage shock. The second branch is the outer one, and under low supersonic conditions, it exits the cascade. Indeed, the flow reaching the cascade is deviated by this outer shock, meaning that the incidence angle depends solely on the Mach number for a given cascade geometry. This condition is called "unique incidence" and is maintained until the flow on the blade surface reaches a subsonic condition.

To recreate the near-stall conditions searched for the evaluation of the second objective function, it was necessary to exit from the unique incidence. For this reason, a study of the influence of the simulation input parameter was conducted to find the best settings to recreate the desired conditions. The individual chosen for this study was not the baseline but a profile generated from a previous Design of Experiment (DOE) study, as it exhibited greater stability than the baseline when subjected to changes in environmental conditions. The parameters altered during the study were the rotational velocity ω, the absolute inlet flow angle α, and the static back pressure. The results of the three studies are summarized in figure 2.4, in particular, the graph represents the trend of β when Mach changes, where β is the angle of the relative flow at the inlet.
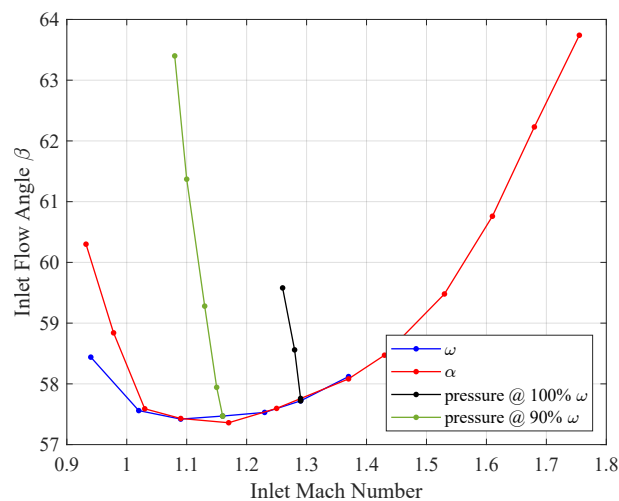
Figure 2.4: Trend of the inlet flow angle, varied using different approaches to exit from the unique incidence condition.

The overlapping of the α and ω curves reveals how the unique incidence condition begins at approximately Mach 1.05 and persists for higher Mach numbers. With these parameters, it was necessary to decelerate the flow to almost subsonic to exit from the unique incidence conditions. For the pressure lines, the results were different. Its increase allowed to exit from the condition of unique incidence while maintaining the inlet velocity almost unchanged thanks to the expulsion of the passage shock. Consequently, the flow in front of the profile became partly subsonic and can adapt to the presence of the cascade. The expulsion of the shock also allowed the mass flow to reduce and this is why the Mach number slightly changes. The variation of the inlet angle occurred very rapidly with the rise of pressure, as visible in figure 2.5. In the picture, the static back pressure is normalized with respect to the inlet total pressure, which remains the same for all the simulations.
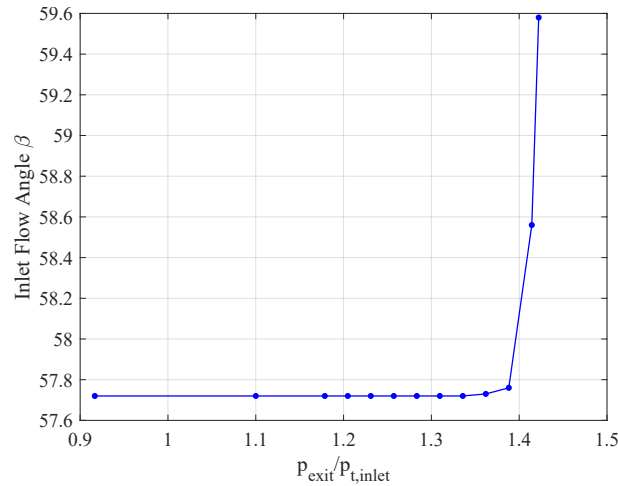
Figure 2.5: Trend of the inlet flow angle, varied for the rise of back pressure at ω 100 %.

Varying the back pressure was found to be the most effective technique for changing the incidence of inflow at each Mach inlet. The near stall condition was obtained by increasing the back pressure ratio to a value of $p_{exit}/p_{t,inlet} = 1.304$ and by reducing the rotational speed to 90 % of ω. This last was slowed to change the inlet Mach number from the first design point. The value of the back pressure was decided by looking at the residuals of the simulation. In particular, it was chosen the last pressure whose residuals remained stable (did not explode).

Mid-Span Blade Section

For the mid-span blade section, two optimizations were performed and the difference lies in the definition of the stall conditions.

The first optimization used the same strategy of reducing the rotational velocity and increasing the back pressure to simulate the near-stall conditions as at the tip blade section. In particular, ω was 90% of the nominal value while the back pressure was $p_2 = 43300 Pa$. How this pressure was chosen will be explained later in chapter 3.

For the second optimization, a different approach was chosen. Studying the stalled profiles, a common trend observed was the variation of the incidence angles from the design condition ($\Delta\beta$). In particular,

when the $\Delta\beta$ of the airfoils was around 4°, the flow conditions were similar. Instead, when applying the same back pressure to all the cascades, as in the first optimization, the final incidence angles differed among the profiles, resulting in different flow conditions. Namely, not all the profiles were exactly stalled. Because the objective of the second design point was to replicate stall conditions in all profiles, the imposition of an incidence angle at the inlet instead of a constant back pressure resulted in more similar stall conditions.

Since the final goal of the second design point simulation was to impose the inlet flow angle, it became necessary to establish a correlation between this angle and one of the input parameters. Several combinations were tested, and the most effective was to correlate the variation of the flow angles ($\beta - \beta_{design}$) to the ratio between the static back pressure and the total back pressure under design conditions ($p/p^0_{exit,design}$). This approach ensured that the characteristic curve of the profiles had a similar trend, enabling prediction of the pressure to be used to obtain the desired β. The resulting curves of the three profiles used to determine the method are presented in figure 2.6. In particular, the selected individuals are the baseline and two profiles from the initial LHS sample.
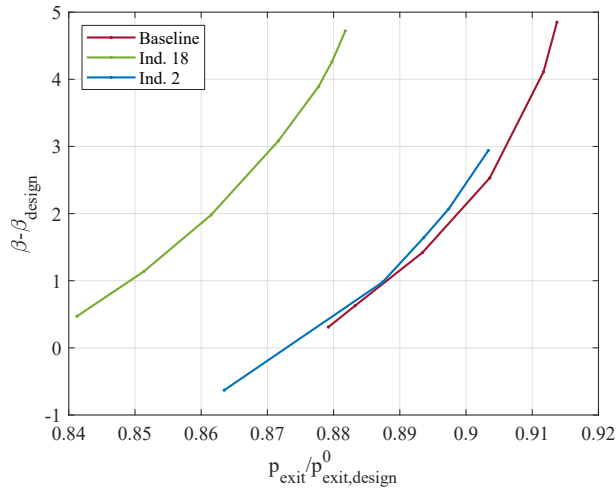
Figure 2.6: Correlation between the difference of the inlet flow angle and the ratio of static back pressure and total back pressure for the baseline and two individuals from the LHS study.

Although the curves did not align perfectly, the trends were similar. In particular, after interpolating them with cubic functions, it was observed that the curves were very similar but only shifted along the x-axis.

From this knowledge, a four-step algorithm was created to achieve the desired $\Delta\beta$. These steps are:

1. The first simulation of the near-stall conditions was performed using a fixed back pressure for all the individuals. This was necessary to get a first point on the $p/p^0_{exit,design}$ vs $\beta - \beta_{design}$ plane.

2. For the second evaluation, the backpressure was determined by assuming that the curve followed a similar trend as that of Individual 2 in figure 2.6. This was because the interpolation function of Individual 2 was an average of the other two functions. Therefore, the second point was determined by shifting the interpolation function of Individual 2 along the x-axis and calculating the pressure ratio that made the $delta\beta$ equal to 4°.

3. For the third evaluation, it was decided to use the acquired knowledge of the function by creating a quadratic function that interpolates the available points. In particular, since three points were needed to uniquely define a quadratic, the value of the coefficient of the squared term was imposed. With this function, the new simulation point was predicted.

4. For the third simulation, another quadratic function was created, but since three points were available, there was no need to choose coefficients.

The algorithm stopped if an individual reached a $\Delta\beta = 4 \pm 0.2$, considering the current simulation as the final. Finally, in this strategy, the rotational velocity was reduced as in the other simulations, to change the inlet Mach number.

2.4 CFD Model

The high-fidelity evaluations of the objective functions were obtained through CFD simulations of the individuals proposed by the optimizer. The software used was Ansys CFX [14] due to its good performance in simulating turbomachinery and easy controllability from an external code. The CFD code solves the Reynolds-averaged Navier–Stokes (RANS) equations. Since this work focused on the shape of the single profile, the meshes were created as bi-dimensional over the meridional plane of the specific blade section and then, one element was extruded along both the directions orthogonal to the plane. In this way, the simulation was seen as 3D by the software but the results were almost the same as a 2D code since there were no variations along the radius. The meshes were structured multi-block with an H-type topology and were generated using the software Ansys Turbogrid. The inlet and the outlet of the domain were positioned far enough from the profile in order not to influence the fluid flows near the profiles. An example of mesh can be seen in figures 2.7 and 2.8.
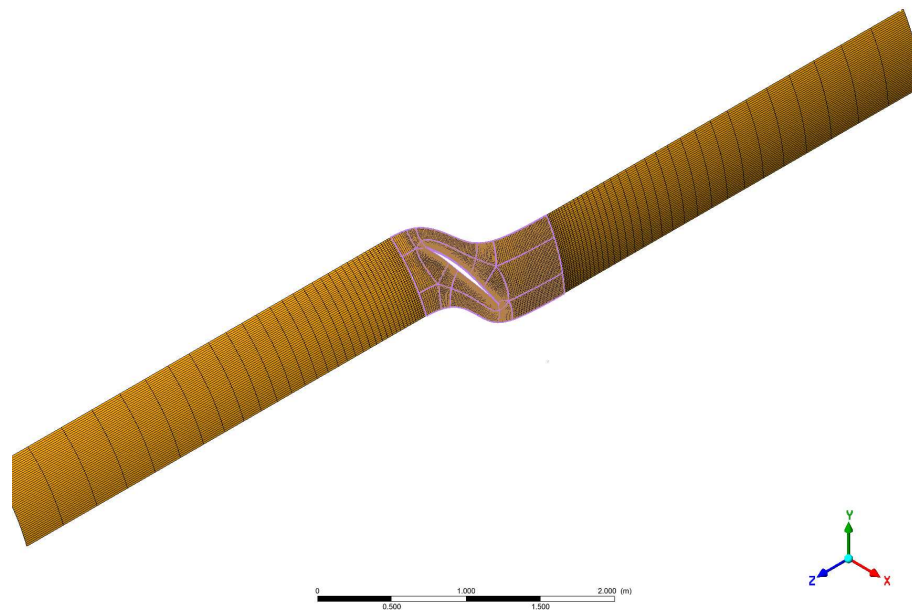
Figure 2.7: Mesh extra course of the baseline at the tip blade section, isometric view. Inlet is on the right.
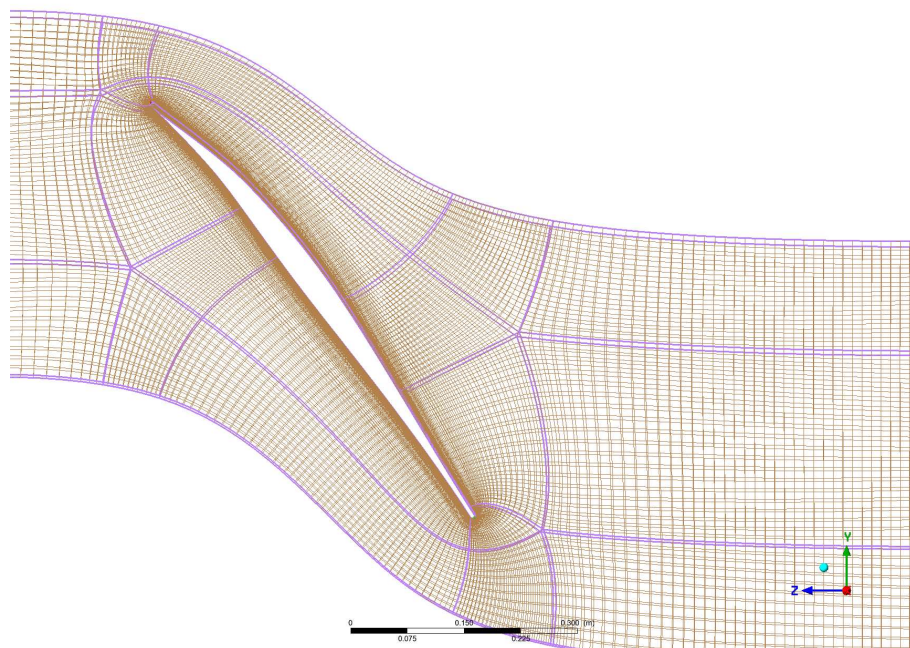
Figure 2.8: Mesh extra course of the baseline at the tip blade section, circumferential view. The inlet is on the right.

The simulations were performed by imposing the total state at the inlet of the domain, the rotational speed and the static pressure at the outlet. With this strategy, the convergence speed increases compared

to the case in mass flow control, however, the continuity must be verified afterwards. During the optimization, the different design points were characterized by the same stagnation values at the inlet whereas the other parameters were changed as explained before. The total pressure at the inlet was $38180Pa$ while the rotational speed ω was $271.45rad/s$. To close the problem of the turbulence, the $k-\omega$ SST model was chosen. Every individual was simulated at 3 different working conditions and depending on the considered blade section, different conditions were used. For all the blade sections, the first simulation was used to initialise the solution and avoid the formation of flow recirculations. The second CFD evaluation corresponds to the first design point while the 3rd was performed at near stall conditions.

2.4.1 Mesh Sensitivity Analysis

The effectiveness of the results obtained in a CFD analysis depends firstly on the quality of the mesh. If the number of elements is not sufficient at points where the flow has many variations, the results obtained will not describe the actual flow. On the other hand, too fine a mesh would lead to too long a calculation time for the aim of this thesis. For these reasons, a mesh sensitivity analysis was conducted to identify the minimum number of mesh nodes needed for the solution to converge. The study was made only for the tip blade section and the same mesh was used for the mid-span optimization. In this study, four meshes were generated by doubling the number of nodes each time, as shown in table 2.3. The extra course mesh was reported in figure 2.8 while in figure 2.9 the fine mesh is reported.

Mesh	Extra Course	Course	Medium	Fine
Number of Nodes	60000	125000	250000	500000

Table 2.3: Number of odes for each mesh
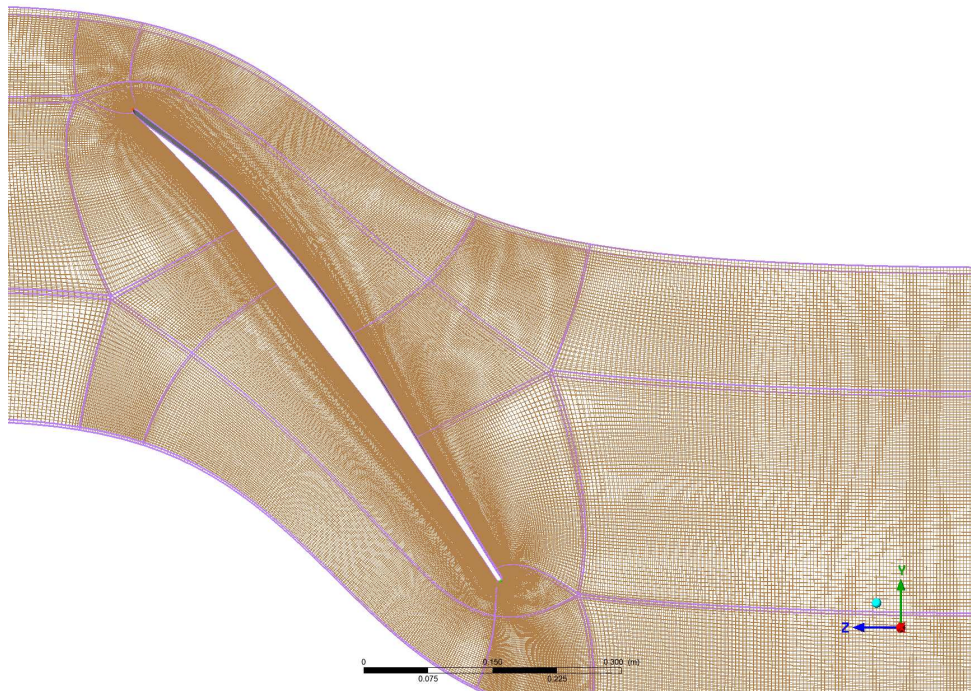
Figure 2.9: Mesh fine of the baseline at the tip blade section, circumferential view. Inlet is on the right.

To check the convergence of the mesh, three important quantities were analyzed: mass flow, TPR and TTR. Since the mass flow is not imposed it was important to check the continuity. The TPR and TTR are two quantities directly utilized during the optimization process, so it was important to ensure their convergence. The results of the analysis are listed in the figures 2.10 (a), (b) and (c), reporting respectively the trends of mass flow, TPR and TTR. From figure 2.10 (a) it is visible that, the steady value is reached from the Course mesh for the first design point and at the Medium mesh for the design point 2. It is important to note that because the scale of the figures is magnified to facilitate an understanding of the trends, the differences between the solutions appear larger than they are. Namely the difference between the last solution and the first is 0.4%. In the TPR and TTR figures, the differences between the different meshes are smaller than in the mass flow case. The percentage difference between the last solution and the first one is less than 0.1% in both design points. In figure 2.10 (d) the simulation time per individual is presented. It is visible how the time scales almost linearly with the number of nodes.
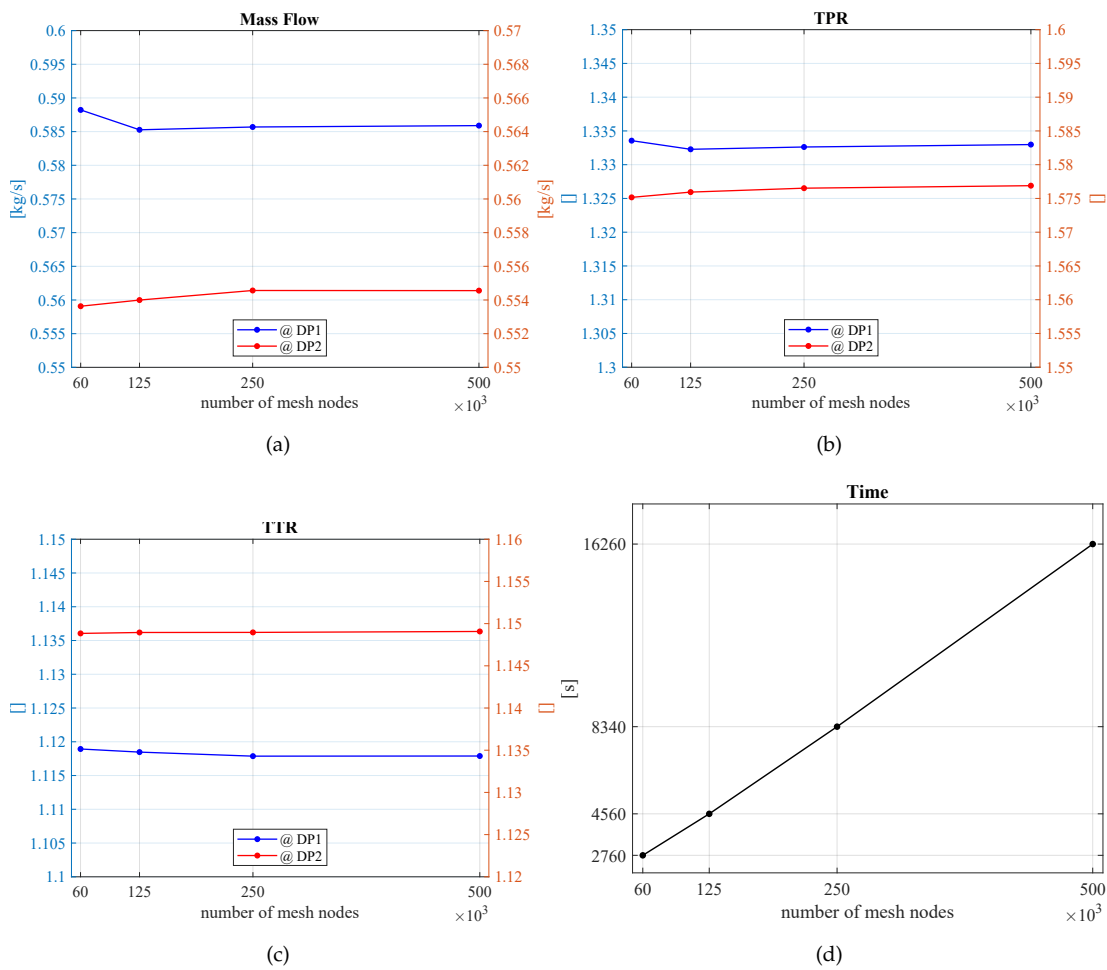
Figure 2.10: Resutls of the mesh sensitivity analysis. (a) Mass flow, (b) TPR, (c) TTR, (d) Simulation time

The mesh chosen for this analysis was the extra course since it was the fastest in terms of computational time while maintaining almost the same results as the others.

2.5 Optimization Problem

Implementing the optimization process is crucial for achieving desirable outcomes. It involves selecting the right optimizer and configuring it appropriately, as well as ensuring seamless integration with other software components responsible for evaluating the objective functions (OF).

In the problems regarding fluid dynamics, due to the high complexity of the fundamental equations, the fitness functions are usually highly distorted, non-continuous and with many local stationary points. Due to this, the mathematical expression of the OF is unknown and it is possible to know the solutions of only a few combinations of DV. Moreover, due to the high computational cost of each evaluation, it is not possible to map the design space with a lot of points. For these reasons, optimizers used for CFD problems must arrive at the optimal solution with the minimum number of evaluations (exploitation), but

also consider the entire design space to avoid reaching a local minimum/maximum point (exploration). Formally, what an optimizer does is find the best combination of DV **x** that minimizes the objective function $f(\mathbf{x})$, i.e.

$$\mathbf{x}^* = \underset{\mathbf{x} \in \mathcal{X}}{\arg\min} f(\mathbf{x})$$

where $\mathcal{X}$ is the design space, in other words, is the feasible space of the DV and $\mathbf{x}^*$ is the optimum of the function. In multi-objective problems, there will be a set of optimal individuals instead of one. These are all the solutions that belong to the Pareto front that, by definition, is made up of all and only the non-dominated solutions (solutions that cannot be improved in any objective without degrading at least one of the others). Therefore, the role of the optimizer is to find the global Pareto set of the specific problem where it is used.

There are many different types of optimizers, from very simple to complex and each of them has its pros and cons. One classification can be made by dividing them according to whether they directly optimize the fitness function or a surrogate function, which is a new function created using the current knowledge of the real functions. For the first case, the most common algorithms are GA that creates a current population by mixing the genes of the best individual from the previous population. In this case, decisions are made only using the actual values of the OF. Even though they are very good at solving multi-objective problems the number of evaluations of the objective functions rapidly increases with the increase of the number of variables. On the other hand, algorithms that optimize a surrogate function, like BO, are designed to reach the optimal solutions with fewer iterations, becoming interesting for the cases where the evaluations of the OF are expensive. In this case, decisions are not made by using only the high-fidelity data but a surrogate model of the objective functions is created to speed up the optimization. This latter represents the low-fidelity model that the optimizer uses to decide the next points to be evaluated with the high-fidelity model. One of the problems with these types of strategies is that the loop and the code are more complicated than in one of the GA. Furthermore, there are new 'default variables' put into place to predict the behaviour of the real functions, increasing the time needed to set the initial parameters.

Since the purpose of this thesis focuses on finding features that unify profiles suitable for distorted transonic inflows, it was decided to utilize the second optimization technique to expedite the process. The strategy chosen is called BO and hereafter there is an overview of how it operates.

2.5.1 Bayesian Optimization

Bayesian Optimization BO is a family of advanced optimization strategies that use Bayesian Inference as a fundamental principle. In brief, Bayesian statistics uses the current knowledge of a sample to estimate the proprieties of the population, and then, when new pieces of information are available, it updates the proprieties. This feature helps to minimize the number of evaluations required to reach the final results, making it particularly useful for problems where evaluating the objective functions is costly. Optimizers using Bayesian inference vary in their approaches and may exhibit small or large differences from each other. Nevertheless, they all follow the same basic structure when addressing optimization problems.

The optimization problem begins with an initial exploration phase where a sample of the DV space is created. Common sampling techniques used to generate the initial population are random search or Latin Hypercube Sampling (LHS). This sample is evaluated and the results represent the initial knowledge from which we infer the propriety of the entire population. These sets of DV and OF are used to train the

regression models which are usually based on GPS These models approximate the objective functions used in the search for the minimum, commonly referred to as surrogate models or low-fidelity model.

Bayesian optimization relies on an acquisition function to decide which point in the search space should be evaluated next. This function acts as a guide to decide where to sample the next point for evaluation. For multi-objective problems, one of the most used acquisition functions is the Expected Hypervolume Improvement (EHVI), used also in our case. This function takes as input the regression models and calculates the improvement that a proposed solution makes on the Pareto front. To calculate the improvement, the function uses a reference point that is assumed to be dominated by the population. In our case, the reference point has values of the objective functions 0.49 and 0.99. At each iteration of the optimizer, the next individual is selected by maximizing the acquisition function with a sub-optimization problem. This is evaluated with the high-fidelity model and the results are used to update the GPS. The new surrogate functions are then used to select a new individual using again the acquisition function. The new individual then is evaluated with the high-fidelity model and the GPS are updated again. This process is repeated with the regression model being refined with each new observation. This method of iteratively updating the surrogate model and intelligently selecting points to evaluate, allows the optimizer to gradually converge towards the optimal solution, achieving this goal with fewer evaluations of the costly objective function when compared with conventional optimization approaches. In figure 2.11, the flowchart of the Bayesian optimizer loop is reported.
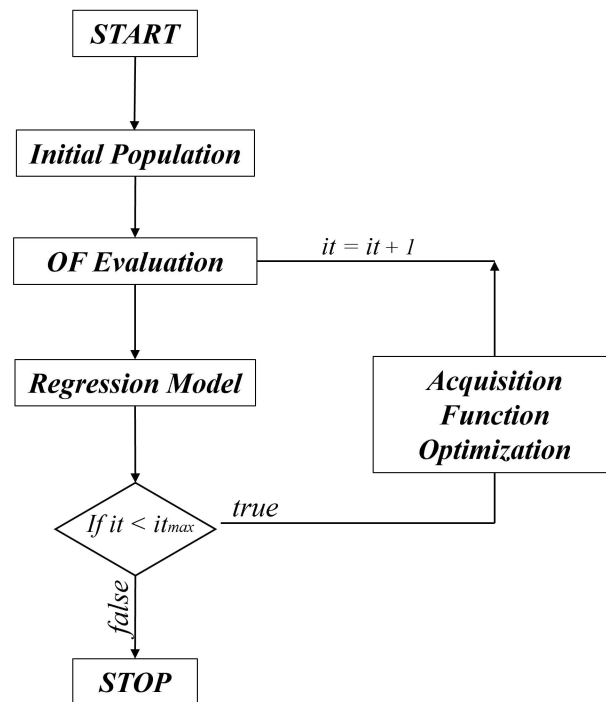
Figure 2.11: Bayesian optimization loop.

2.5.2 Genetic Algorithm

Genetic algorithms are a family of optimization algorithms inspired by the principles of natural selection and genetics. They are used to solve optimization problems by emulating the process of natural selection in biological systems. At every iteration, a population of individuals is created taking the best from the previous one. This new set of individuals is then evaluated using the expensive fitness functions and the score is then assigned to each individual. The creation of a new population is done by using the genetic operators. These operators are the key components that drive the evolution of the population. The three usually used are, in order:

- Selection, ensures that better solutions are more likely to be chosen as parents

- Recombination, combines genetic material from selected parents to create offspring with potentially improved characteristics

- Mutation, introduces stochastic variation to explore new regions of the search space

These play a key role in getting the right balance between exploration and exploitation of the optimizer so the choice of which type of operator to use is very important. There are also other operators used to reach the desired balance of the algorithm and the right implementation of them can speed up the solution with a reduced risk of falling in local stationary points. Finally, these particular types of algorithms are particularly well-suited for multi-objective optimizations since they evolve a generation of individuals at a time. For this reason, they are widely used in engineering problems.

2.5.3 Optimization Loop

The optimization loop used during this study was composed of both a Bayesian optimizer, which works how it was described previously, and a Genetic Algorithm optimizer. This decision was taken mainly to increase the exploitation of the surrogate model. For the initial 80% iterations (where iterations correspond with the number of individuals simulated), the algorithm worked like a normal BO. The next individual to be evaluated was decided by the EHVI functions which in our case was maximized using a particle swarms optimizer. After 80% of the total iterations, a GA optimization was introduced. The algorithm alternated one optimization cycle with the BO and one with the GA. This latter started to work optimizing directly on the surrogate model. Since the problem had two objectives, a Pareto front of individuals was generated by the GA. The individual selected for the evaluation was the furthest from the actual Pareto. This parallel optimization started only when more than 80% of total iterations were performed to have a more realistic model of the objective functions since more data were available. This optimization loop used is presented in figure 2.12.

The entire loop was controlled by MATLAB including the parameterizer. Our two objectives were initially intended to be maximized. However, because the algorithm assumes minimization problems, the sign of each objective was changed, transforming the problem into a minimization one.
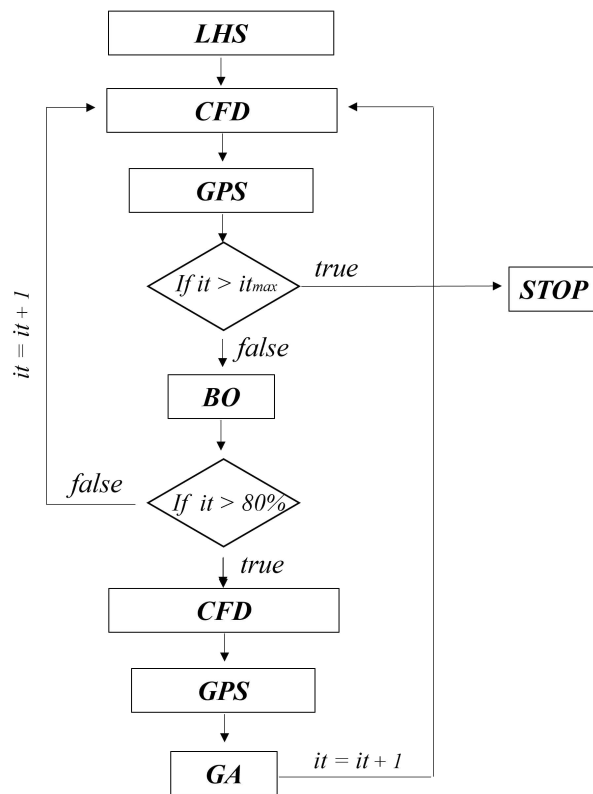
Figure 2.12: Optimization loop used for the optimizations.

3 RESULTS

This chapter provides an overview of the analysis results. First, the results obtained at the tip blade section are presented, subsequently, the mid-span results are analyzed.

3.1 Tip Optimization

3.1.1 Baseline

The baseline was simulated to establish a benchmark for the optimization. Additionally, this simulation was used to determine the back pressure for the second optimization point. This point was identified as the pressure threshold at which the residuals remain stable and it was found to be $49.8 \times 10^3 Pa$.

First, in figure 3.1, the profile geometry at the tip is presented.
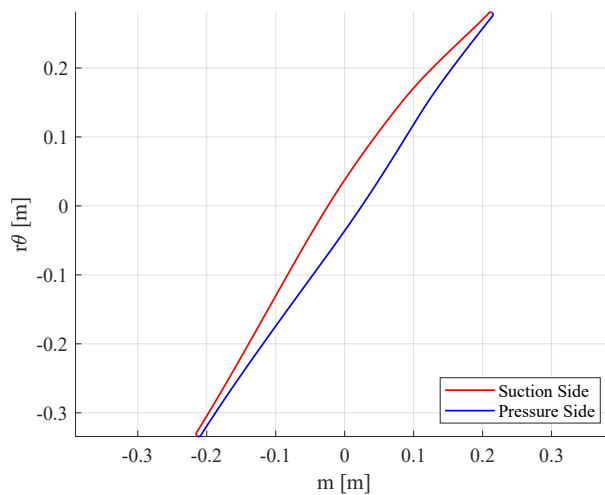
Figure 3.1: Geometry of the baseline at the blade's tip.

The contour plots of the Mach number are then presented in figures 3.2 (a) and (b).

(a)

(b)
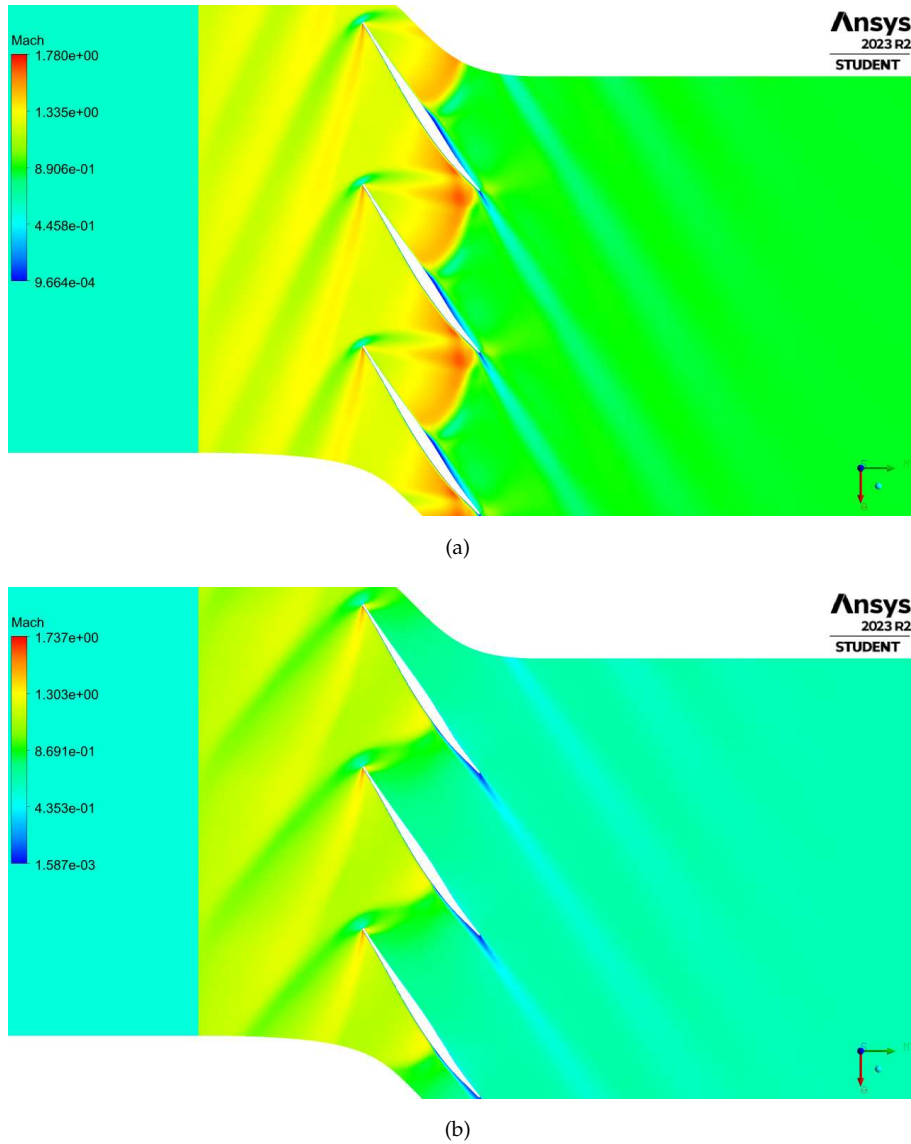
Figure 3.2: Mach contour of the baseline. (a) design conditions (first design point) (b) near-stall conditions (second design point).

In the first picture, the flow field is completely supersonic with the mass flow locked at the maximum level. A detached bow shock is present at the LE of the blade and large subsonic zone forms after this, indicating that the shock is strong and so dissipative. An expansion fan is then formed on both sides of the LE, bringing the flow back to supersonic conditions. The inner branch of the bow shock enters the passage and it is reflected after interacting with the suction side of the previous blade. This reflection creates a passage shock that slows down the flow to subsonic conditions again. The interaction of the second passage shock with the pressure side of the current profile causes the boundary layer to separate. Later on, but due to the favourable pressure gradient, the flow reattached containing the wake losses.

At the second design point (figure 3.2 (b)) the passage shock is outside the cascade and so the mass

flow is no longer locked. The bow shock now is almost normal and no reflections of the inner shock are visible. Two expansion fans are also formed in this case, but they are considerably weaker and tend to dissipate with the interaction of the shock. A small flow separation occurs at the end of the suction side mainly due to the final curvature of the blade.

The objective function results for the baseline are listed in the table 3.1.

η_{pol}	TPR
0.732	1.575

Table 3.1: Baseline at tip objective functions' results

3.1.2 Bayesian Optimization

To start the Bayesian optimization, an LHS study was performed to get a representative initial population. This sample was then evaluated to determine the fitness of each individual. These results were used to train the GPS parameters using a Matlab built-in optimizer. The parameters then remained the same throughout the optimization process. During the optimization, 269 profiles were generated for a total of 301 individuals. Each individual takes about 40 minutes of calculation time and the total optimization was about 8 days to finish. After 56 evaluations the boundaries of the first 6 DV (those who controlled the Camber line) were increased from $[-3, +3]$ to $[-4.5, +4.5]$. This was done because the algorithm started to stagnate along the boundaries, indicating overly strict constraints. The solutions obtained during the optimization are reported in figure 3.3.
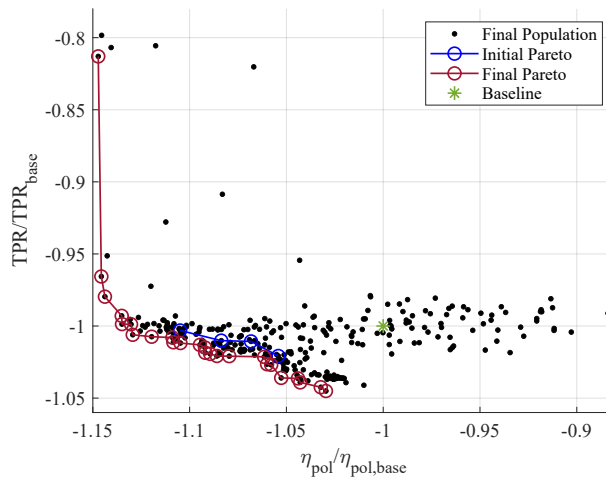
Figure 3.3: Results of the Bayesian Optimization at the tip, normalized with respect to the baseline.

The advancement from the initial LHS solution is small in terms of performance; however, greater improvements have been made over the baseline. The optimizer obtained good results for the first objective, with improvements of almost 15%. On the other hand, the Pareto front advanced less on the TPR axis indicating a difficulty for this objective. Since the simulation of the first objective function was conducted while maintaining a similar TPR, this difficulty is justified.

The performance of the population is presented on the DV space using a colour map. The efficiency is represented in figure 3.4 while the TPR results are shown in figure 3.5.
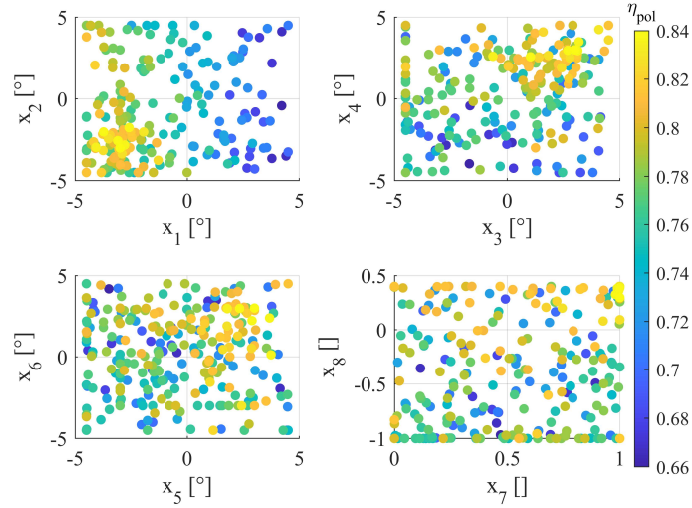
Figure 3.4: Rappresentation of the η_{pol} results of the airfoils in the space of the DV using a colour map. Results after the BO at the tip.
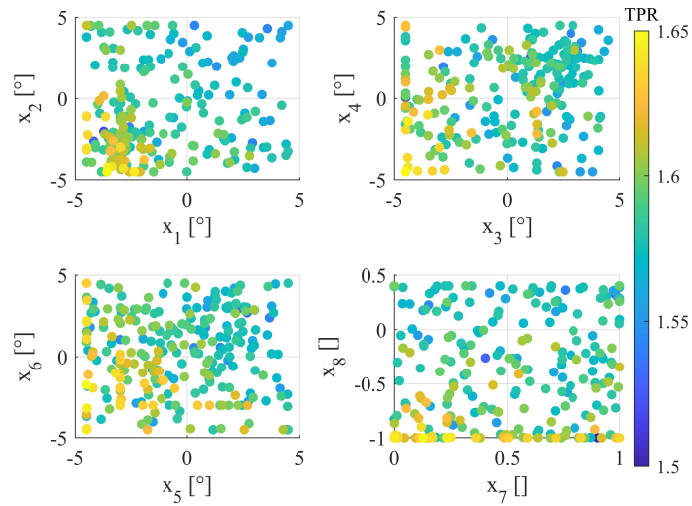
Figure 3.5: Rappresentation of the TPR results of the airfoils in the space of the DV using a colour map. Results after the BO at the tip.

For variables x_1 and x_2 the best individuals are almost all on the bottom left of both of the graphs. This indicates that the leading edge (LE) of the optimized individuals has a lower inlet angle than the

baseline. The variables x_3 and x_4 have opposite behaviour in the two objectives. Positive values of both are preferred for the first objective, on the other hand, the individuals that excel in the second OF have negative values, although the correlation in this latter is weaker. The same behaviour is visible for DV x_5 and x_6 with negative values for high TPR individuals and positive for profiles with good η_{pol}. For the variables controlling the thickness of the profile, some differences are noticeable. The individuals with the best η_{pol} are almost all thicker than the baseline (i.e. positive values of x_8) while airfoils with high TPR are thinner. However good profiles for efficiency can be found also thinner than the baseline while for high TPR a thin blade is needed. No significant correlations are observed for the DV x_7.

To verify whether the optimizer achieved some level of convergence, 5 individuals were selected from the final fitted Pareto. This Pareto was obtained by optimizing the GPS trained with the final population. In particular, the fitted Pareto fronts were found using a GA optimizer. Due to the complexity of evaluating the objective functions, 100000 generations of 100 individuals were generated. The individuals selected were simulated to the real value of the OF. The results of this study are reported in figure 3.6.
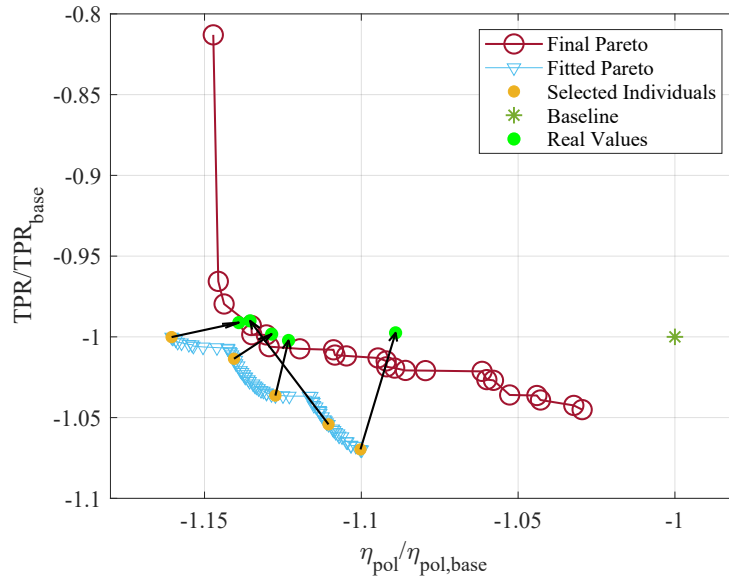
Figure 3.6: Results of the selection and simulations of the 5 individuals from the final fitted Pareto

Form figure 3.6 how the real OF values are still on the real Pareto front, confirming the results of the optimization. The differences between the two final Pareto fronts are mainly caused by the underdefinition of the GPS model.

The uncertainty of the final and initial regression models is studied; figure 3.7 illustrates the disparity between the final predicted values of the objective functions and the actual ones. The predicted values are for the initial and final GPS. The results are presented only for the first objective function (η_{pol}); for the second, results are similar.
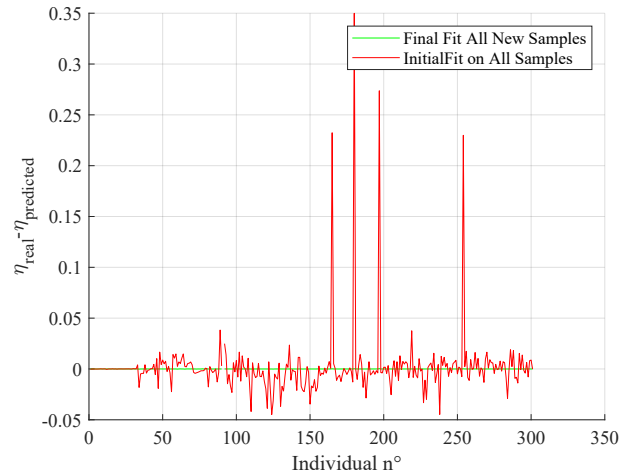
Figure 3.7: Differences between the real values of the first objective function with the one predicted using the first and last regression model.

Although the differences between the final fitted and real Pareto are high, the final GPS show a low final error, visible from the flat green line. These low values (under 10^{-3}) are not unexpected since the model is trained with these data. The red line on the other hand present many spikes, indicating a sensible difference between the real values of the objective function and the predicted.

A study of three different profiles is now conducted to delve deeper into the difference between the optimal solutions. The individuals chosen are reported in figure 3.8. Overall the profiles were selected to perform at least as well as the baseline.
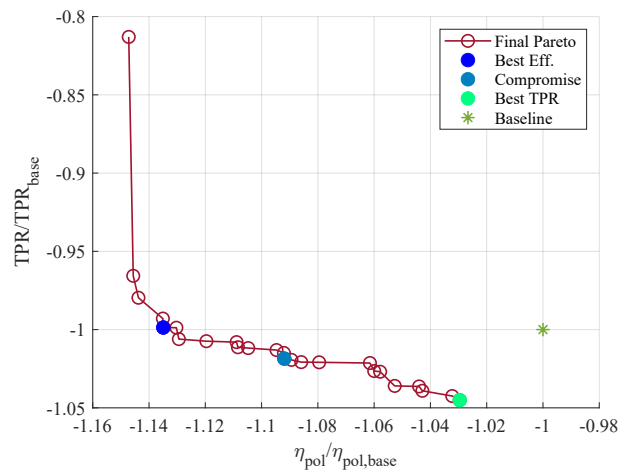
Figure 3.8: Best individuals selected for the study.

Best Efficiency

The first individual studied is the one having the best efficiency and it was created as the 15th profile of the optimization. In figure 3.9 the geometry is visible. The values of the DV and OF are reported in tables
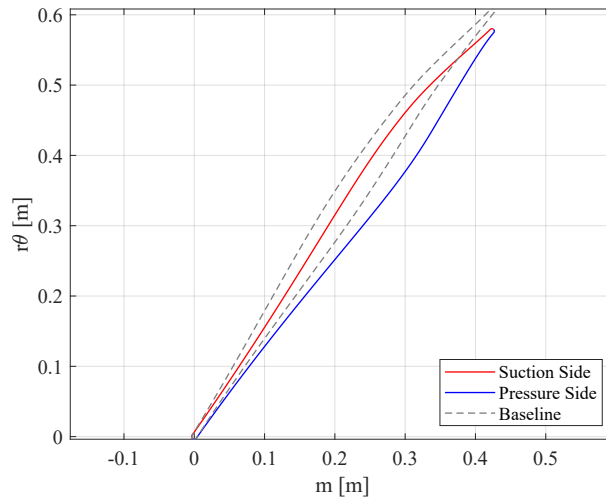
Figure 3.9: Best individual for efficiency.

Camber Line Variables [°]						Thickness Variables []	
-3.00	-3.00	3.00	3.00	2.43	-3.00	1.00	0.40

Table 3.2: Decision variables values of the best η_{pol} profile.

	Value	$\Delta\%$ form base
η_{pol}	0.830	13.42
TPR	1.573	-0.12

Table 3.3: Objective functions values and comparison with the baseline for the best η_{pol} profile.

Looking at figure 3.9 and table 3.2 the profile is thicker and with the maximum moved backwards. The individual was generated before the enlargement, and the values of the decision variables are almost all at the old boundaries.

To understand the difference in performance at the first design point, the relative Mach number contour and the relative total pressure ratio contour are presented respectively in figure 3.10 and 3.11. In particular, the relative total pressure ratio is calculated as the ratio between the total pressure ratio at the specific position and the total pressure at the inlet, both in the relative frame.

Figure 3.10: Mach contour of the individual with the best η_{pol} under design conditions (first design point).

Figure 3.11: Relative total pressure contour for the baseline (left) and the individual with the best η_{pol} under design conditions (first design point). The values are expressed as the ratio between the relative total pressure at the specific position and the relative total pressure at the inlet.

The relative Mach number at which the two cascades work is slightly different with the baseline at 1.23 and the current individual at 1.28. For this reason, efficiency improvements cannot be associated with the weakening of the bow shock. Although the higher velocities, in the best efficiency profile, the back pressure causes the inner branch of the bow shock to shift upstream, leading to the almost complete dissipation of the reflected shock. The interaction between this shock and the SS of the previous blade causes the separation of the boundary layer. This detachment does not occur on the pressure side since no reflection of the shock is present. On the baseline, the separation was only on the PS and hence more controlled than in the current case.

In figure 3.11 is visible how the second passage shock is the leading cause of the efficiency loss on the baseline. Since there is almost no reflection of the bow shock in the optimized individual, this is the main cause of the higher efficiency. in the baseline wake losses are contained since the separation occurs on the PS while on the optimized profile they are higher because the detachment of the boundary layer is on the suction side. Moreover, the bow shock is stronger on the current airfoil due to higher speed than in the baseline. Finally, although larger wake and bow shock losses are present on the optimized profile, the absence of the second passage shock enables the cascade to obtain a higher η_{pol}.

To understand the differences in the performances at the second design point, the relative Mach number contour and the total pressure ratio contour are reported hereafter. Particularly, the total pressure ratio is calculated as the ratio between the absolute total pressure and the absolute total pressure at the inlet, which is the same on both cases.
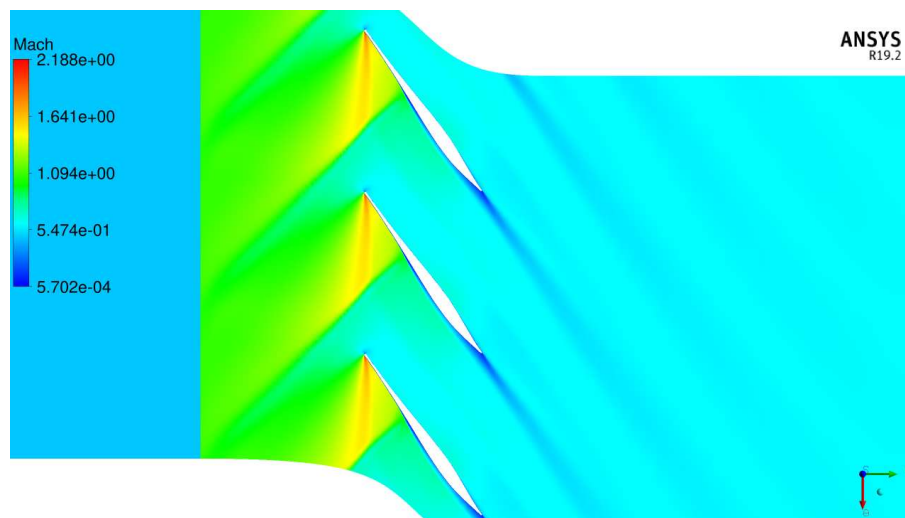
Figure 3.12: Mach contour of the individual with the best η_{pol} under near-stall conditions (second design point).

Figure 3.13: Absolute total pressure ratio contour for the baseline (left) and the individual with the best η_{pol} under near-stall conditions (second design point).

From figure 3.12 this condition, the flow on the optimized profile is more critical than in the baseline. In the current individual, the bow shock shifted upstream, fully detaching from the LE of the blade, becoming almost normal. This shape of the shock is also due to the high incidence of the flow. Looking at the position of the stagnation point this is positioned on the side of the LE. This causes a consistent difference in the velocities between the pressure and suction sides, and the creation of a big expansion fan. This accelerates the flow that is then slowed by the shock. On the other hand, in the baseline, the passage shock was just expelled and the incidence angle was smaller so the conditions were more stable. Overall, the optimized profile looks nearer to the stall conditions than the baseline.

For figure 3.13 it is visible how the presence of the shocks, in both cases, is the leading cause of the TPR increase. This is because the shocks reduce relative velocity and so absolute velocity rises. Moreover, the pressure increases almost instantly through the wave, so overall the total pressure increases. Since the optimized profile is straight, the pressure does not rise while to flow is in the passage. On the baseline, since a small deviation of the flow is present at the back of the profile, a slight increase in total pressure is visible between the blades. The final results are almost identical indicating that the main cause of pressure rise are the shocks.

Overall, the better performance at the first design point is mainly due to the intrinsic characteristics of supersonic profiles. These types of profiles see their efficiency growing while approaching stall conditions and then falling immediately when the stall is reached. Thus, this is the leading cause of the increased efficiency of the optimized profile. In fact, the flow filed at the first design point (figure 3.10) the passage shock is positioned upstream of the passage indicating that the back pressure is already high for this cascade. Moreover, comparing the flow fields at the second design point of both profiles, it is clear that the current individual is in a much more critical condition than the baseline. Finally, although the optimized individual looks better on the two objective functions than the baseline, this is partly because it is working in a near-stall condition and for supersonic profiles this increases the efficiency. Overall, this is still suitable for a BLI application.

Compromise

The second individual studied is the one being a compromise between the two objectives of the problem and it was created as the 258th profile of the optimization. In figure 3.14 the geometry is visible. The values of the DV and OF are presented in tables 3.4 and 3.5.
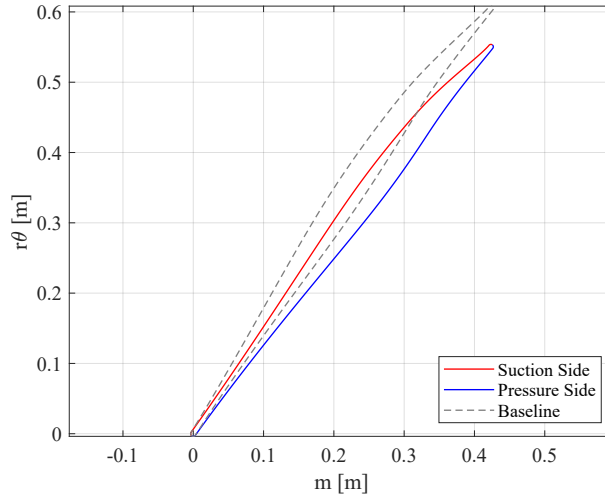

Figure 3.14: Individual compromise between the two objectives.

Camber Line Variables [°]						Thickness Variables []	
-3.41	-3.83	0.26	1.84	-4.49	1.46	0.57	-0.10

Table 3.4: Decision variables values of the compromise profile.

	Value	$\Delta\%$ form base
η_{pol}	0.799	9.12
TPR	1.605	1.86

Table 3.5: Objective functions values and comparison with the baseline for the compromise profile.

The profile has a smaller stagger angle than the baseline and it is slightly thinner with the maximum shifted backwards. In this individual, good improvements have been made for the first objective function while the TPR has improved by less than 2%.

To understand the difference in performance at the first design point, the relative Mach number contour and the relative total pressure ratio contour are presented respectively in figure 3.15 and 3.16. In particular, the relative total pressure ratio is calculated as the ratio between the total pressure ratio at the specific position and the total pressure at the inlet, both in the relative frame.
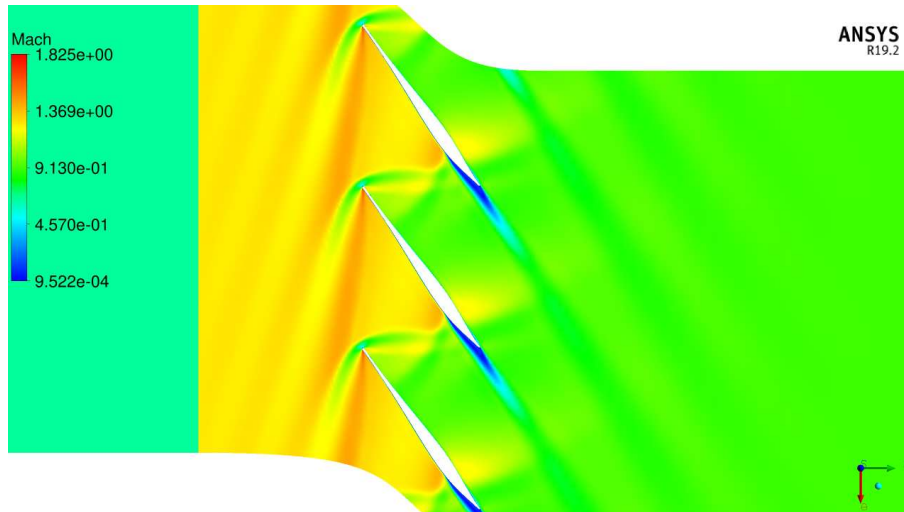
Figure 3.15: Mach contour of the compromise individual under design conditions (first design point).
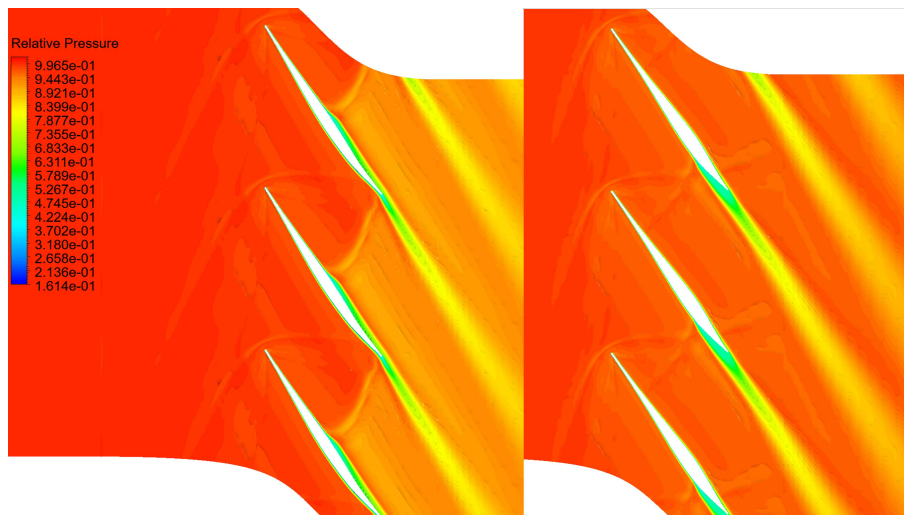

Figure 3.16: Relative total pressure contour for the baseline (left) and the compromise individual under design conditions (first design point). The values are expressed as the ratio between the relative total pressure at the specific position and the relative total pressure at the inlet.

First, it is visible in figure 3.15 how the bow shock has a smaller subsonic zone than the baseline, visible the green zone in front of the blade. This indicates that the shock occurring on the baseline is stronger than on the current profile, and so causes more losses. The reduced subsonic zone is probably caused by the fact that the flow here is faster than in the baseline with a relative Mach number of 1.30 against 1.23. Thanks to the reduced thickness and stagger angle the throat area is bigger and so the flow is faster. As with the baseline, the passage shock is reflected by the interaction with the previous blade in the form of another shock passage. This reflected shock is strong and it decelerates the flow from supersonic to subsonic. The interaction between the previous blade and the inner branch of the bow

shock promotes the separation of the flow at the TE as it happens at the end of the SS. However, thanks to the presence of the expansion fan originating at the leading edge, this separation is contained and the wake losses do not increase drastically. The second passage shock also interacts with the pressure side of the current blade causing a slight separation of the boundary layer. This is more contained than in the baseline thanks to the more favourable pressure gradient created by the profile shape.

Figure 3.16 highlighted that the losses caused by the reflected passage shock in the compromise individual are fewer than in the baseline. In the latter case, the second shock was found to be the leading cause for the loss of efficiency, thus the reduced intensity of this in the current individual is the motivation for better efficiency. On the other hand, the wake losses here are higher than in either of the above cases. This is caused by the partial detachment of the boundary layer on both sides after the interaction with the passage shocks.

To understand the differences in the performances at the second design point, the relative Mach number contour and the total pressure ratio contour are reported hereafter.

Figure 3.17: Mach contour of the compromise individual under near-stall conditions (second design point).
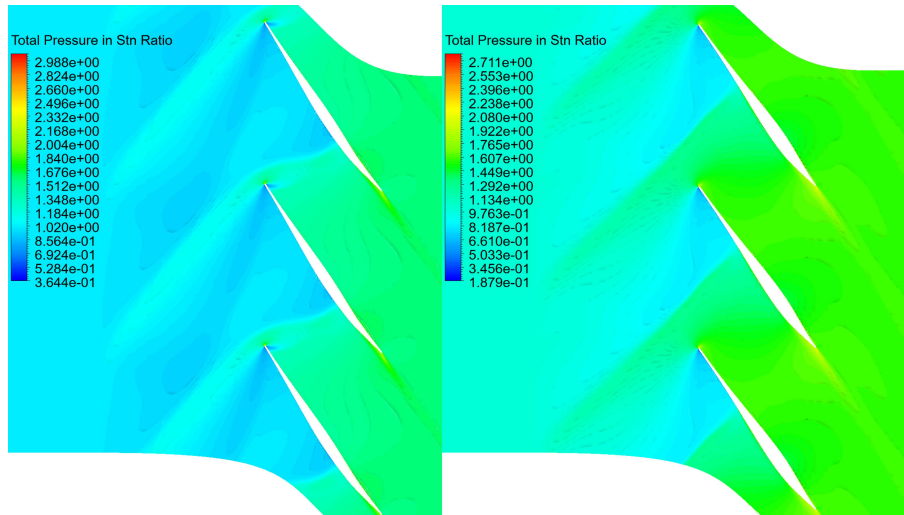
Figure 3.18: Absolute total pressure ratio contour for the baseline (left) and the compromise individual under near-stall conditions (second design point).

The shock pattern here is similar to the individual with the best η_{pol}, but the conditions are more stable. The bow shock is detached from the LE and moved upstream of the blade but it is still a little inclined. On the other hand, in the baseline the passage shock was just expelled and so the conditions were farther from the stall. The incidence angle in the current individual is larger than in the baseline but still, it is well tolerated.

In figure 3.18, as in the previous case, the presence of the shock is the main reason for the increase in the total pressure of both profiles. Because in the current individual, the shock is almost normal, the increase in total pressure is sharper than in the baseline where the shock is curved. Also, the inlet Mach number in the two cases is slightly different. In particular, the baseline has an inlet Mach of 1.10 while the optimized has 1.12 so more kinetic energy is available for the optimized profile. Finally, the increase in TPR obtained throughout the passage is similar, and thus the 2% improvement results almost only from the stronger shock.

Overall, in this case, the profile works better on both objectives. Indeed, for the second design point, the individual achieved a better TPR due to the stronger passage shocks. For the first design point, on the other hand, the profile improved the efficiency by more than 9% mainly due to a reduction in shock wave losses. This latter improvement was mainly caused by a higher throat area. Thanks to the thinner profile, the deviation between the blades due to the contraction of the section was smaller and so the supersonic flow had to deviate less from its normal path. An increase in the wake losses was observed but this still was lower than the shock losses. These latter were considered again as the leading causes of the loss in efficiency. Finally, these profile results are well suited for a BLI propulsion application since sensible improvements are made on both the OF, maintaining stable working conditions.

Best TPR

The last individual studied is the one having the best TPR and it was created as the 96th profile of the optimization. In figure 3.19 the geometry is visible. The values of the DV and OF are presented in tables

3.6 and 3.7.
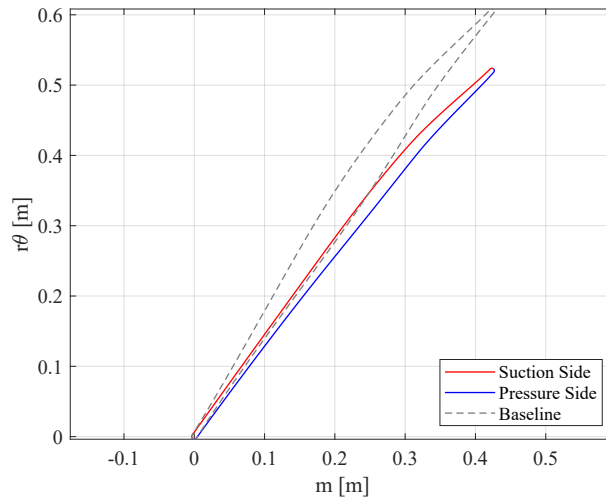
Figure 3.19: Best individual for TPR

Camber Line Variables [°]						Thickness Variables []	
-3.59	-4.50	-4.50	-4.50	-4.50	-1.73	0.13	-1.00

Table 3.6: Decision variables values of the best TPR profile.

	Value	$\Delta\%$ form base
η_{pol}	0.753	2.89
TPR	1.646	4.56

Table 3.7: Objective functions values and comparison with the baseline for the best TPR profile.

The profile is thinner and with a lower stagger angle than the baseline. Looking at the DV, the values are consistent with the overall view given in figure 3.5.

To understand the difference in performance at the first design point, the relative Mach number contour and the relative total pressure ratio contour are presented respectively in figure 3.19 and 3.21. In particular, the relative total pressure ratio is calculated as the ratio between the total pressure ratio at the specific position and the total pressure at the inlet, both in the relative frame.
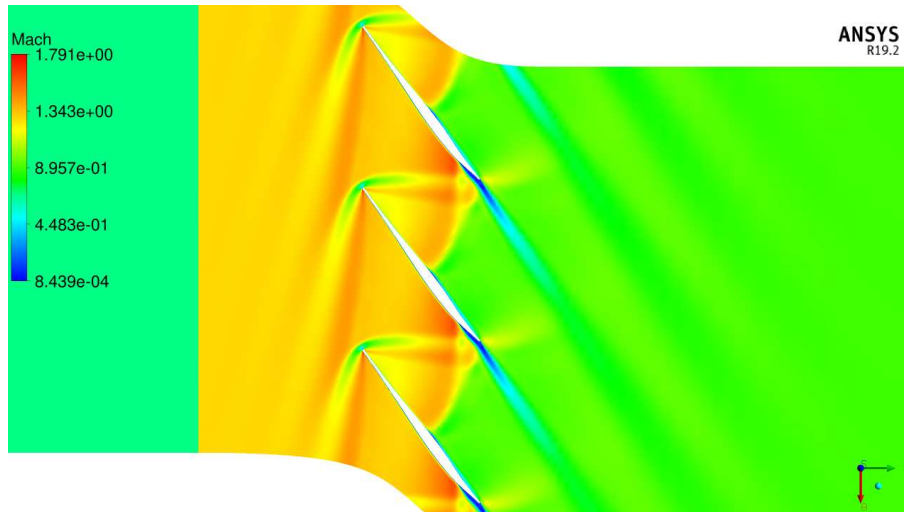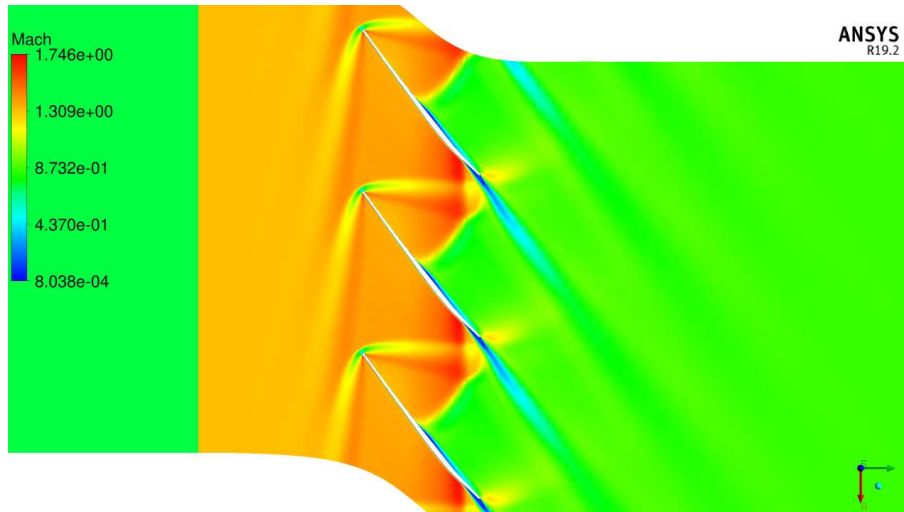
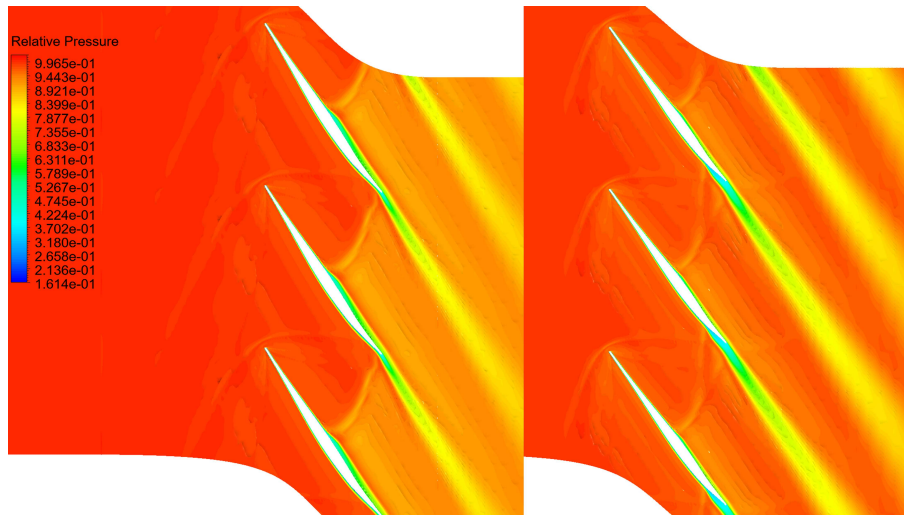Figure 3.20: Mach contour of the best TPR individual under design conditions (first design point).
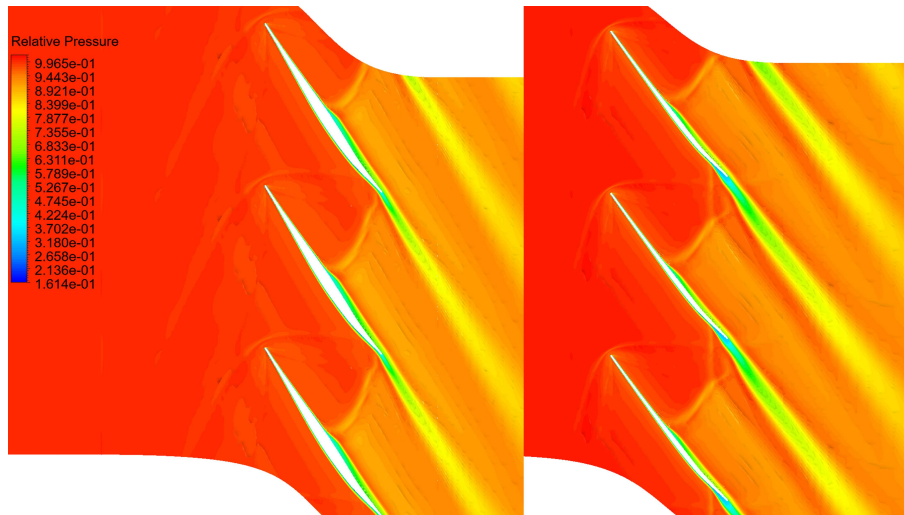
Figure 3.21: Relative total pressure contour for the baseline (left) and the best TPR individual under design conditions (first design point). The values are expressed as the ratio between the relative total pressure at the specific position and the relative total pressure at the inlet.

In this case, the bow shock is almost oblique and the subsonic zone is the smallest of the three individuals. This results in a less dissipative deceleration of the fluid compared to the baseline. However, because the flow entered the blade passage at a higher speed (relative Mach here is 1.32 and 1.23 for the baseline), the second passage shock is stronger than in the previous cases. Moreover, since the first passage shock is oblique, it encounters the previous blade far behind, interacting directly with the wake and not the solid wall of the profile. This causes the detachment of the boundary layer, contained by the presence of the expansion fan. This is not observed on the Baseline. On the pressure side of the current profile, the second passage shock detached the boundary layer but this is reattached later on thanks to

the presence of a favourable pressure gradient. This is more intense in the baseline.

In figure 3.21 is visible that the leading cause of the decrease in efficiency is the second passage shock, as with the previous cases. While in the two profiles, the phenomenology is similar, the shocks generated from the baseline and the optimized profile have a different impact on the relative total pressure losses. In particular, the second passage shock occurring on the baseline is more entropic. This can be associated with the greater thickness of the blade which causes a severe deviation of the flow inside of the cascade. While the passage shock looks worse on the baseline, the opposite occurs for the wake losses. In the optimized individual, the wake interacts with the first passage shock. This causes the growth of a detached flow and the rise of the wake losses. In the baseline, no flow separation occurs since the shock is reflected by a "solid" wall. On the pressure side, the detachment of the boundary layer causes similar losses so they are not the causes of the different efficiency. Overall, the weaker second passage shock is again the leading cause for the higher efficiency of the optimized individual. However, the more oblique bow shock causes, in the current individual, an increase in the wake losses.

To understand the differences in the performances at the second design point, the relative Mach number contour and the total pressure ratio contour are reported hereafter.
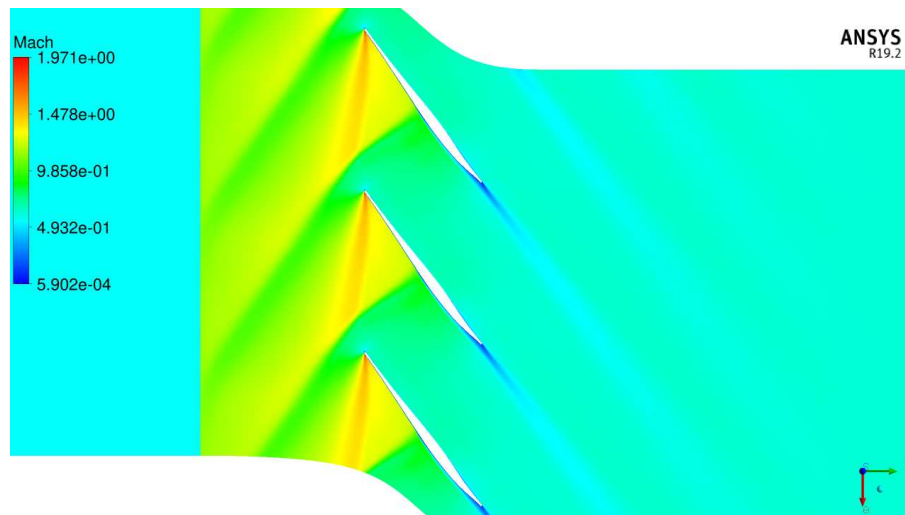

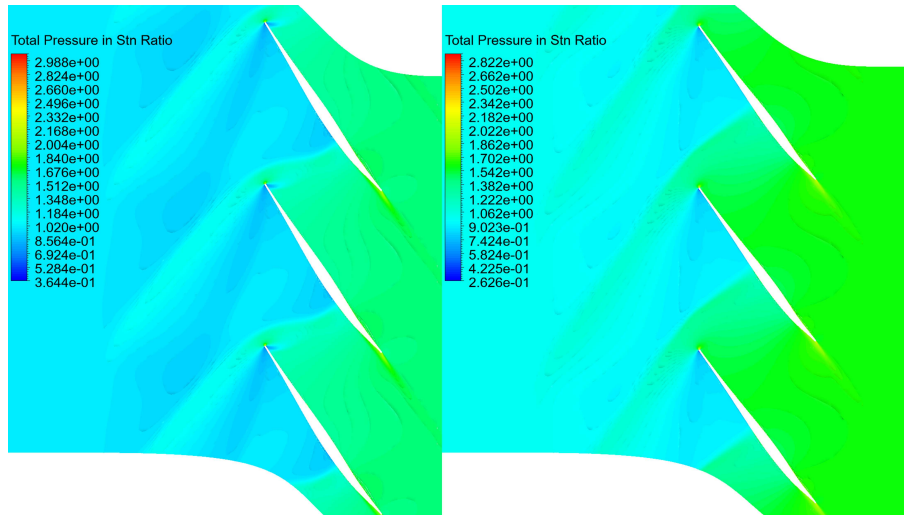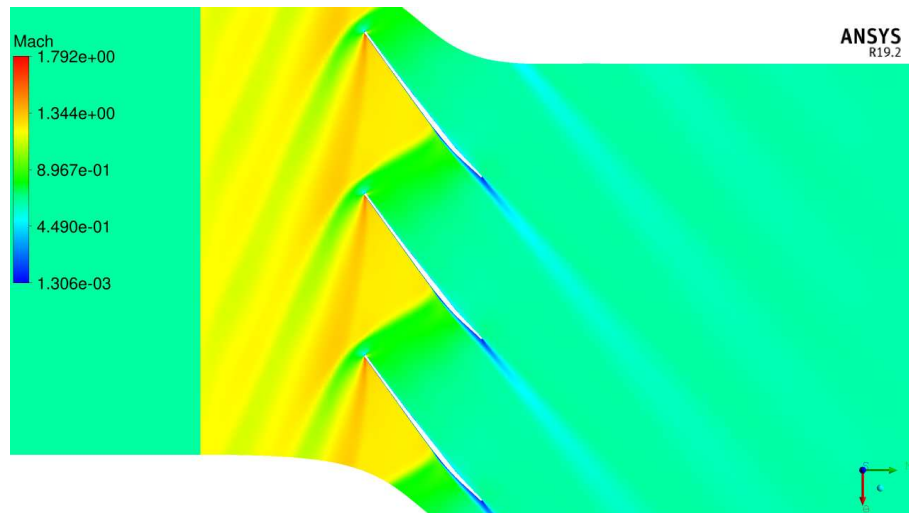Figure 3.22: Mach contour of the best TPR individual under near-stall conditions (second design point).
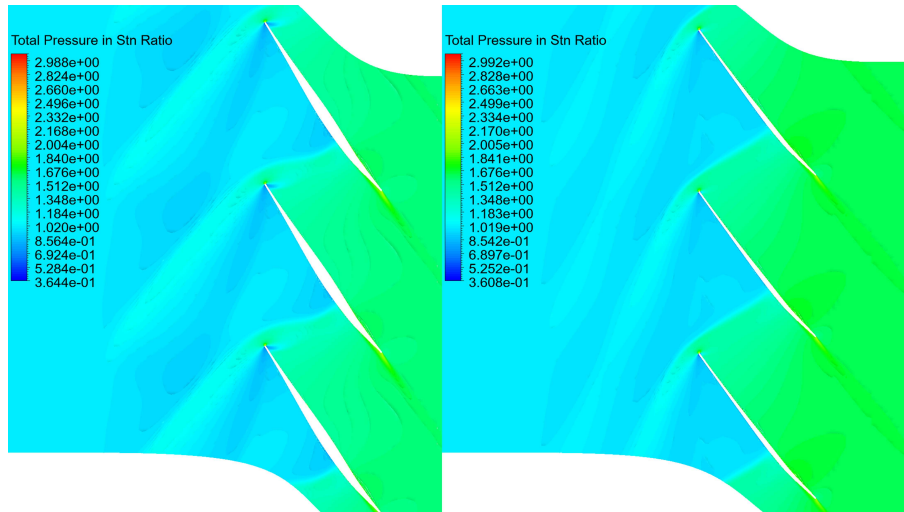
Figure 3.23: Absolute total pressure ratio contour for the baseline (left) and the best TPR individual under near-stall conditions (second design point).

The shock pattern is similar to what was found in the previous individuals. Namely, as expected, the bow shock is outside the passage and almost normal. The condition here is stable and the wake is contained. The stagnation point is positioned on one side of the TE indicating that the incidence angle is not zero. This causes, as in the other profiles, the creation of an expansion fan on the suction side that ends with the bow shock. From the colour map in figure 3.2 (b) and 3.22 it is visible how in the second one, although the scale is not the same, the speed is higher. The relative Mach number is 1.10 for the baseline and 1.18 for the individual with the best TPR.

Looking at figure 3.23 it can be noticed how the passage shocks are again the main reasons for the increase of the TPR inside the passage. The difference in the performance of the two cascades is caused by the stronger shock occurring on the current individual. In fact, due to higher velocities and stronger deceleration, the increase in TPR is higher. Moreover, also the bigger curvature of the final part of the profile increases the pressure ratio due to higher deflections of the flow and hence more energy is exchanged.

Overall, this individual is better than the baseline on both objectives. In particular, since it maximizes the TPR, the profile is well suited for BLI applications. Moreover, the good performance on the first design point enables the profile to reduce energy consumption.

Conclusions

From this study, the weaknesses of the baseline and how the optimizer addressed them were highlighted.

First, in high η_{pol} individuals, since most of the losses were caused by the shocks, the optimizer created individuals with lower throat areas by increasing the thickness while maintaining almost the same stagger angle. This creates profiles nearer to the stall conditions than the baseline. The TPR was maintained equal to the baseline thanks to stronger shock on the optimized profiles.

Individuals with high TPR are thinner and exhibit a curved camber line on the back. They performed well on the second objective, enhancing the total pressure ratio through stronger shocks and partly

deviating the flow. Additionally, efficiency is improved due to weaker second passage shocks at the first design point. This reduction in the strength of the shocks is achieved by a lower contraction of the passage. Thanks to the high stability of these profiles and the enhanced characteristics, they proved to be well-suited for BLI applications.

3.1.3 Comparison between BO and GA

To test the effectiveness of the Bayesian optimizer, another optimization of the same problem was launched using a well-known Genetic Algorithm. The solvers were compared using the same number of evaluations of the objective functions. In particular, in the GA, the population size was set to 15 individuals for a total of 22 generations including the gen. 0 (initial generation), created using an LHS method. The total number of evaluations was set to more than 301 (i.e. number of individuals simulated in the BO) because, during the optimization, any duplicate individuals created are not directly evaluated but the values of the OF are copied. The size of the final population was 309. The algorithm used is called *GeDEA II* [15], a proprietary optimizer of the COMETES research group at the University of Padova. It is a well-proven algorithm and it has the characteristic of focusing on the boundary of the domain to find the best individuals.

First, the results are now shown on the DV space using a colour map, as done in figures 3.4 and 3.5 for the .
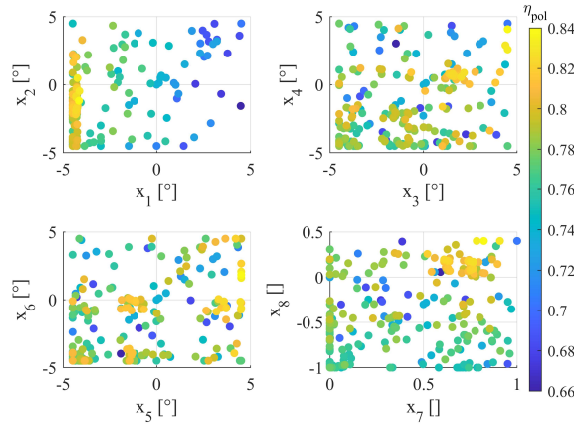
Figure 3.24: Rappresentation of the η_{pol} results of the airfoils in the space of the DV using a colour map. Results after the GA at the tip.
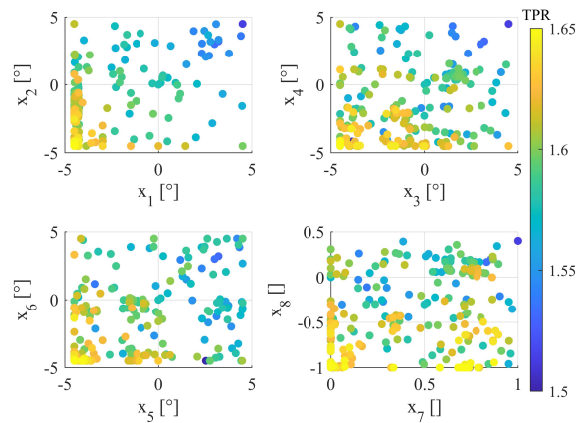
Figure 3.25: Rappresentation of the TPR results of the airfoils in the space of the DV using a colour map. Results after the GA at the tip.

First, it is visible that the optimizer explores the design space less extensively than the BO. This is likely because the optimizer discovers highly favourable solutions in certain areas and persists in searching within them, indicating a preference for exploitation over exploration. Additionally, it is characteristic of the GA used for the comparison to seek solutions, particularly along the boundaries. Overall, the colour map shows results similar to what was found in the previous optimization, confirming the effectiveness of the BO, with a few differences. For example, in the Bayesian optimization, a stronger correlation was found over the x_3 and x_4 DV, especially in the efficiency results where the GA found that almost all design space here could bring good results. For variables x_5 and x_6, a stronger correlation is visible in figure 3.4 than in figure 3.24 probably also due to the less distributed DV on this latter plot. Although these differences exist, the correlation between the results remains high. A comparison between profile geometries will be conducted to confirm the correlation further.

Because the objective of this paragraph is to compare the results of the BO and the GA, there will not be an in-depth study of the results of this optimization but instead, a comparison between the two populations obtained was done. The final Pareto fronts are compared on the objective functions space in figure 3.26.
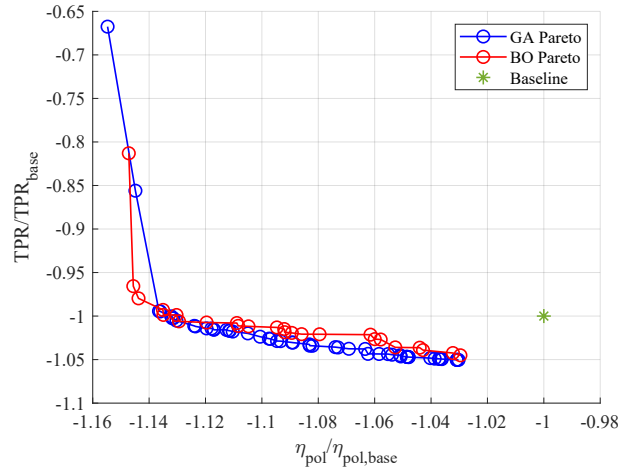
Figure 3.26: Comparison of the final Pareto fronts obtained with the BO and GA optimizers, plotted on the OFs space.

The Pareto from the first optimization is slightly beyond the second Pareto. Furthermore, the Pareto front obtained with the GA is denser than the one of the BO, especially in the zone where the TPR is maximized. Overall, the results from the two optimizations are similar.

To understand how the BO and GA performed during the optimization, the Pareto fronts at different moments are plotted. Since the Bayesian optimiser worked with generations composed of at most two individuals, the results were compared regarding the number of objective function evaluations. More specifically, the results are plotted every 3 generations (45 simulations) starting from generation 0 until the 15th generation. Later generations were not displayed since no significant changes were obtained. The results are visible in figure 3.27.

From figure 3.27 (a) it is visible that the Pareto fronts at generation 0 are different. This is because, in the GA optimization, the boundaries of the DV space were already expanded, so the initial LHS study found better individuals. At gen. 3, the BO already begins to find individuals from its final Pareto, especially in the high-efficiency zone. The front is well distributed across the space with good solutions also for the second objective. In the high TPR zone, the Pareto is still slightly far from the final solution also because at this generation the DV boundaries were not enlarged. Indeed, as seen in the previous section, individuals in this area have a smaller stagger angle compared to the baseline, only obtainable with the enlarged limits. The GA, on the other hand, finds profiles from the final Pareto only in the high TPR zone while not-dominated individuals are not visible for the first OF. At 105 individuals (figure 3.27 (c)), the Bayesian optimizer continued populating the final Pareto almost everywhere, except for the high TPR zone where still the algorithm lacks. This is because the boundaries were just enlarged so new DV space was available and the optimizer used new individuals for exploration purposes rather than exploitation. At this generation, the Pareto GA has grown along the η_{pol} axis and continues to find final solutions only in the lower front. Since Gen. 9 (150 individuals, half of the total optimization, figure 3.27 (d)), the Bayesian optimizer almost reached the final Pareto, finding solutions even with high TPR. In later generations, new individuals tend to thicken the Pareto but not advance it, indicating a convergence of the algorithm. For the GA optimizer, the front continues to grow towards more efficient individuals, but the solution is still slightly far from the final one. New individuals from the final Pareto continue to
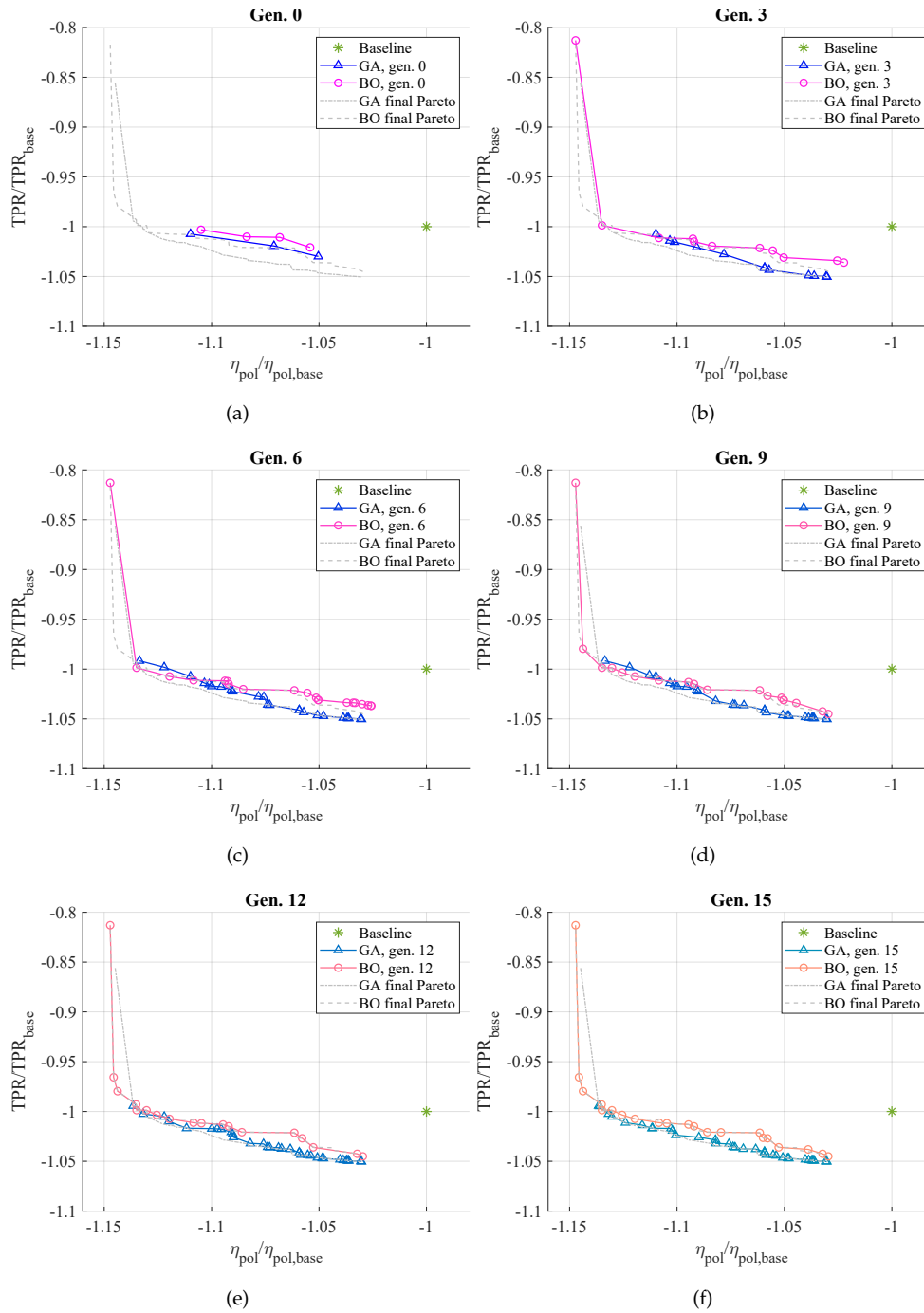
Figure 3.27: Pareto fronts obtained with GA and BO form generation 0 to 15

populate the bottom part of the front. In the next 45 individuals (Gen. 12, figure 3.27 (d)), the Pareto of the GA advanced finding some final solutions with high efficiency. At generation 15 the genetic optimizer almost reached its final solution. Overall, the Bayesian optimizer reached the final solution faster than the GA, although it was penalized by the later boundaries enlargement. Despite this, some individuals of the final Pareto were found before the new limits, but they are only 5 out of 25. Moreover, these are on the boundaries of the first domain, indicating the necessity of the enlargement. Finally, the difference between the two Pareto fronts is probably because the Bayesian optimizer used was a relatively simple version. A better training of the fixed parameter or a different EHVI function can improve the final solution.

To complete the comparison between the two optimizers, the geometries of the 3 profiles used in the previous section are compared with 3 profiles from the GA optimization. The three new individuals were selected to have similar OF values as the other three. In figure 3.28 the profiles selected are reported on the Pareto fronts.
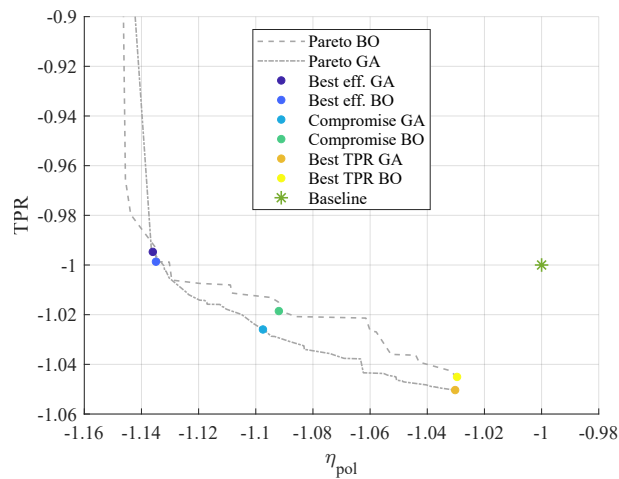
Figure 3.28: Individuals selected for the comparison between the two Pareto fronts.

In figure 3.29, the geometries of the profiles are compared while in table 3.8 the values of the DV on the profiles are presented. Overall both the geometries and the DV are similar in the two cases, confirming the effectiveness of the BO.
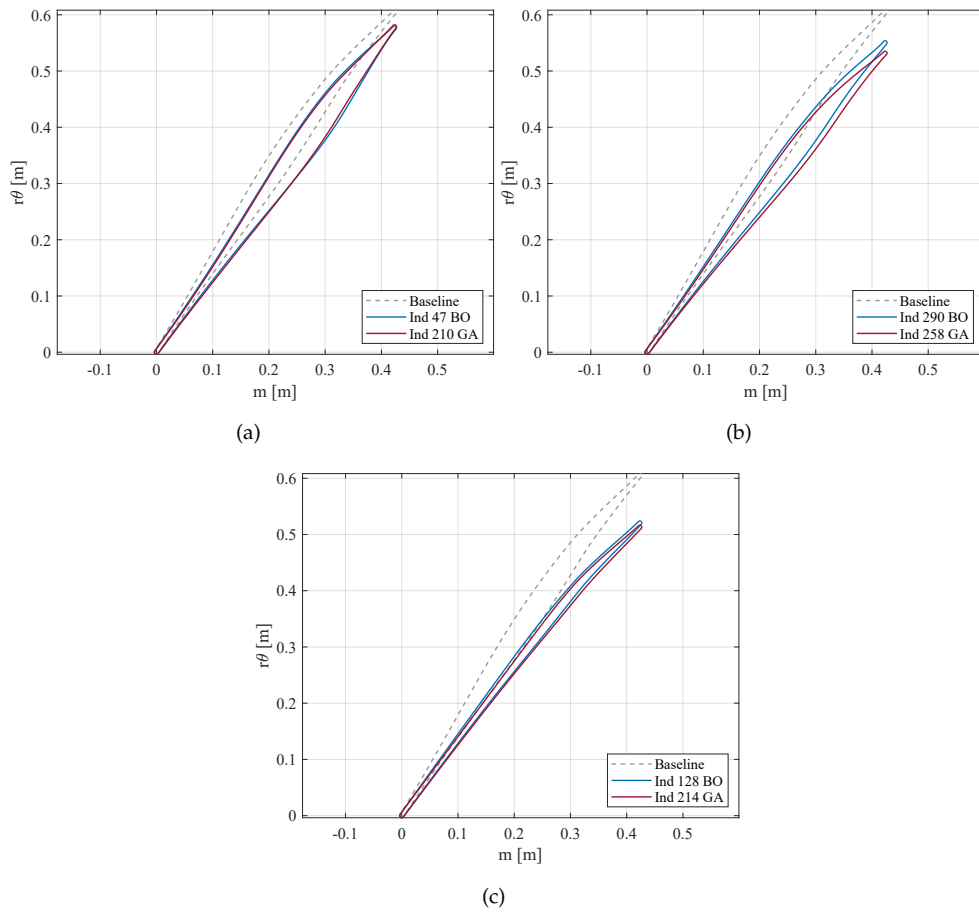
Figure 3.29: Geometry comparison between the individuals obtained form the BO and GA optimization with (a) Best Eff., (b) Compromise, (c) Best TPR

	Camber Line Variables [°]						Thickness Variables []	
Best Eff. BO	-3.00	-3.00	3.00	3.00	2.43	-3.00	1.00	0.40
Best Eff. GA	-4.31	-0.84	2.17	0.88	4.50	-0.62	0.75	0.17
Compromise BO	-3.41	-3.83	0.26	1.84	-4.49	1.46	0.57	-0.10
Compromise GA	-4.50	-3.84	-2.22	1.11	-4.50	-4.50	0.75	0.08
Best TPR BO	-3.59	-4.5	-4.50	-4.50	-4.50	-1.73	0.13	-1.00
Best TPR GA	-4.50	-4.50	-4.50	-4.50	-4.50	-4.50	0.73	-1.00

Table 3.8: Decision variables values of the selected profiles of the BO and GA optimizations.

Conclusions

In conclusion, the performances of the two optimizers are similar, confirming the effectiveness of the BO. Some differences in terms of final results between the two final Pareto fronts are visible and they

are mainly due to the EHVI function and the surrogate functions. These latter contain uncertainties that cannot be completely eliminated. Moreover, despite the differences in the final Pareto fronts, the BO found optimal solutions earlier than the GA. In fact, at 60 individuals simulated (figure 3.27 (b)), the Bayesian optimizer almost arrived at the final front while the Genetic did not explore some space yet. Also, convergence time could be reduced if the initial boundaries were already enlarged, so the algorithm did not lose time in exploring the new working space.

3.2 Mid-Span Optimization

For this blade section, two optimizations were performed, both using the Bayesian optimizer. In the first one, the back pressure was selected as the last that makes most of the profiles of the LHS stall. The choice of checking all the initial profiles and not looking only at the baseline was made because, with the pressure that stalled the baseline, almost half of the simulations of the initial population did not converge. For this reason, the final back pressure was chosen as the highest allowing almost all simulations to converge. A second optimization was launched with the last back pressure chosen looking at the incidence of the blade. The selection algorithm was explained in chapter 2 in the optimization points section.

3.2.1 Baseline

The benchmark used to compare the results of the optimization is the baseline. In this section, the results of its simulations are presented. In figure 3.30, the geometry of the baseline is reported.
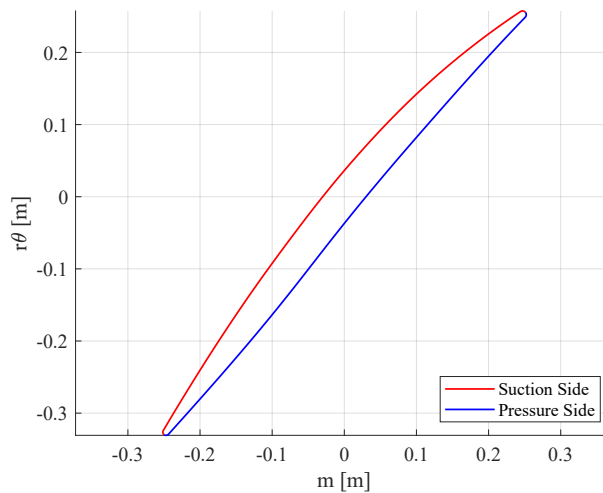
Figure 3.30: Geometry of the baseline at the blade's mid-span.

The contour plots of the Mach number are presented hereafter.
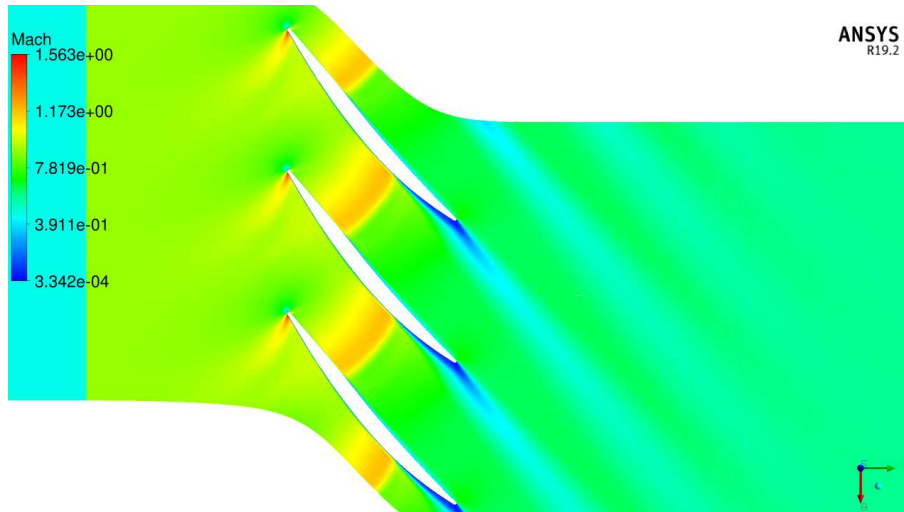
Figure 3.31: Mach contour of the baseline under design conditions (first design point).

In this case, the inlet relative Mach number is 0.90 and so the flow is subsonic. At the LE of the profiles, no bow shocks are visible, however, an expansion fan is present at the beginning of SS. This is because the flow does not enter the passage with zero incidence as visible from the shifted stagnation point. Thanks to the expansion fan and the passage shape, the flow is accelerated till a supersonic condition that locks the mass flow at its maximum level. This acceleration ends with an almost normal shock wave that decelerates the flow to subsonic conditions. The interactions between the shock wave and the suction side of the profile cause the separation of the boundary layer. This is contained and does not deteriorate the blade performance.
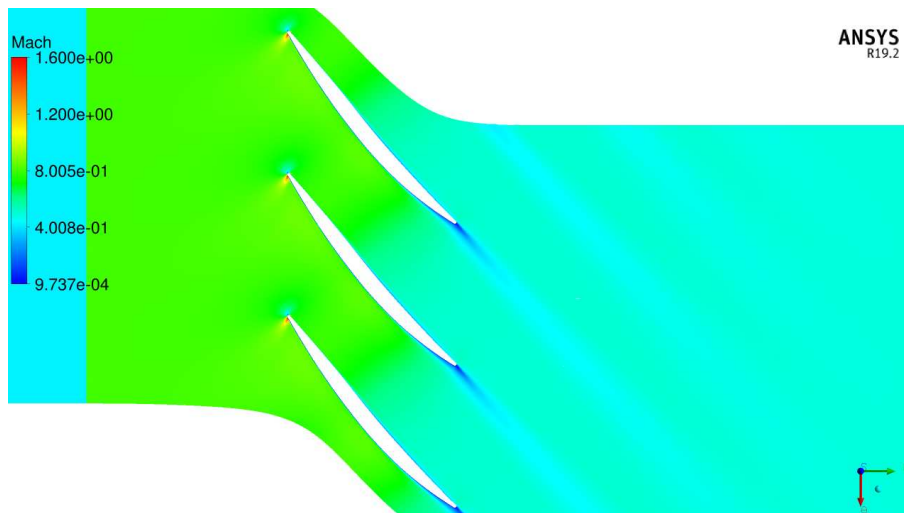
Figure 3.32: Mach contour of the baseline under near-stall conditions (second design point) for the constant back pressure optimization.

Figure 3.32 shows the Mach number contour of the baseline under near-stall conditions for the first optimization. The value of static back pressure of this design point is $43.3 \times 10^3 Pa$. The decrease in angular velocity and the increase in static pressure at the outlet cause the inlet Mach number to decrease to 0.80. Consequently, the passage shock dissipates and the flow field becomes almost entirely subsonic. The inlet flow angle changes by only 0.3° compared to the first design point. Overall, the wake is well-controlled, and the flow is stable.

For the second optimization, the final back pressure obtained was $44.94 \times 10^3 Pa$ with a difference between the flow angle at the design and stall conditions of 4.07°. The final $\Delta\beta$ was reached at the 3rd simulation of the second design point. In figure 3.33 the iterations for the selection of the final back pressure are shown.
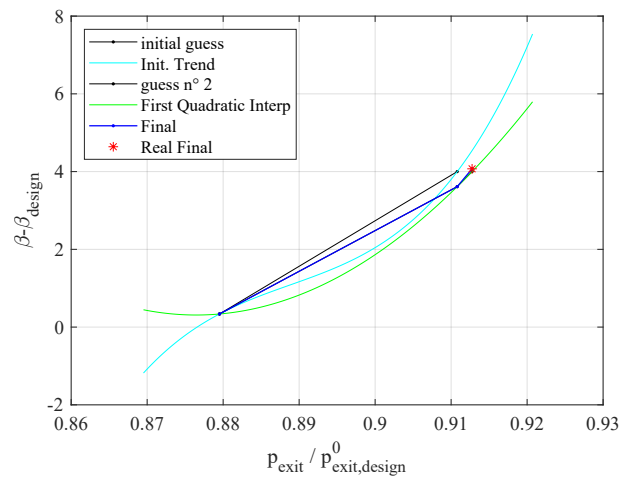
Figure 3.33: Back pressure ratio vs inlet angle of the baseline.

The initial guess made using the imposed cubic function was already accurate. In fact, with the pressure ratio calculated from this, the final $\Delta\beta$ was 3.6°. In the third simulation, the pressure was determined using the quadratic interpolator with one coefficient imposed (the first coefficient was imposed since only two points were available). This approach proved highly effective, allowing to achieve a final $\Delta\beta$ of 4.07°. The relative Mach contour number of this flow field is shown hereafter.
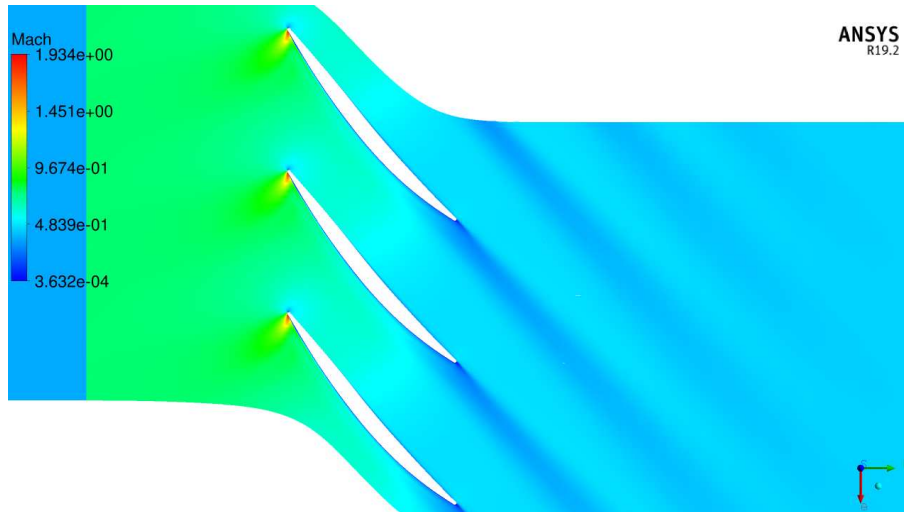
Figure 3.34: Mach contour of the baseline under near-stall conditions (second design point) for the variable back pressure optimization.

In figure 3.34 it is visible that the increase in static back pressure brought the cascade to a much more unstable condition than the previous. The higher inlet flow angle is visible from the shift of the stagnation point near the pressure side. This causes a higher acceleration of the air on the suction side with the formation of an expansion fan. Overall this acceleration is contained and interested only a small part of the flow. Due to the higher incidence, at the end of the SS, the boundary layer tends to separate, increasing the wake losses.

Although with the two strategies, the differences in the back pressure are contained (about $1640Pa$), the flow fields are very different. Also, it is evident, how a small increase in back pressure can drastically deteriorate the flow conditions. For this reason, at this blade section, it was difficult to determine the optimal back pressure for the first optimization. On the other hand, the control of the incidence angle enables the comparison of all profiles in conditions that better represent the stall. The time constraint, due to the multiple simulations needed for the second strategy, was the reason why it was first performed the constant back pressure optimization. In fact, the baseline took less than 40 minutes with the first strategy while using the second it took more than 90 minutes.

The objective function results are then listed in the table below.

η_{pol}	TPR, 1st strategy	TPR, 2nd strategy
0.854	1.306	1.352

Table 3.9: Baseline at mid-span objective functions' results.

The results obtained in this section will be used to understand what improvements the optimized profiles get.

3.2.2 Bayesian Optimization with fixed back pressure

Firstly, an LHS study was performed to obtain the initial population used to train the regression model. 32 individuals were generated and evaluated through the high-fidelity model. The optimization process began with a final total number of direct evaluations of the real objective functions set to 168. This decision was made based on the observation from the tip optimization, where after nearly 150 total evaluations, the improvements of the Pareto front were completed, and subsequent simulations continued to populate the same front. The evaluation of a single individual took 40 minutes on average and the total optimization was complete in about 4.5 days. Thanks to the lower Mach number, this blade section was less critical than the upper one, and so the boundaries of the DV were already taken as the larger used for the tip optimization. However, also in this case the algorithm started to stagnate on the edges of the domain. For this reason, the DV boundaries of the Camber line were increased from $[-4.5, +4.5]$ to $[-6.5, +5.5]$ after 89 total evaluations. The final Pareto front obtained from the optimization is shown in figure 3.35.
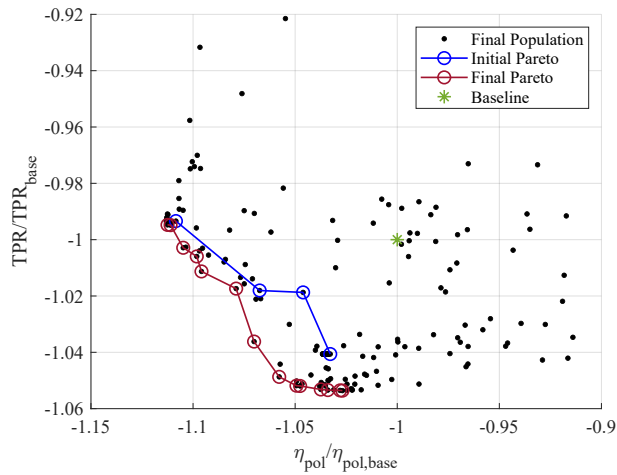
Figure 3.35: Results of the Bayesian Optimization at mid-span, normalized with respect to the baseline.

From figure 3.35, it is noticeable that the optimizer significantly improved both objectives. The final Pareto consists of 14 individuals, with nearly half of them exhibiting a TPR value over 5% higher than the baseline. Moreover, all the not-dominated individuals surpassed the initial profile in terms of efficiency, with the most improved profile achieving an enhancement of over 11%.

The performances of each individual are represented on the DV space using a colour map to understand how best individuals are composed. In particular, the efficiency is represented in figure 3.36 while the TPR results are shown in figure 3.37.
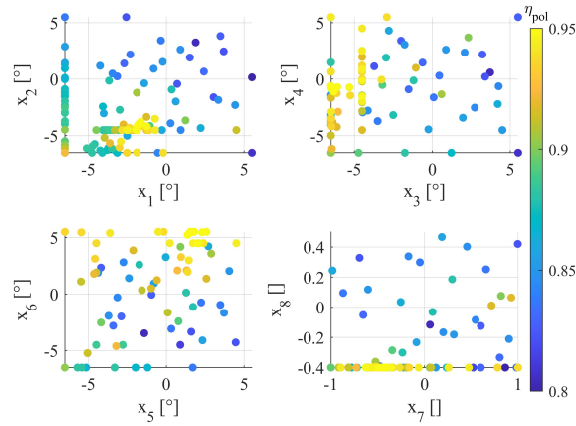
Figure 3.36: Rappresentation of the η_{pol} results of the airfoils in the space of the DV using a colour map. Results after the BO at mid-span using constant back pressure.
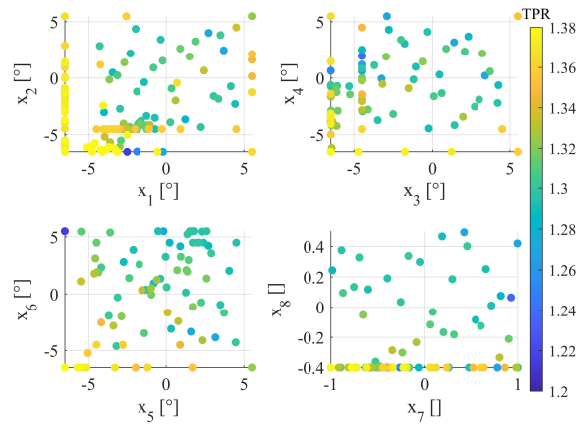
Figure 3.37: Rappresentation of the TPR results of the airfoils in the space of the DV using a colour map. Results after the BO at mid-span using constant back pressure.

First, it can be noticed that the decision space is still too tight since a lot of solutions are stacked at the boundaries of the domain. These should be extended more, but because the optimizer was already improving, it was decided to conclude the optimization with these values. Moreover, some DV could not be enlarged since this would lead to ineligible geometries. For instance, the variable x_8 has all the best individuals at the minimum of its range but, because this controlled the maximum thickness, some structural considerations must be taken. In particular, it was not possible to reduce the variable below -0.4 so all the results were stacked on the boundary. For the first two variables, high-efficiency individuals are all contained in a small area on the bottom left of the graph while for the best TPR profiles the correlation between the two variables and the performance are less clear. The 3rd DV shows a significant trend for the first objective function, with the best individuals having x_3 negative while for the second objective, no correlations between the variable and the function are visible. For variable x_4,

negative values are correlated with good profiles for the second objective function while for the η_{pol} no significant trends are visible. In variables x_5 and x_6 the trend looks opposite between the two graphs. Individuals with the best η_{pol} are on the top right of the graph while profiles that optimize the TPR are located on the bottom left. The variable controlling the position of the maximum thickness along the Camber line (i.e. x_7) does not influence either of the two objective functions. On the other hand, the best individuals have all minimum values of x_8.

To check whether the optimizer reaches convergence or if further improvements are possible, the Pareto, initial and final and real and fitted with the GPS are presented in figure 3.38.
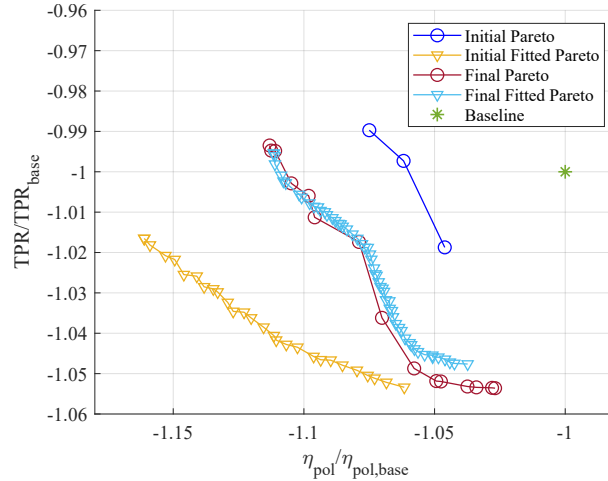
Figure 3.38: Pareto fronts initial and final both real and predicted with the GPS model.

The initial Pareto calculated using the regression model uses the first DV boundaries and despite this, very good improvements were expected. Comparing this with the final obtained it is visible how the initial GPS were not enough accurate in the description of the fitness functions. Looking at both the final Pareto it is evident how the regression model and the real almost match. The differences are mainly because the minimum of the function lies at the edges of the domain and so the function is difficult to explore for the optimizer. Moreover, since the regression functions are highly distorted, the final Pareto of the surrogate functions was calculated imposing to the GA optimizer 2 million generations composed of 160 individuals.

A study of three different profiles is done to delve deeper into the differences between the optimal solutions. The individuals chosen are reported in figure 3.39. Particularly, the individual with the highest TPR is not the one at the edge of the Pareto because near profiles have almost the same value in the second objective function while sensibly improving efficiency.
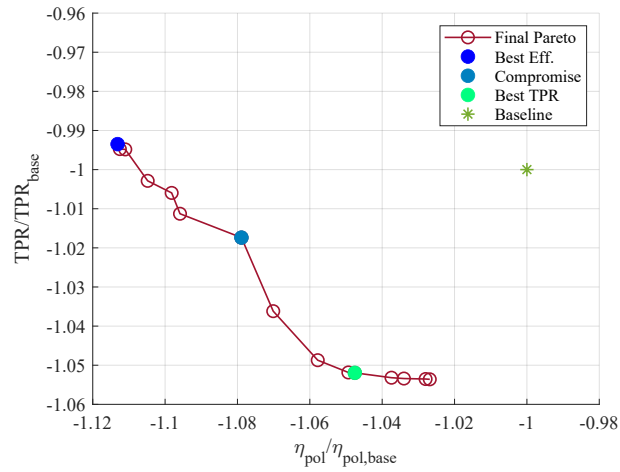
Figure 3.39: Best individuals selected for the study. Mid-span optimization at constant back pressure.

Best Efficiency

The first individual studied is the best efficiency profile. It was created as the 86th (118th of the overall optimization) profile of the optimization. In figure 3.40 the geometry of the profile is presented, while in table 3.10 the values of the decision variables are shown. The values of the OF are then reported in table 3.11.
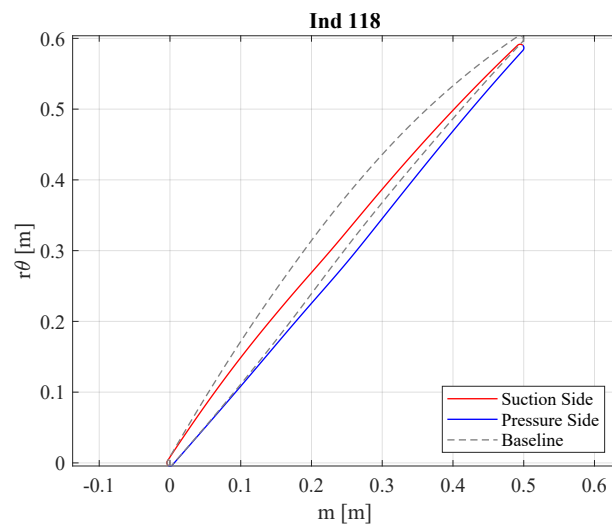
Figure 3.40: Best individual for efficiency.

Camber Line Variables [°]						Thickness Variables []	
-1.64	-3.78	-6.50	-0.62	1.53	5.50	-0.50	-0.40

Table 3.10: Decision variables values of the best η_{pol} profile of the mid-span optimization with constant back pressure.

	Value	$\Delta\%$ form base
η_{pol}	0.950	11.31
TPR	1.297	-0.65

Table 3.11: Objective functions values and comparison with the baseline for the best η_{pol} profile for the optimization at mid-span with constant back pressure.

The profile is thinner and straighter than the baseline similar to a flat plate. This latter is very good in terms of efficiency but lacks compression performance since it almost does not deflect the flow. The values of the decision variables are consistent with what was observed in figure 3.36, with 3 of the 8 DV situated at the edges of the domain.

The Mach number contours at the two optimization points are now analyzed to understand the differences in the performances. First, the contour at the first design point is reported in figure 3.41. To understand the differences in the values of the efficiency, the contour of the relative total pressure ratio is presented in figure 3.42.
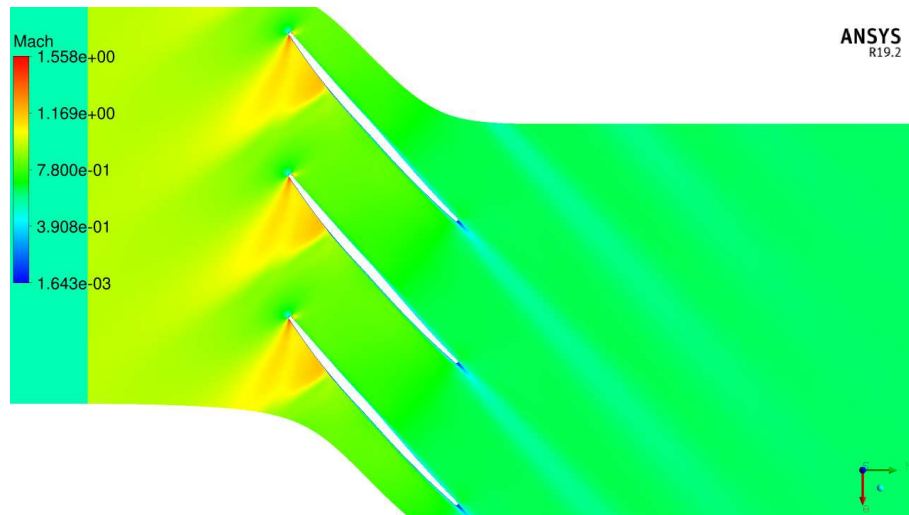
Figure 3.41: Mach contour of the individual with the best η_{pol} under design conditions (first design point).
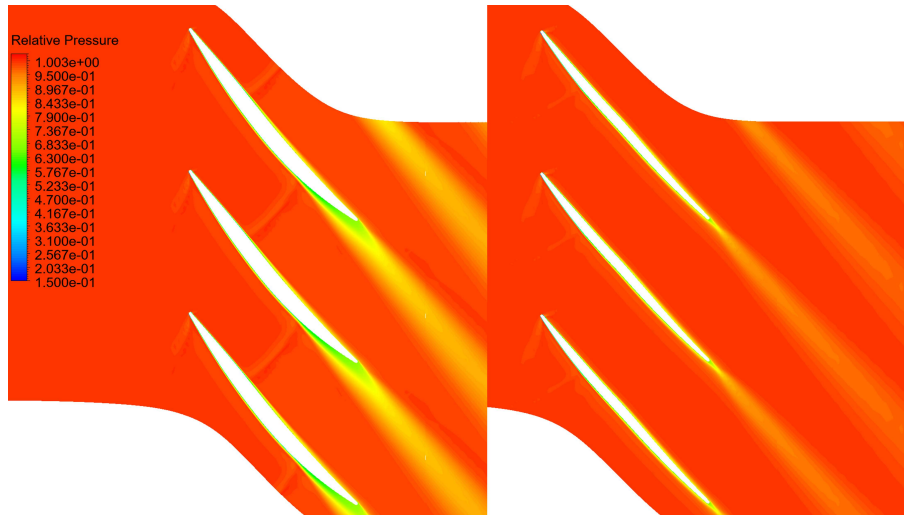
Figure 3.42: Relative total pressure contour for the baseline (left) and the individual with the best η_{pol} under design conditions (first design point). The values are expressed as the ratio between the relative total pressure at the specific position and the relative total pressure at the inlet.

In figure 3.41 it is noticeable that, although the Mach number is similar to the baseline (0.94 here, 0.90 the baseline) the flow fields show multiple differences. First, in the current airfoil, since the flow enters the passage with a non-zero incidence angle, a big expansion fan is formed on the suction side causing the flow entering the cascade to become supersonic. The air then decelerates, before entering the passage, due to a shock that originates from the suction side of the profiles. In the baseline, this effect is much weaker, with the expansion fan affecting only a small area. On the other hand, in the starting profile, the flow after entering the cascade accelerates again until reaching an almost normal passage shock. In the optimized profile, there are no other noticeable accelerations or decelerations of the flow inside the cascade, attributed to the geometry of the passage. Because the blade is almost straight, neither diffusion nor significant deviations of the flow are visible, and thus losses through the cascade are low. Finally, in the baseline, the shock passages caused the flow to separate at the end of the SS. In the current profile, since there are no other shocks than the one described before, no flow separation is visible. Also, the low deviation helps to contain the losses. Overall, because no passage shock is present on the current individual, the mass flow is not locked at its maximum level.

From figure 3.42 it can be noticed that the shock losses are very low in both cases, especially compared to the tip blade section where they were the main cause of loss of efficiency. The magnitude of the two shock losses here is similar in the two cases. In this blade section, the main cause for the decrease in η_{pol} of the baseline are wake losses. For the optimized individual, the wake is contained since no flow separation occurs also thanks to the shape of the profile.

The performances at the second design point are now investigated. Figure 3.43 and 3.44 reported respectively the relative Mach number and the total pressure ratio contours. Particularly, the total pressure ratio contour is obtained by dividing the total absolute pressure with the total absolute pressure at the inlet.

Figure 3.43: Mach contour of the individual with the best η_{pol} under near-stall conditions (second design point).

Figure 3.44: Absolute total pressure ratio contour for the baseline (left) and the individual with the best η_{pol} under near-stall conditions (second design point).

In figure 3.43, the flow field is more critical than in the baseline with a high-incidence condition and a partial separation of the flow on the suction side, visible from the big wake formed from almost half of the profile's chord. The inlet flow angle goes from 54.8° under design conditions to 60.6° with this back pressure with this high incidence condition visible from the shifted stagnation point This condition causes also the formation of an expansion fan on the suction side of the profile which ends with a normal shock. Overall this latter effect is very contained, not influencing the flow field. Although the profile is nearer to the stall compared to the baseline, the TPR at these conditions is smaller by only 0.65%. Although the inlet flow on the baseline is high subsonic (i.e. 0.80) the flow is almost everywhere subsonic. Similarly,

the optimized individual worked with a relative Mach number at the inlet of 0.78.

In figure 3.44 the baseline increases the total pressure gradually as the flow passes through the cascade thanks to the shape of the profile. On the other hand, in the current individual, since the blades are almost straight, all the flow deceleration and compression occur at the entrance of the cascade due to the contraction of the streamlines. Despite these differences, the final values of the objective functions are similar thanks to the similar inlet Mach conditions.

Overall, this profile performed well at both design points, exhibiting significant improvements under design conditions while matching the baseline at stall pressure. However, in the last simulation, the flow field conditions were more critical compared to the baseline. Despite this, for a BLI application, this profile remains a viable option, particularly if the emphasis is on engine efficiency.

Compromise

The next individual studied is the one being a compromise between the two objectives and it was created as the 158th profile of the optimization. In figure 3.45 the geometry of the profile is presented, while in table 3.12 the values of the decision variables are shown. The values of the OF are then reported in table 3.13.
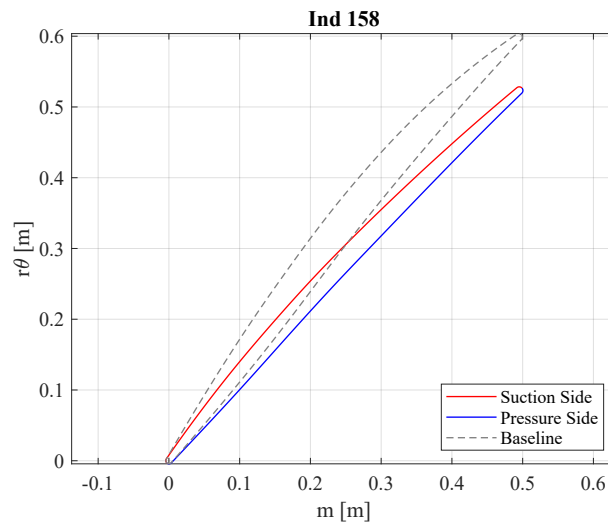
Figure 3.45: Best compromise individual.

Camber Line Variables [°]						Thickness Variables []	
-3.63	-5.66	-6.44	-6.16	-4.64	1.79	-0.56	-0.40

Table 3.12: Decision variables values of the compromise profile of the mid-span optimization with constant back pressure.

	Value	$\Delta\%$ form base
η_{pol}	0.921	7.89
TPR	1.328	1.74

Table 3.13: Objective functions values and comparison with the baseline for the best η_{pol} profile for the optimization at mid-span with constant back pressure.

The profile is thinner than the baseline with a slightly curved Camber line and a decreased stagger angle. The profile improved the efficiency by almost 8% while the TPR rose by less than 2%. To understand how these improvements are made, the flow field of the two design points is studied.

The results at the first design point are illustrated by the contours of relative Mach number and relative total pressure ratio, displayed in Figures 3.46 and 3.47, respectively.
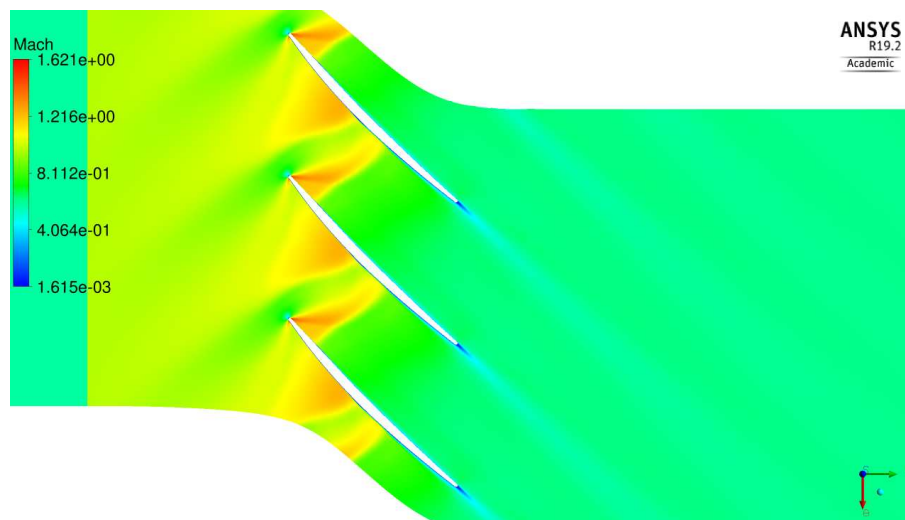
Figure 3.46: Mach contour of the compromise individual under design conditions (first design point).
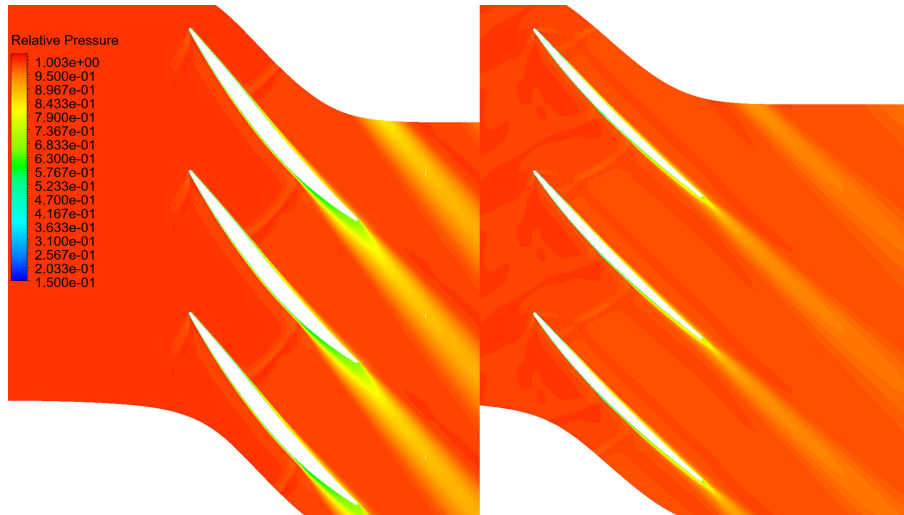
Figure 3.47: Relative total pressure contour for the baseline (left) and the compromise individual under design conditions (first design point). The values are expressed as the ratio between the relative total pressure at the specific position and the relative total pressure at the inlet.

The flow field of this profile shown in figure 3.46 is substantially different from the one of the baseline. In this case, the relative Mach number contour is similar to what occurs on supersonic cascades. The relative Mach number at the inlet is 0.97 while in the baseline was 0.90. It is visible near the LE, the formation of a detached bow shock. This is more clear in the branch entering the passage while the other part of the shock tends to dissolve. Two expansion fans are formed from the LE of the blade, accelerating the flow to supersonic conditions. The acceleration caused by the fan formed on the SS of the previous blade is the main reason why the inner shock is stronger than the other. After passing through this shock the flow is then accelerated from the second expansion fan. After this a second passage shock is formed and the flow becomes subsonic. This latter is not caused by the reflection of the bow shock but by the shape of the passage. Overall, the incidence angle of the cascade is contained, visible from the centered stagnation point.

In figure 3.47, the shocks formed on the optimized individual (right figure) create slightly more losses than the ones occurring on the baseline due to the higher velocities. Since the flow is low supersonic, shocks are weak and the decrease in relative total pressure is low. What still is the primary factor contributing to the loss of efficiency is the wake losses. In fact, in the left picture, the separation of the boundary layer caused by the shock causes a sensible total pressure loss. In the optimized individual, however, although there is a complex formation of shocks and expansion fans, the final wake of the cascade is contained. This last characteristic is the main reason why the current profile has a higher efficiency.

Now the second objective function results are investigating. In figure 3.48, the Mach number contour is reported while in figure 3.49 the total pressure ratio is shown.
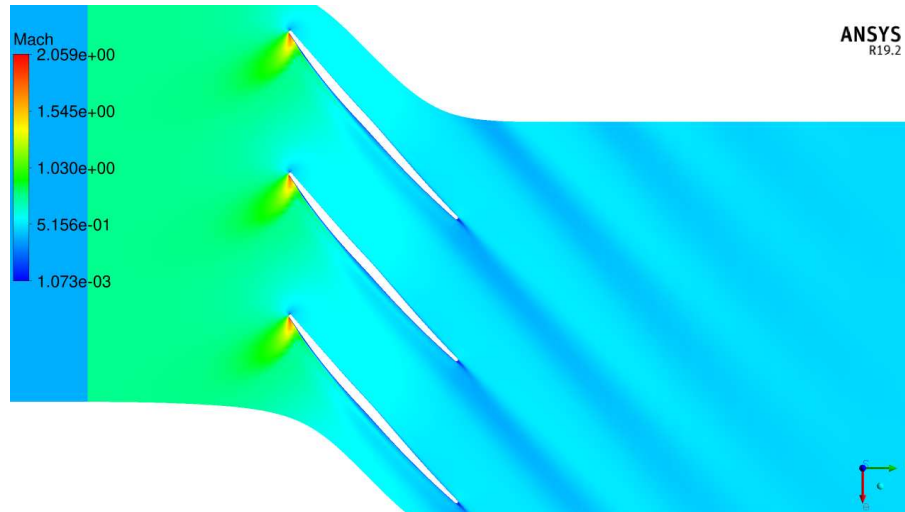
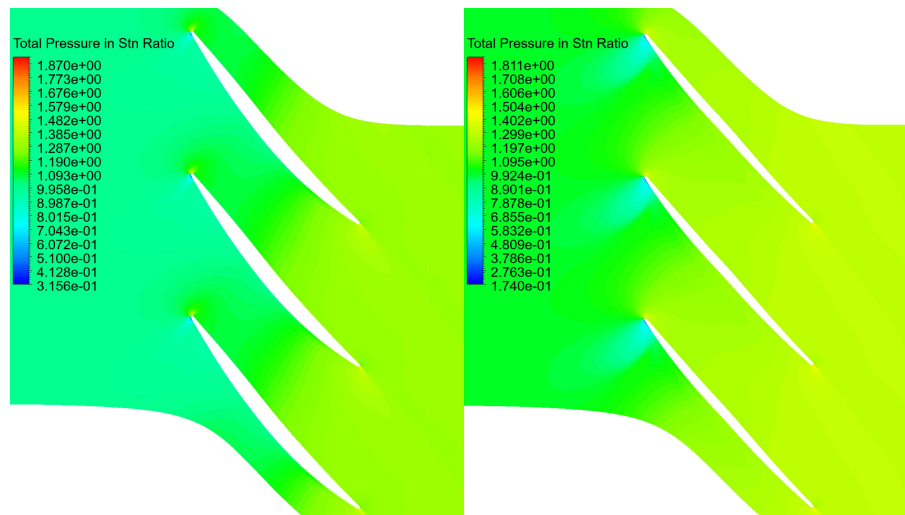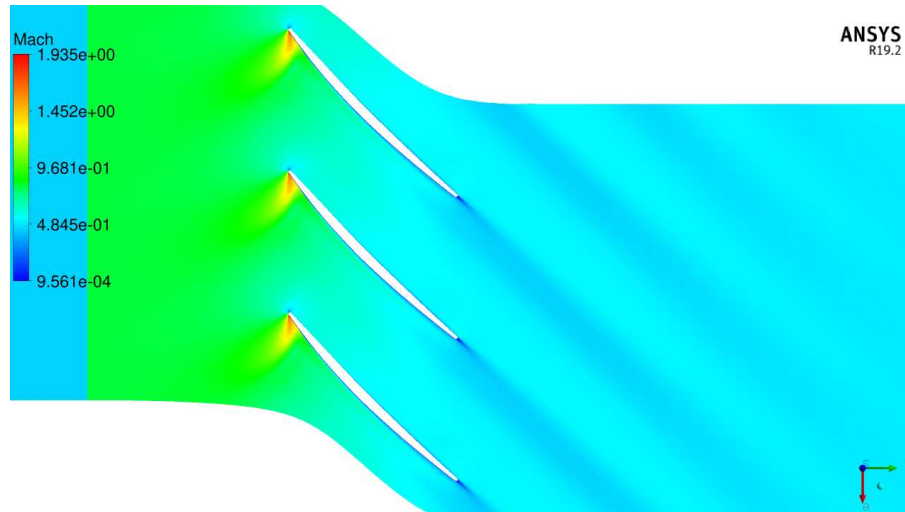Figure 3.48: Mach contour of the compromise individual under near-stall conditions (second design point).
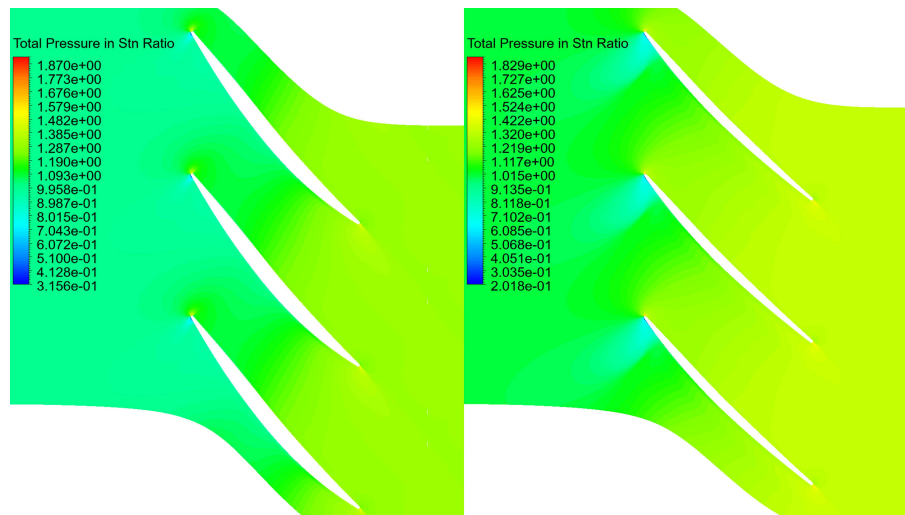
Figure 3.49: Absolute total pressure ratio contour for the baseline (left) and the compromise individual under near-stall conditions (second design point).

At the second design point, the flow slowed down to an inlet Mach number of 0.81, almost equal to the baseline. All of the flow field is subsonic, as visible from figure 3.48, except for a small expansion fan in the first part of the suction side. This is caused by the high incidence of the flow, noticeable also from the shifted stagnation point. In particular, the final angle of the flow is 57.48° which is almost 5° larger than at design point 1 and higher than at the baseline. The acceleration due to the fan is followed by a small shock that returns the flow to subsonic conditions. This is not visible in the baseline, where, thanks to the lower Mach number and incidence angle, the magnitude of the expansion fan is smaller. While passing the cascade the flow is slowed down and at the end of the SS, a separation of the boundary layer

occurs. This is similar to what was observed on the baseline.

From figure 3.49, it is visible how the optimized individual compressed the flow almost only at the entrance of the cascade while, in the baseline, the compression occurs more gradually throughout the passage. There seem to be no significant reasons why the TPR of the optimized cascade is better than the one of the initial profile but, since the difference is less than 2%, this is mainly due to the difference on the inlet Mach number that is 0.814 for the current individual and 0.800 for the baseline. In terms of efficiency, the optimized profile goes from 0.92% at the first design point to 0.93% at the second design point by reducing shock losses while the baseline increases its efficiency from 0.85% to 0.95% thanks to a smaller wake.

In conclusion, the profile shows good performances on both design points making it well-suited for BLI applications. In particular, under design conditions, the optimized individual improved the baseline efficiency by almost 8% thanks to the reduction of wake losses. Under stall conditions, the profile overcomes the baseline TPR mostly thanks to a higher inlet Mach number. In this condition, the profile improved also its efficiency thanks to the elimination of the shock losses, compared to the first design point.

Best TPR

The third individual studied is the best TPR profile, created as the 98th profile of the optimization. In figure 3.50 the geometry of the profile is presented, while in table 3.14 the values of the decision variables are shown. The values of the OF are then reported in table 3.15.
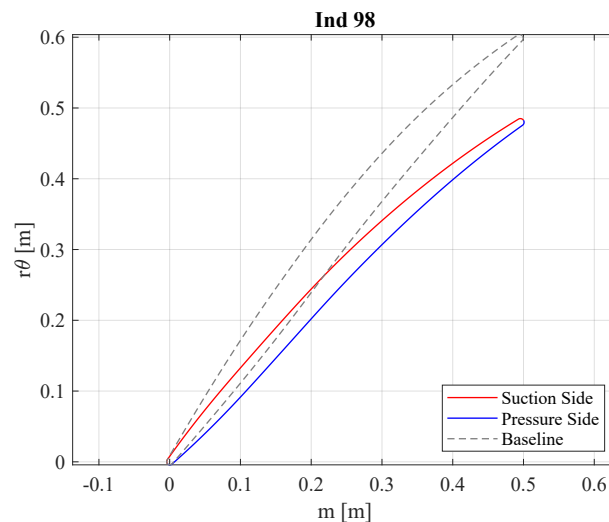
Figure 3.50: Best individual for TPR.

Camber Line Variables [°]						Thickness Variables []	
-6.50	-5.49	-6.50	-6.50	-6.50	-6.50	-1.00	-0.40

Table 3.14: Decision variables values of the best TPR profile of the mid-span optimization with constant back pressure.

	Value	$\Delta\%$ form base
η_{pol}	0.894	4.76
TPR	1.373	5.20

Table 3.15: Objective functions values and comparison with the baseline for the best TPR profile for the optimization at mid-span with constant back pressure.

The profile is thinner and more curved compared to the baseline. Specifically, it is similar to a MCA airfoil, with the initial arc appearing almost straight while the tail is more curved. The stagger angle is decreased compared to that of the baseline. All the decision variables are on the boundaries of the domain except for x_2 and x_7. This observation aligns with the trends shown in figure 3.37.

To delve deeper into the reasons behind the improvements observed in the objective functions due to the optimized profile, a study of the flow fields is now conducted. The relative Mach number and the relative total pressure ratio contour are presented respectively in figure 3.51 and 3.52.
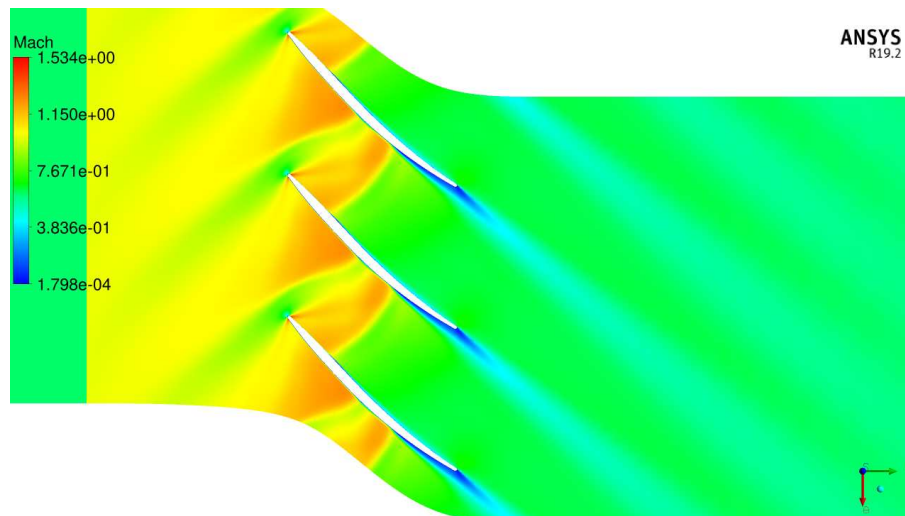
Figure 3.51: Mach contour of the individual with the best η_{pol} under design conditions (first design point).
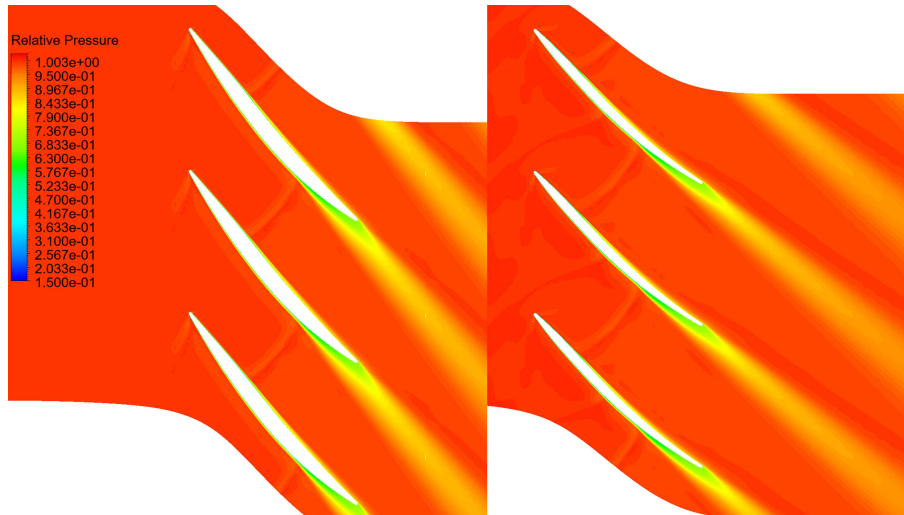
Figure 3.52: Relative total pressure contour for the baseline (left) and the individual with the best TPR under design conditions (first design point). The values are expressed as the ratio between the relative total pressure at the specific position and the relative total pressure at the inlet.

The flow field of this cascade (figure 3.51) is similar to the one found on the compromise individual. In this case, thanks to the lower stagger angle, the passage area is bigger enabling higher velocities than the baseline with a relative Mach number of 0.989. A detached bow shock is formed with the passage branch being stronger than the other. At the sides of the leading edge, two expansion fans are formed as in the previous individual, accelerating the flow to supersonic conditions. Inside the passage, the flow is then decelerated to subsonic conditions by an almost normal shock. This shock leads the boundary layer to separate, especially on the SS causing the growth of the wake as occurs on the baseline. The separation is promoted also by the curvature of the last part of the blade which creates an unfavourable pressure gradient.

The losses introduced by the shocks, and visible in figure 3.52, are similar in the two cases and again, they are not the main reason for the loss of efficiency. On the other hand, the wake is bigger on the baseline, mostly due to the increased thickness of the baseline. However, from the contour, the intensity looks similar. To delve deeper into the magnitude of the two different losses in the two profiles, this time a comparison between the relative total pressure ratio along the circumferential direction at the outlet of the cascade is presented. In particular, the reference arc is positioned at a distance of 0.5 the chord from the TE, downstream the cascade. The circumferential coordinate is normalized with respect to the pitch angle.
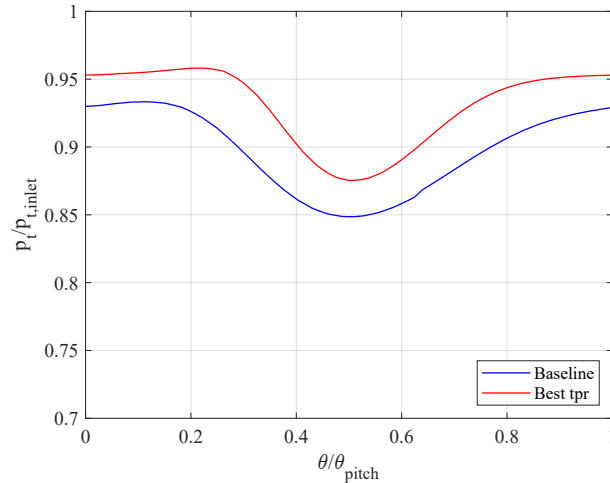
Figure 3.53: Trend of the relative total pressure ratio along the circumferential direction for the best TPR individual and the baseline under design conditions (first design point). Measurement at 0.5 chords from the blade TE of the array. Theta coordinate is normalised to the pitch, the y-coordinate to the total relative pressure at the inlet.

The shock losses on the baseline cause a bigger downshift of the blue line indicating that the shock is stronger. This is mainly due to the shape of the profile and the reduced acceleration on the current individual. Overall, shock losses are contained and in fact, in figure 3.52 the contour colours after the shock are similar. For wake losses, while intensity looks similar, in fact the difference between the highest value (free stream) and the lowest (TE flux) is the same on both curves, the one occurring in the baseline is more extended than in the best TPR individual. This is visible from the fact that the blue line returns to undisturbed flow conditions after the red line. Overall the optimized individual improved the efficiency by reducing shock losses and containing the wake dimension.

The performances at the second design point are now investigated. Figure 3.54 and 3.55 reported respectively the relative Mach number and the total pressure ratio contours.
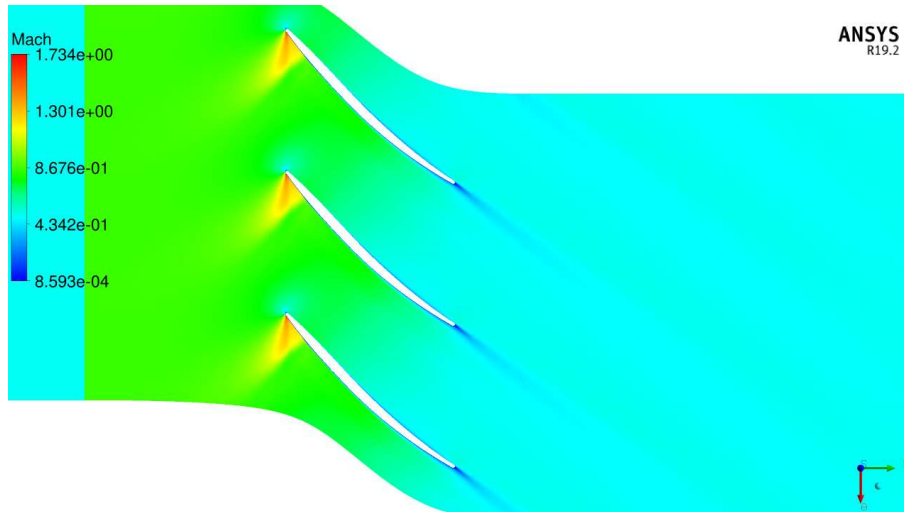
Figure 3.54: Mach contour of the individual with the best TPR under near-stall conditions (second design point).
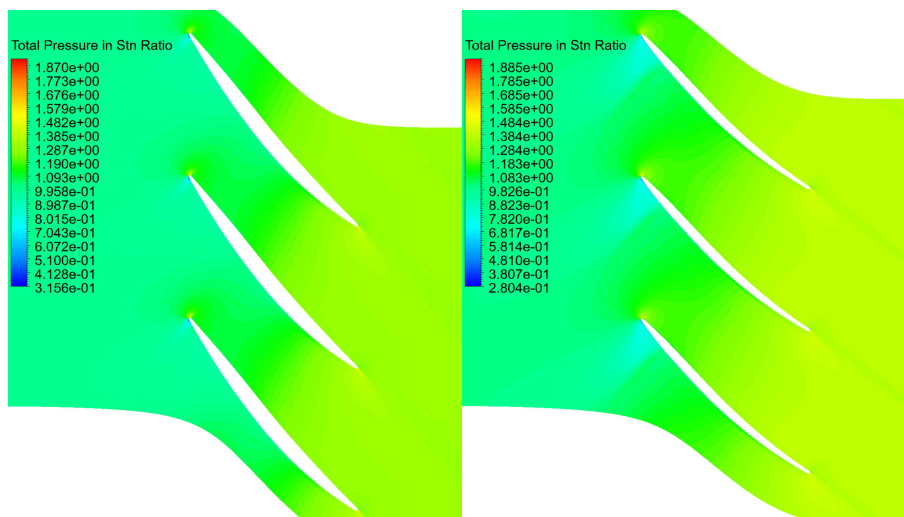
Figure 3.55: Absolute total pressure ratio contour for the baseline (left) and the individual with the best TPR under near-stall conditions (second design point).

The inlet angle, in this case, increases by more than 2° compared to the value at the design condition, due to the higher back pressure and lower rotational speed. Despite the little changes in the inlet angles, an expansion fan formed on the first part of the suction side due to the high velocities as visible in figure 3.54. The Mach number here is 0.86 which is higher than the baseline under the same conditions. After the expansion fan, the flow is supersonic and a normal shock wave decelerates the flow to subsonic conditions. This phenomenon is almost not observed on the baseline where, due to the lower incidence angle, the flow remains subsonic nearly everywhere. In the current individual, as well as in the baseline, no flow separation occurs on the suction side indicating good stability of the flow field.

From figure 3.55, it is visible that in the optimized profile as in the baseline, the compression occurs throughout the passage thanks to the shape of the blade. In the current profile, most of the increase in total pressure occurs in the first half of the profile while in the baseline this occurs in the second half. These zones where most of the compression happens are the areas where the passage shock is positioned in the two profiles at the first design point. This confirms that the passage shock was caused by the shape of the profile. Moreover, the shape of the baseline tends to create a shock shifted downstream, causing the flow separation. Although the process of compression is similar between the baseline and the current profile, the latter has better performances mainly for two causes. First, the deflection angle of the optimized profile is greater compared to the baseline and second, the speed is higher so more kinetic energy can be converted into pressure energy. In the previous cases, at the second design point, the profile efficiencies were penalized by the separation of the boundary layer at the SS. This does not occur on the baseline and hence the efficiency is very high. Also on the profile that optimizes the TPR, the flow did not separate and the efficiency here results in 0.961%, the highest of all the optimizations.

Overall the optimized profile outperforms the baseline in both conditions. At the first design point, the current individual increases the efficiency by almost 8% thanks to contained wake losses. On the second design point, the total pressure ratio increases thanks to a greater deviation of the flux and higher velocities. Under this condition also efficiency improves thanks to the low wake and shock losses overcoming the baseline by 1%. In conclusion, given the profile outstanding performance in both aspects, its results are highly suitable for BLI applications.

Conclusions

The good outcomes of the optimization were confirmed in this study, by highlighting the weaknesses of the baseline and illustrating how the optimizer successfully addressed them.

At the first design point, most of the losses on the baseline were caused by the separation of the boundary layer on the suction side of the profile. This separation was caused by the interaction between the passage shock and the suction side of the profile causing drastic growth of the wake. To overcome this problem, the optimizer worked on reducing the wake magnitude by shifting the shock upstream where the boundary layer was more stable. Moreover, the profiles with higher efficiency were also less curved so there were no adverse pressure gradients on the later part of the suction side.

For the second objective function, the baseline was already good but still some improvements were made. In particular, the TPR were increased firstly thanks to the higher velocities of the flow due to bigger passage areas, achieved with thinner and less staggered profiles. The individual with the best TPR was also more curved than the baseline and so it deviates more from the flow, thus exchanging more energy

In conclusion, a fundamental requirement for a profile to be considered good is the low thickness. Profiles who maximize efficiency are straight while individuals who privilege the TPR are curved and less staggered than the baseline.

3.2.3 Bayesian Optimization with variable back pressure

The initial sample used was the same as the previous optimization but the individuals were re-simulated to update the results for the new strategy at the second design point. After reviewing the results of the previous optimization, it was noticed that the minimum thickness was slightly too low for the specific

application. Particularly, since the blade is subjected to cyclical loads over time, the resistance section should not be too small so the boundaries of the last DV went from $[-0.4, +0.5]$ to $[-0.3, +0.5]$. The other limits of the optimization space were chosen as the last used previously. Because the time per individual was significantly higher than in the previous optimization, 90 individuals were simulated (122 with the LHS) for a total computational time of more than 150 hours (more than 6 days).

The overall results of the optimization are reported in figure 3.56, where the final population and the initial and final Pareto fronts are shown. It is important to notice that the baseline objective functions are different from the one used in the previous analysis since the conditions at the second design point were different.
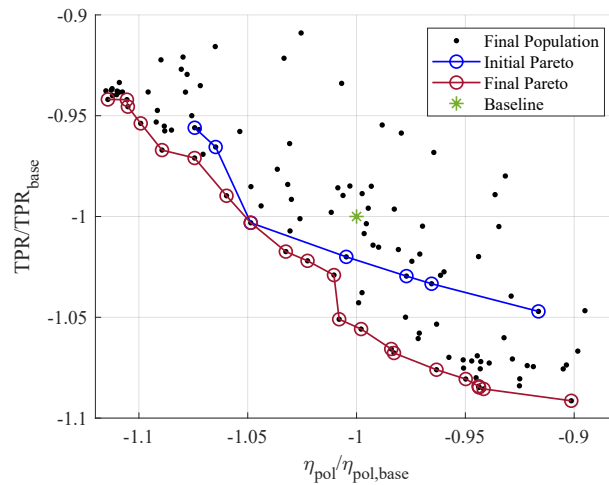
Figure 3.56: Results of the Bayesian Optimization at mid-span with variable back pressure, normalized with respect to the baseline.

Although the number of individuals generated by the optimizer is low, sensible improvements were achieved, with a final Pareto composed of 22 individuals. However, these improvements are relatively smaller compared to those obtained in the other cases, mainly because fewer individuals were simulated. Overall the final Pareto appears wide and densely populated with good solutions visible for both objectives. The most efficient individuals increase the baseline efficiency by almost 12%, while cascades with the best TPR achieved over a 9% improvement compared to the initial profile. However, these individuals are situated on the edges of the Pareto, and although they significantly gain in one objective function, they lack in the other when compared to the baseline.

To better understand the final results, the performances of each individual are represented on the DV space using a colour map. In particular, the efficiency is represented in figure 3.57 while the TPR results are shown in figure 3.58.
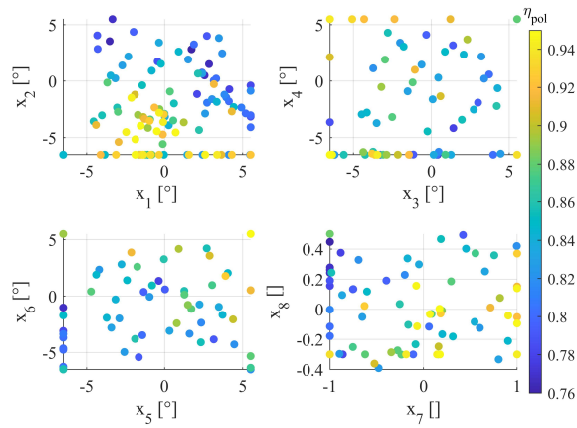
Figure 3.57: Rappresentation of the η_{pol} results of the airfoils in the space of the DV using a colour map. Results after the BO at mid-span using constant back pressure.
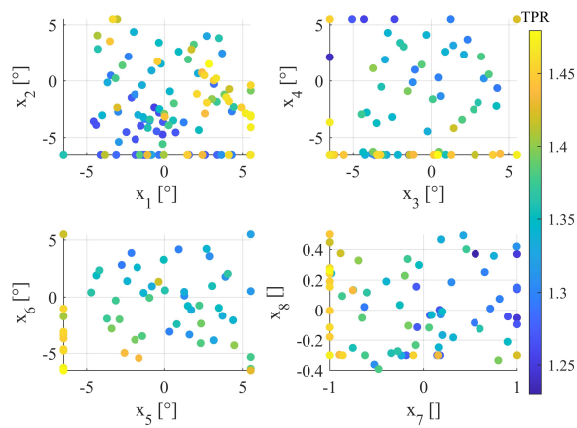
Figure 3.58: Rappresentation of the TPR results of the airfoils in the space of the DV using a colour map. Results after the BO at mid-span using constant back pressure.

Some blank spaces are visible in all the domains indicating that the optimizer did not explore enough the design space so to cover the entire domain more iterations are needed. For variables x_1 and x_2, in the efficiency results it is visible that all best individuals are clustered on the bottom left part of the graph, with some outliers on the bottom right. This is similar to what was found in figure 3.36 for the previous optimization. On the other hand, profiles with high TPR have positive values of x_1 (first angle bigger than the baseline) and negative for x_2. For the second objective, however, the correlation is weaker than for the η_{pol} results, especially for x_2. This is different to what was found for the previous optimization, where the best individuals were lying mostly on the left part of the graph. This difference can be caused by the lack of data in that zone. For variables x_3 and x_4, no stronger correlations are visible. Best individuals lay almost only on the boundaries of x_4 and on all domains of x_3. This is different from what happened previously, especially for high-efficiency profiles, that have negative x_3 with every x_4. In variables x_5 and

65

x_6, the correlation is opposite between the two objectives, with the best individuals stacked one over the other at the corners of the domain. In particular efficient profiles have values on the top right of the graph while high TPR cascades are on the bottom left. A similar influence of the variables is observed in the previous work. For the DV controlling the thickness, the optimizer did not concentrate on low-thickness individuals as in the optimization with constant back pressure. Here, the best individuals for both objectives have all values of x_8 as visible in figure 3.58. For x_7 the correlation is stronger and in fact, profiles with high values of the second objective have the maximum thickness shifted upstream (negative x_7) while airfoils with high efficiency are characterized by positive x_7 (maximum moved downstream).

To check whether the optimiser has reached some level of convergence or if still some improvements can be made, the Pareto, initial and final and real and fitted with the GPS are presented in figure 3.59. In particular, the fitted Pareto fronts were found using a GA optimizer. Since the computational cost of the evaluations of these functions was very low, 100000 generations of 100 individuals were generated.
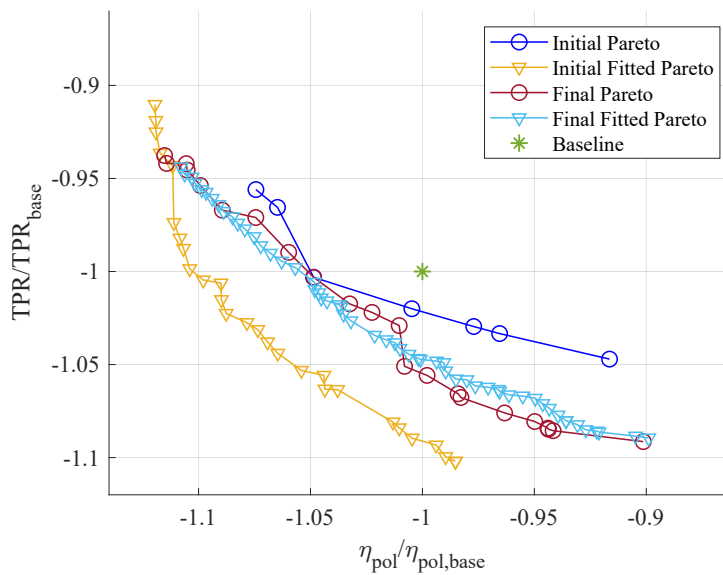
Figure 3.59: Pareto's fronts initial and final both real and predicted with the GPS model for the BO at mid-span with variable back pressure.

The final fitted Pareto and the final real Pareto are very similar but still, some differences are noticeable. These are due to the under definition of the GPS that are trained with too low data for this problem. Overall, the model predicts a Pareto front that closely aligns with the final one obtained by the optimizer, indicating the successful progress of the optimization. However, due to the significant distortion of the functions and the limited data in some areas of the decision variable space, it would be wise to continue the optimization.

Figure 3.60 shows the difference between the real value of the objective function and the predicted value both for the initial and final regression models. The initial regression models are trained using the LHS sample, while the final models are trained with all the population available at the end of the optimization.
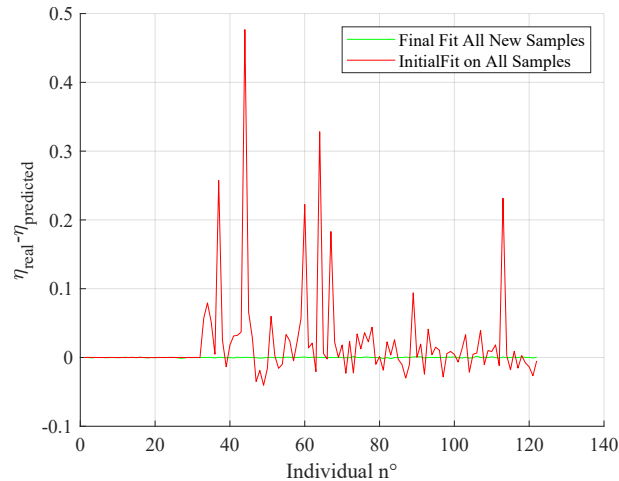
Figure 3.60: Differences between the real values of the first objective function with the one predicted using the first and last regression model.

As seen in the previous optimizations, the initial regression model has good performance only on the train data while on new samples there are a lot of differences between real end predicted values. This is mostly because the OF are complicated, so 32 individuals are not enough to recreate the functions. However, this uncertainty is acceptable at the beginning and it is why Bayesian optimizers perform well. The final model, on the other hand, predicts the values almost perfectly also because they are the data used to train the model. In summary, given the proximity of the two final Pareto fronts and the low error of the GPS models on the final population, it can be concluded that the optimization process is progressing very well. Convergence appears to be within reach, although additional data are still required.

Now, to compare the results of the two optimizations, the Pareto fronts are presented on the same graph with the respective baseline. The axes are not normalized due to differences in the baseline objective function values.
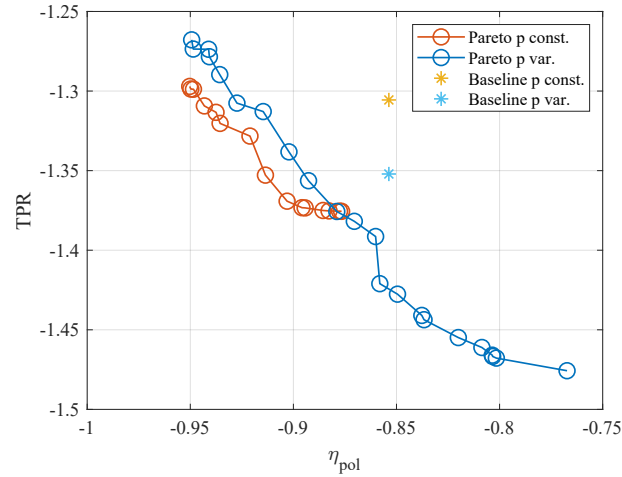
Figure 3.61: Comparison of the final Pareto fronts obtained with the BO at constant back pressure and variable back pressure, plotted on the OFs space.

Although the second optimization evaluates fewer individuals, its Pareto front is wider compared to the one obtained with the first optimization. Moreover, the results found with the second strategy are improving also the first baseline. Comparing profiles on the two Pareto fronts, the two optimizations have similar results. Individuals who maximize the η_{pol} in both cases improve the weaknesses of the baseline, in particular the wake losses. In the first optimization, the profiles were straight to avoid boundary layer separation. However, on the second optimization, the airfoils are not straight but a discontinuity is visible in the middle of the Camber line. This seems not to have any specific purpose and it would probably disappear with the continuation of the optimization. Similar results were obtained also for high TPR individuals. They were more curved, to enable a higher deflection of the flow and so exchange more energy.

Despite these similarities, the optimization with the second strategy looks behind the first one, especially in the zone of high-efficiency individuals. To delve deeper into the results in this area, one individual for each optimization is selected. In particular, to compare more fairly the results, the individual selected from the first optimization was the compromise individual studied in the previous section. This was chosen because it has an "incidence angle" of 4.78° and so the conditions at the second design point are similar between the two profiles. For the last optimization, the individual selected was generated at the 50th iteration (82nd considering also the LHS). This profile has a final back pressure of $43480 Pa$, obtained at the third simulation under near-stall conditions. This back pressure is similar to the one of the other individual, making the comparison more fair. In figure 3.62 the two individuals are represented on the respective Pareto fronts while the fitness functions values are reported in table 3.16.
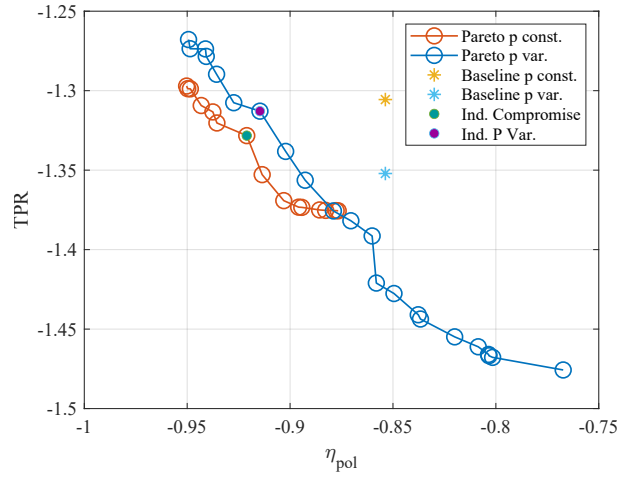
Figure 3.62: Individuals selected for the comparison of the two optimizations at mid-span.

	η_{pol}	TPR
BO constant pressure	0.921	1.328
BO variable pressure	0.915	1.313
$\Delta\%$	0.651	1.130

Table 3.16: Objective functions values of the profiles obtained form the two BO.

The geometries of the two individuals are compared in figure 3.63 while the values of the DV are reposted in talbe 3.17.
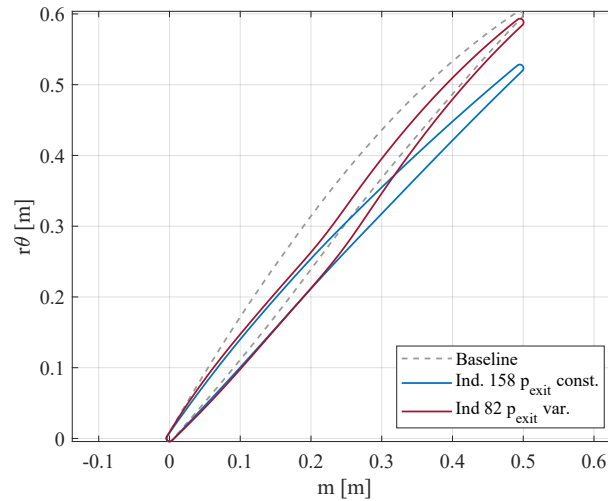
Figure 3.63: Geometries of the individuals selected for the comparison of the two optimizations at mid-span.

	Camber Line Variables [°]						Thickness Variables []	
BO p conts.	-3.63	-5.66	-6.44	-6.16	-4.64	1.79	-0.56	-0.40
BO p var.	-2.95	-5.38	-6.50	5.50	5.50	0.53	-1.00	-0.30

Table 3.17: Decision variables values of the best η_{pol} profiles of the BO and GA optimizations.

Although the two profiles have very similar performance under similar boundary conditions, the geometries are quite different. In the current individuals, the second part of the Camber line deviates from other profiles creating a shape similar to a dovetail. The values of the DV confirm that the profile is almost equal in the first half while in the second they are almost opposite.

To understand how these two different geometries reach similar results, first, the Mach contour and the relative total pressure ratio contour of both individuals are presented.
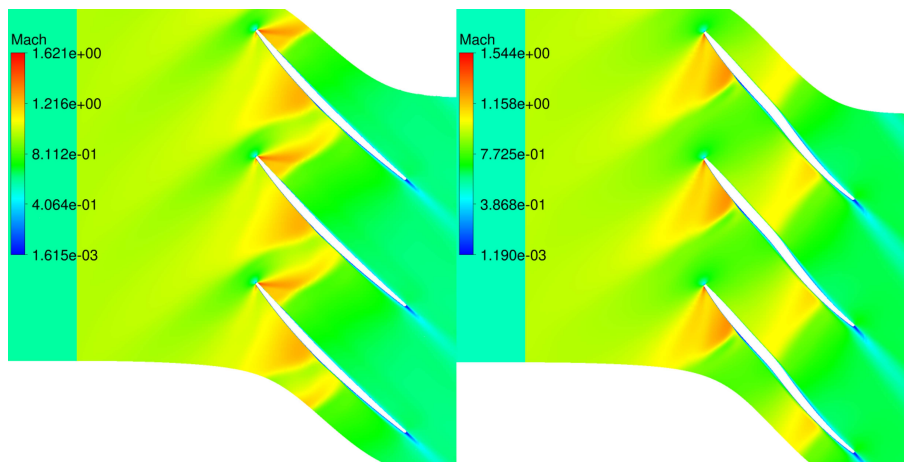
Figure 3.64: Mach contour of the individual with the individual form the first optimization (left) and second (right) under design conditions (first design point).

Figure 3.65: Relative total pressure ratio contour for the individuals from the first optimization (left) and second (right) under design conditions (first design point).

The two flow fields in figure 3.64 are different although the final efficiency is almost the same, with the right contour being similar to the baseline. Moreover, the dovetail shape of this individual creates a convergent zone inside the passage that accelerates the flow like in a nozzle. This acceleration terminates on the second half of the camber line with the presence of a passage shock. Although the passage shock on the current individual is positioned on the second half of the passage, no flow separation is visible. This occurs due to the passage shape, resembling a diffuser after the shock, thereby generating a favourable pressure gradient. In the profile of the first optimization, the flow field is different and it is similar to a supersonic cascade flow field. Overall the η_{pol} of the two cases is very similar because the wake losses are limited since no boundary layer separation occurs. The relative inlet Mach number of the individual from the first optimization is 0.97 while in the current profile is 0.94. For this reason, the difference in the final values of η_{pol} is not caused by the viscous stresses.

Form figure 3.65 it is noticeable the separation of the boundary layer on the initial part of the suction side, but overall it appears to be well-contained and it is not the primary cause of the efficiency loss. Looking at the shock losses, on the left case slightly greater decrease in total pressure ratio is visible compared to the right due to the higher velocities on the first profile. On the other hand, the current cascade shows slightly larger wake losses, noticeable especially from the TE of the two individuals. To compare these last two losses, the relative total pressure ratio is plotted downstream the profiles along a circumferential direction as visible in figure 3.66.
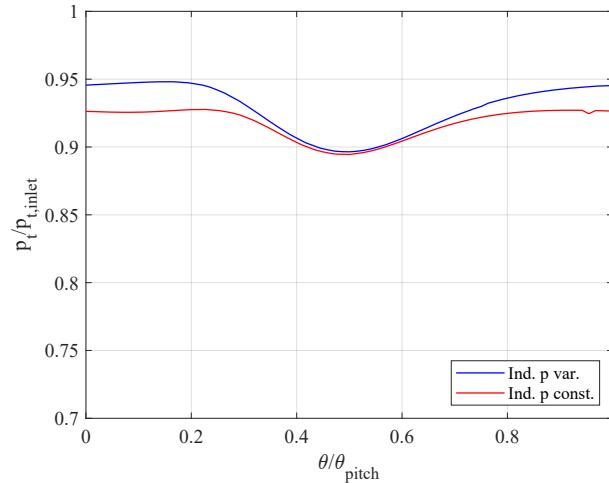
Figure 3.66: Relative total pressure downstream the cascade.

The shock losses on the current individual are lower than those on the optimized profiles from the first optimization visible from the downshift of the red line in figure 3.66. On the other hand, the wake losses are higher for the current individual, as indicated by the fact that the two curves converge to the same value at the centre while starting from different heights. This is the main reason why the optimized individual with the variable pressure outlet has a little higher losses. Moreover, looking back at figure 3.64, it is visible that the wake is not perfectly aligned with the final part of the profile. These higher losses are mainly due to the final shape of the airfoil. Overall, this confirms that in this blade section, the most significant losses are caused by the wake.

To understand the differences in the performances at the second design point, the relative Mach number contour and the total pressure ratio contour are reported hereafter. Particularly, the total pressure ratio is calculated as the ratio between the absolute total pressure and the absolute total pressure at the inlet, which is the same on both cases.
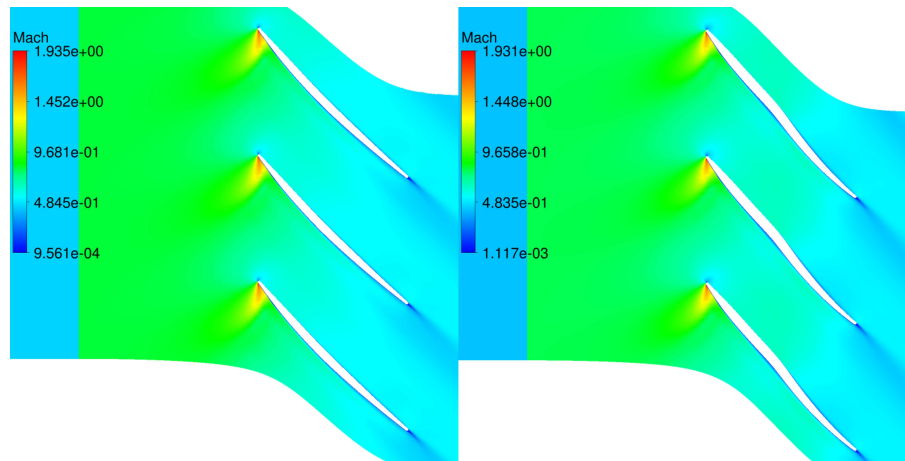
Figure 3.67: Mach contour of the individuals from the first optimization (left) and second (right) under near-stall conditions (second design point).
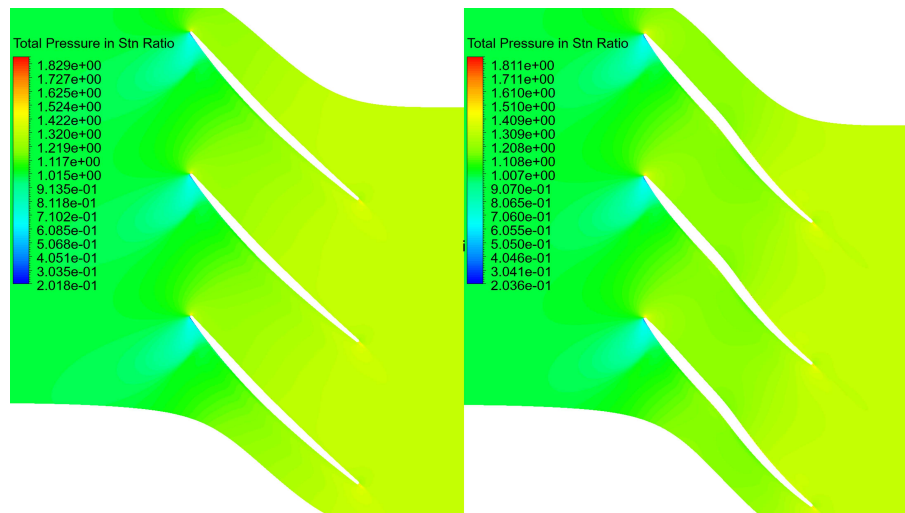
Figure 3.68: Total pressure ratio contours of the individuals from the first optimization (left) and second (right) under near-stall conditions (second design point).

Since the $\Delta\beta$ is similar in the two cases, and the profiles have almost the same shape on the first part of the Camber line, the flow filed in this region is very similar, as visible in figure 3.67. More differences are noticeable in the second half of the airfoil. Here, since the passage has a divergent shape, the separation of the flow is slightly more contained in the current profile than in the left individual. On the other hand, the dovetail shape of the profile obtained with the second optimization creates some small zones where the flow decelerates. Form figure 3.68 it can be noticed that the shape of the profile obtained with the second optimization causes the total pressure to fluctuate inside the passage. This, combined with the slightly lower Mach number for this profile (0.81 vs. 0.79), are the reasons why the TPR of this profile is lower than that of the other profile. Although the shape causes a fluctuation of the total pressure, the

final wake of the current profile is smaller than the one of the first one. Also in this case the wake is the leading cause for the efficiency losses and in fact, the final η_{pol} is 0.93% for the individual obtained with the second optimization while for the other is 0.92%.

Overall, although the profiles have different geometries, the final results of the two flow fields are similar. In particular both the individuals improved the baseline problems in similar ways. However, the dovetail geometry of the individual obtained by the second optimization appears to lack functional reasons for its specific shape. It is possible that with further optimization iterations, the shape becomes more similar to the one obtained in the first optimization.

Conclusions

The two different strategies for simulating near-stall conditions brought similar results, although some differences were observed.

First, the Pareto front obtained with the second strategy looks much wider than the first one, indicating that more solutions were explored. Imposing the incidence angle instead of a fixed back pressure allows for more cascades to be simulated without encountering numerical issues. Moreover, the conditions at the second design point were more similar whereas on the first optimization, the individuals were in more different conditions. Profiles with higher stall pressure were unable to achieve their final TPR, penalizing the second objective function. An example of this is the baseline, which has a higher pressure ratio in the second optimization.

Looking at the geometry of the profiles composing the Pareto, in general, individuals with high TPR were really curved and thin, confirming what was found in the previous optimization. On the other hand, high η_{pol} airfoils exhibited geometric differences between the two strategies. While both minimized the baseline losses (especially wake losses), in the first optimization, they were straight, whereas in the second, dovetail profiles were generated. The unusual shape of the profile composing the final Pareto of the second optimization seems not to be justified. To confirm this, further optimizations are necessary to validate the effectiveness of this particular geometry. Overall these differences are the main causes for the second Pareto front to be slightly behind.

In conclusion, the use of a different strategy to recreate near-stall conditions on the profiles allowed for a much larger Pareto front to be found. Moreover, the comparison between the individuals was more fair in terms of proximity to the stall conditions, without penalizing the profiles that have different stall pressures. However, to confirm the effectiveness of these results, the optimization should be continued further.

4 Conclusion

A multi-objective, multi-point optimization of two different profiles of a transonic fan was conducted to find the main features of distortion-tolerant profiles. A Bayesian optimizer was used for its velocity of convergence whereas objective functions evaluations were performed using bi-dimensional steady state CFD simulations. The tip blade section was investigated for its high sensitivity to inflow conditions. For the second optimization at mid-span, near-stall conditions were obtained by looking at the inlet incidence angle. This latter study was used as a comparison with the first strategy.

For the tip blade section, improvements of almost 15% were achieved in terms of η_{pol} compared to the baseline while only 5% for the second objective function. High η_{pol} profiles were thicker than the baseline and had almost the same stagger angle. The improvement was obtained by reducing the losses caused by the second passage shock. Particularly, no reflection of the passage shock was present because the profiles were nearer to the stall conditions than the baseline. Results similar to the baseline were achieved at near-stall conditions where improvements were obtained thanks to stronger shock on the optimized profiles. Individuals with high TPR were thinner and had a curved Camber line on the back. Performances were improved on the second objective, enhancing the total pressure ratio through stronger shocks and partly deflecting the flow. Additionally, efficiency was improved under design conditions due to weaker second passage shocks. This reduction was achieved by a lower contraction of the passage.

At mid-span, in the optimization with the first strategy, a common feature of the overall population was the low thickness of the high-performance profiles. High-efficiency profiles increased the η_{pol} up to 11% compared to the baseline thanks to a reduction in the wake losses. In particular wake losses were caused by the interaction between the suction side and the passage shock. Best individuals were straight and improved performances by expelling the passage shock. High TPR individuals increased the second objective thanks to higher velocities and greater flow deviation achieving up to a 5.2% increase in pressure ratio compared to the baseline. The resulting profiles were more curved and with a lower stagger angle than the baseline. Good performances were obtained also on the first objective function thanks to contained wake losses. This was achieved by shifting upstream the second passage shock and thus containing the flow separation.

With the second optimization strategy, the final Pareto was wider and slightly behind the one obtained with the first optimization of the mid-span. The bigger extension was mainly due to the variable back pressure. In the first optimization, the fixed back pressure caused the elimination of certain profiles because of the too-high counter-pressure whereas the adjustable back pressure of the second strategy allowed the exploration of more solutions. In terms of decision variables, the biggest difference was observed with the thickness where no correlation between x_8 and performance was visible. High TPR profiles were thin and with a curved camber line, confirming what was found in the previous optimization. On the other hand, high η_{pol} airfoils exhibited geometric differences between the two strategies. While both minimized the baseline losses (especially wake losses), in the first optimization, cascades were straight, whereas, in the second, dovetail profiles were generated. Furthermore, certain areas of the design variable space remain unexplored, leading to the neglect of some solutions. Overall, the use of a different strategy to recreate near-stall conditions on the profiles allowed the finding of a wider Pareto front compared to the first strategy.

Finally, the Bayesian optimizer demonstrated its effectiveness in comparison with the GA, obtaining

similar results. A faster convergence was observed in the BO with this latter reaching the final Pareto at about 50% of the total evaluations while the genetic took more than 70%. Moreover, at less than 2/10 of the total iterations, the BO already started to find individuals on the final Pareto, with good solutions for both objectives. This was not observed in the case of GA, where the optimizer continued to extend the Pareto front as the optimization proceeded.

A APPENDIX

A.1 Riassunto Esteso

La propulsione BLI (Boundary Layer Ingestion) è un concetto promettente nell'ingegneria aeronautica che mira a migliorare l'efficienza degli aerei. Questa tipologia di soluzione porta però a delle problematiche a livello del motore a causa del fatto che il flusso all'inlet è distorto. La seguente tesi affronta la progettazione di una famiglia di profili che reasca a lavorare in modo efficiente quando soggetta a flussi in ingresso distorti. Per trovare le caratteristiche principali dei profili tolleranti alle distorsioni è stata utilizzata un'ottimizzazione multi-punto multi-obiettivo. Il primo capitolo offre una panoramica su questo argomento, oltre ad illustrare una serie di contributi scientifici sul tema e ad indicare gli obiettivi dell'elaborato.

Nel secondo capitolo vengono presentati i metodi utilizzati. Inizialmente viene introdotto il caso studio, contestualizzando quindi il lavoro di tesi. Viene poi descrtitta la modalità con la quale la geometria viene parametrizzata durante l'ottimizzazione. In particolare, i profili vengono ricostruiti parametrizzando separatamente Camber line e distribuzione degli spessori, utilizzando delle B-spline cubiche. In seguito, il modello CFD utilizzato per le simulazioni viene presentato assieme ad un'analisi di convergenza della mesh, resa necessaria per validare i risultati ottenuti. I punti di ottimizzazione scelti per il caso studio sono poi presentati. Il primo punto scelto è stato l'efficienza politropica in condizione di progetto mentre il secondo è stato il rapporto tra le pressioni totali in condizioni di stallo. Due diversi metodi per la scelta delle condizioni di stallo sono stati utilizzati. Nel primo, condizioni uguali venivano applicate per tutti gli individui dell'ottimizzazione mentre nel secondo le condizioni di stallo venivano decise guardando all'angolo in ingresso. Infine è stato descritto l'ottimizzatore utilizzato. In particolare è stato utilizzato un ottimizzatore Bayesiano per la sua velocità di convergenza alla soluzione finale.

Nel terzo capitolo vengono presentati i risultati. Prima viene analizzata l'ottimizzazione eseguita al tip della pala. Per questa sezione palare, sono stati ottenuti miglioramenti di quasi il 15% in termini di prestazioni rispetto al valore della baseline, mentre solo il 5% per la seconda funzione obiettivo. I profili ad alta efficienza risultavano più spessi rispetto alla baseline e avevano angoli di calettamento simili. Il miglioramento è stato ottenuto riducendo le perdite causate dal secondo shock di passaggio. Gli individui con elevato TPR hanno aumentato il secondo obiettivo grazie a velocità più elevate e una maggiore deflessione del flusso, superando la baseline di quasi 5%. I profili risultanti erano più curvi e con un angolo di calettamento inferiore rispetto al profilo di partenza. È stato poi confrontato l'ottimizzatore Bayesiano con un ottimizzatore ben collaudato basato su un algoritmo genetico. Risultati simili sono stati ottenuti ed inoltre è stata osservata una maggiore velocità di convergenza da parte del Bayesiano. La sezione di mid-span della pala è stata poi analizzata. Una prima ottimizzazione Bayesiana è stata eseguita utilizzando delle condizioni simili alla sezione superiore. Si è notato come i profili ad alta efficienza aumentavano le prestazioni fino all'11% rispetto al valore della baseline grazie a una riduzione delle perdite di scia. Qui gli individui migliori erano diritti e miglioravano le prestazioni espellendo lo shock di passaggio. Gli individui ad alto TPR hanno aumentato il secondo obiettivo grazie a velocità più elevate e una maggiore deflessione del flusso, aumentando le prestazioni fino a 5,2% in più ripetto al rapporto di compressione della baseline. I profili risultanti erano più curvi e con un angolo di calettamento inferiore

rispetto alla baseline. Una seconda ottimizzazione è stata poi eseguita utilizzando una diversa tecnica per la determinazione delle condizioni di stallo. In particolare si guardava all'angolo del flusso in ingresso. Una buona correlazione con i risultati precedenti è stata trovata, ed in particolare con questa tecnica il fronte di Pareto finale è risultato più esteso ripetto al caso precedente.

BIBLIOGRAPHY

[1] S. Solomon, G.-K. Plattner, R. Knutti, and P. Friedlingstein, "Irreversible climate change due to carbon dioxide emissions," *Proceedings of the National Academy of Sciences*, vol. 106, no. 6, pp. 1704–1709, 2009.

[2] E. Commission and D.-G. for Climate Action, *Going climate-neutral by 2050 – A strategic long-term vision for a prosperous, modern, competitive and climate-neutral EU economy.* Publications Office, 2019.

[3] H. Ritchie, "Climate change and flying: what share of global co2 emissions come from aviation?," *Our World in Data*, 2020. https://ourworldindata.org/co2-emissions-from-aviation.

[4] "Global Outlook for Air Transport - December 2023 - Report." https://www.iata.org/en/iata-repository/publications/economic-reports/global-outlook-for-air-transport—december-2023—report/, 12 2023. [Online; accessed 2024-02].

[5] A. M. O. Smith and H. E. Roberts, "The jet airplane utilizing boundary layer air for propulsion," *Journal of the Aeronautical Sciences*, vol. 14, pp. 97–109, 1947.

[6] D. Williams, "Review of current knowledge on engine response to distorted inflow conditions," *Proceedings of the Engine Response to Distorted Inflow Conditions*, pp. 1–32, 1987.

[7] V. J. Fidalgo, C. Hall, and Y. Colin, "A study of fan-distortion interaction within the nasa rotor 67 transonic stage," 2012.

[8] A. Lesser and R. Niehuis, "Transonic axial compressors with total pressure inlet flow field distortions," in *Turbo Expo: Power for Land, Sea, and Air*, vol. 45578, p. V01AT01A036, American Society of Mechanical Engineers, 2014.

[9] E. Gunn and C. Hall, "Aerodynamics of boundary layer ingesting fans," in *Turbo Expo: Power for Land, Sea, and Air*, vol. 45578, p. V01AT01A024, American Society of Mechanical Engineers, 2014.

[10] H. Pearson and A. McKenzie, "Wakes in axial compressors," *The Aeronautical Journal*, vol. 63, no. 583, pp. 415–416, 1959.

[11] W. T. Cousins and M. W. Davis Jr, "Evaluating complex inlet distortion with a parallel compressor model: Part 1—concepts, theory, extensions, and limitations," in *Turbo Expo: Power for Land, Sea, and Air*, vol. 54617, pp. 1–12, 2011.

[12] M. J. Shaw, P. Hield, and P. G. Tucker, "The Effect of Inlet Guide Vanes on Inlet Flow Distortion Transfer and Transonic Fan Stability," *Journal of Turbomachinery*, vol. 136, p. 021015, 10 2013.

[13] L. Da, L. Hanan, Y. Zhe, P. Tianyu, D. Hai, and L. Qiushi, "Optimization of a transonic axial-flow compressor under inlet total pressure distortion to enhance aerodynamic performance," *Engineering Applications of Computational Fluid Mechanics*, vol. 14, no. 1, pp. 1002–1022, 2020.

[14] A. CFX-Solver, "Theory guide," *Release ll*, 2006.

[15] C. C. D. Ronco and E. BENINI, "Gedea-ii: A simplex crossover based evolutionary algorithm including the genetic diversity as objective," 2013.

ACKNOWLEDGEMENT